Tungsten Telluride Quantum dot-based Biosensor for Alpha-Methylacyl CoA Racemase – An Emerging Prostate Cancer Biomarker

UNIVERSITY *of the*
WESTERN CAPE

By

Zaiyaan Begum Sampson (BSc Honours)

A thesis submitted in partial fulfilment of the requirements for the degree of

Magister Scientiae in Nanoscience

Faculty of Natural Science
University of the Western Cape
Cape Town, South Africa

Supervisor: Prof. Emmanuel I. Iwuoha
Co-supervisor: Dr. Samantha Douman

November 2019

Abstract

Prostate cancer, commonly referred to as adenocarcinoma of the prostate, is the leading cause of cancer death in men in 46 countries, and it was estimated that by the end of 2018 there would approximately be 1.3 million new cases of prostate cancer worldwide. Currently, the Food and Drug Administration (FDA) approved biomarker for prostate cancer disease diagnostics Prostate Specific Antigen (PSA) is not specific to the disease itself but extends to other cases such as Benign Prostate Hyperplasia (BPH) a condition in which the prostate grows uncontrollably. This biomarker is then detected in blood samples via conventional methods which require a qualified individual to operate and are often time consuming. Examples of these methods are spectrophotometry and High Performance Liquid Chromatography (HPLC). Hence, a more efficient biomarker and method of detection is needed for prostate cancer disease diagnostics, as early detection of the disease means early treatment, which could ultimately save lives. Currently, an emerging biomarker for prostate cancer known as Alpha-Methyl CoA Racemase (AMACR) has shown to be more specific to the disease with advantages such as being a non-invasive biomarker. AMACR has been reported to be present in urine, and thus may be detected via a non-invasive method. This study proposed an economical, non-invasive electrochemical biosensor for the rapid detection of AMACR based on mercaptosuccinic acid capped tungsten telluride (MSA-WTe_3) quantum dots (QDs). Nanomaterial has shown promise in terms of increasing the sensitivity and specificity of sensors. MSA-WTe_3 QDs was successfully synthesized using easy, inexpensive method and was studied by various techniques such as High Resolution Transmission Electron Microscopy (HR-TEM) where the size was confirmed to be within the nanometer scale and was reported to be 2.65 nm with a good crystallinity. X-ray diffraction (XRD) confirmed the structural properties and chemical composition of the QDs and it is reported that the QDs are rich in both tellurium and tungsten and comprise of a hexagonal structure. Scanning Electron Microscopy (SEM) confirmed the successful immobilization of aptamer sequence specific to AMACR onto the electrode surface by showing a distinct conformational change when aptamers were introduced to the QDs under study. This study reports the successful detection of AMACR using an MSA-WTe_3 QDs based aptasensor immobilized onto a screen printed glassy carbon electrode, with a detection limit of 0.35651 ng/mL and a limit of quantification calculated to be 1.08033 ng/mL.

Keywords

Prostate Cancer

Aptamer

AMACR

Quantum Dots

Mercaptosuccinic Acid

Tungsten Telluride

Biomarker

Diagnostics

Biosensor

Aptasensor

Electrochemical Impedance Spectroscopy

Differential Pulse Voltammetry

Microwave Synthesis

Abbreviations

AMACR – Alpha-Methylacyl CoA Racemase

CE – Counter Electrode

CV – Cyclic Voltammetry

DPV – Differential Pulse Voltammetry

EDS - Energy Dispersive X-ray Spectroscopy

EIS – Electrochemical Impedance Spectroscopy

FDA – Food and Drug Association

HR-TEM – High Resolution Transmission Electron Microscopy

HR-SEM - High Resolution Scanning Electron Microscopy

IUPAC – International Union of Pure and Applied Chemistry

MSA – Mercaptosuccinic Acid

POC – Point of Care

PSA - Prostate Specific Antigen

QDs – Quantum Dots

RE – Reference Electrode

SAXs – Small Angle X-ray Scattering

SPE – Screen Printed Electrode

UV-Vis –Ultraviolet Visible Spectroscopy

WE – Working Electrode

WTe_3 - Tungsten Telluride

HPLC – High Performance Liquid Chromatography

R_{ct} – Charge Transfer Resistance

Declaration

I declare that **Tungsten Telluride Quantum dot-based Biosensor for Alpha-Methylacyl CoA Racemase – An Emerging Prostate Cancer Biomarker** is my own work, that it has not been submitted for any degree or examination in any other university, and that all the sources I have used or quoted have been indicated and acknowledged as complete references.

Signature ----------

Zaiyaan Begum Sampson **November 2019**

Dedication

This work is dedicated to my mother Soraya Naidoo and my father Rafique Sampson, who always wanted me to continue studying despite social pressures and obligations, I love you both. To all my family members who helped me along the way to make this journey easier for me I say shukan to you. To a very special friend Uzair Jones thanks for putting up with me this year.

Acknowledgements

I would like to thank Allah (SWT) for granting the ability and the opportunity to complete my work.

A special thanks to my supervisor, Prof. Emmanuel Iwuoha, for his guidance and support.

To my Co-Supervisor Dr. Samantha Douman who always went out of her way to make sure that deadlines were met and that emotional support was offered to aid my success in this project.

To my friend Marlon whom without I wouldn't have been able to complete this work.

To the rest of SensorLab, especially Dr. Waryo, for always lending a helping hand in the laboratory and all the staff and researchers, thanks for the advice and friendship.

Thank you to the DST for making this study possible, as well as Mrs. Valencia Jamalie for sorting out ordering of chemicals and making sure they are delivered on time.

\

List of Publications

Zaiyaan Sampson, Samantha Douman and Emmanuel I Iwuoha. Detection of Prostate Cancer using a Novel Tungsten Telluride Quantum Dot based Aptasensor. *Submitted to Biosensors and Bioelectronics.*

Table of Contents

List of Symbols

A - Geometric Area of Electrode

D- Interplanar Spacing

E_p - Peak Potential

E_{pa}- Anodic Peak Potential

E_{pc} - Cathodic Peak Potential

I_p- Peak Current

I_{pa}- Anodic Peak Current

I_{pc} - Cathodic Peak Current

D_o - Diffusion Coefficient

C_o- Concentration

K - Scherrer Constant

R - Ideal Gas Constant

θ – Theta

β - Beta

h - Plancks Constant

α- absorption coefficient

υ- Scan rate

ɼ- Surface Concentration

λ- Wavelength

T- Temperature

ω - Radial Frequency

List of Figures

List of Schemes

List of Tables

CHAPTER ONE

CHAPTER 1

INTRODUCTION

1.0) Overview

This chapter describes the aspects involved in the study. Topics like prostate cancer, early detection of the disease, biomarkers, quantum dots, nanotechnology, linking agents as well as aptamers are all discussed. The reason for the study is motivated and the problem statement is also addressed.

1.1) Background

Prostate cancer, commonly referred to as adenocarcinoma of the prostate, is the leading cause of cancer death in men in 46 countries, and it was estimated that by the end of 2018 there would approximately be 1.3 million new cases of prostate cancer worldwide.[1] Prostate cancer can be described as an uncontrollable growth of cells in the prostate glandular tissue, this gland is about the size and shape of a walnut[2] and is located just below the bladder through which the urethra flows. The prostate gland plays an important role in fertility, as it secretes an alkaline fluid that constitutes about 20-30% of the total volume of seminal fluid,[3] and complications such as growth or swelling of a benign or a malignant tumour present in this area could also result in complications associated with urine flow throughout the urethra.[4] Prostate cancer tumours if not controlled could metastasize spreading cancer to areas other than the primary area.

Risk factors for prostate cancer before the 1980's were primarily based on age, race and family history.[5] However, upon approval by the Food and Drug Administration (FDA) in 1994, prostate specific antigen (PSA) screening of men over the age of 55 resulted in greater statistical analysis. Prostate specific antigen refers to a glycoprotein[2] produced by normal as well as malignant cells of the gland itself, and is the current biomarker used for prostate cancer diagnosis. The national institutes of health biomarkers definitions working group defined a biomarker as a *'characteristic that is objectively measured and evaluated as an*

indicator of normal biological processes, pathogenic processes or pharmacologic responses to a therapeutic intervention'.[6]

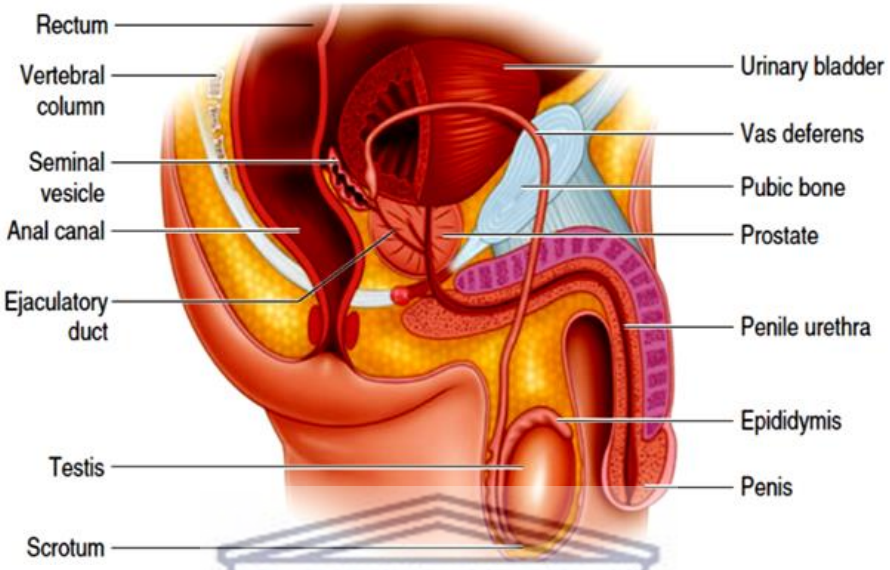

Figure 1. 1: Side view of male pelvis and relation of all components to the prostate. Reprinted from (M. Sharma, S. Gupta, B. Dhole and A. Kumar, The prostate gland, Basics of human andrology, *Springer nature* Singapore, 2017, 17-19.

However, one of the biggest drawbacks of PSA as a biomarker for prostate cancer diagnosis or prognosis is that it is not specific to prostate cancer but extends to benign prostate hyperplasia (refers to a condition in which the prostate swells uncontrollably, but it does not extend to cancer). As such elevated PSA levels during screening for prostate cancer are usually accompanied by a digital rectal exam (DGE) as a follow up to confirm the presence of a benign or malignant tumour. Even so, after a DGE it still isn't clear whether the patient has a benign or malignant tumour present, so the final step is to do a biopsy, which is often invasive and painful. During this biopsy two different types of tissue cells in the prostate are collected, and are rated according to the Gleason score grading system.[7] The Gleason score grading system defines five different cell growth patterns which can be studied under a microscope. Once cancer cells are extracted during a biopsy they are first classified into primary and secondary grades, these grades refers to cells that make up the largest and second largest parts of the prostate, respectively. Obtained cells are then classified into one of five cell growth patterns and rated on a scale of 1-5. The scores for both the primary and

secondary grades are then added to form the total Gleason sum. Scores of 6 suggest a moderate growing cancer whereas scores of 7 or higher indicate an aggressive cancer.[7]

1.2) Problem Identification

Cancer is a major epidemic that leaves patients and families devastated, which can take a toll on our economy, not only due to expensive medical care resources and trials, but also loss of human capital in cases of mortality.[8] It is reported that prostate cancer is the most common cancer in men across all population groups in South Africa.[9] According to data from the South African National Cancer registry the incidence rate of prostate cancer in South Africa has increased from 24.9 per 100 000 in the year 2007 to 67.9 per 100 000 in the year 2012, and it is still rising.[10]

Early detection of the disease is important in terms of controlling the cancer before it metastasises and spreads to other areas of the body. Currently the screening for prostate cancer biopsies are mainly based on high PSA levels or abnormal digital rectal examination.[11] For a PSA test serum levels above threshold value of 4.0 ng/mL are regarded as a 'positive' test. Patients should then follow up with a biopsy to distinguish between benign and malignant tumours.[12] The specificity of the PSA test for screening prostate cancer in patients which display intermediate PSA levels was reported to be only 20% at a sensitivity of 80% .[13,12] Due to the low specificity of PSA, false-positive results are a reality which can lead to unnecessary medical expenses as well as emotional strain.[14] Hence, the need for highly specific biomarkers towards detecting prostate cancer are of utmost importance. AMACR (Alpha-Methylacyl-CoA Racemase), an enzyme involved in peroxisomal beta-oxidation of dietary branched-chained fatty acids is a promising biomarker for prostate cancer, since it has a sensitivity of 83% with a specificity of 88% towards the disease.[15,12] AMACR also known in most cancer literature as (P504S) has been proven as one of the few biomarkers that can help distinguish cancer from benign and malignant cells for prostate carcinoma.[16] This biomarker can also be detected non-invasively from urine samples, unlike PSA which is usually conducted as a blood test.

Screening for early diagnosis of prostate cancer relies heavily on traditional methods such as cell morphology primarily using staining of tissue and microscopy. These methods are invasive and often not conclusive as tissue removal during a biopsy could miss cancer cells in

the earlier stages of the disease.[17] Waiting periods for these tests is often long and gruesome not to mention expensive as well. Hence, the need for non-invasive, rapid point of care testing, which can generate results in real time, does not require a skilled individual to operate and should be cost effective. A solution to this is known as electrochemical biosensors.[18] Electrochemical biosensors have recently made huge progress in terms of aiding the diagnosis and the monitoring process of many diseases.[19] Biosensors offers a compact solution for the detection of specific analytes to make a trustworthy medical diagnosis.[20] The sensitivity and specificity of a biosensor can be fine-tuned by incorporating nanomaterials[21] as a mediating platform between the sensing component and the transducer. Nanomaterials has many amazing properties such as increased surface area, electrical properties, luminescent as well as optical properties which can be manipulated for biological sensor applications. Studies have shown that quantum dots in particular offer a good biocompatibility as well as sensitivity in providing an interface between an electrode surface as well as a biological recognition component.[22]

1.3) Research Aims and Objectives

Thus, the aim of this study was to develop a quantum dot (QD) modified biosensor for the determination of an emerging prostate cancer biomarker known as AMACR. The electrochemical biosensor (in this case aptasensor) was developed by incorporating tungsten telluride quantum dots capped with mercaptosuccinic acid, which was used as an electron mediator between the transducer and the aptamer specific to AMACR.

The aim was achieved by objectives outlined below:

- Synthesis of Tungsten Telluride (WTe_3) quantum dots capped with mercaptosuccinic acid (MSA) via an aqueous route.
- Investigating the microscopic properties of MSA-WTe_3 quantum dots using high-resolution transmission electron microscopy (HR-TEM), and high-resolution scanning electron microscopy (HR-SEM) to determine the particle size and shape. Confirming the size of the MSA-WTe_3 QDs by small angle X-ray scattering (SAXs) and the elemental composition was confirmed by energy dispersive X-ray spectroscopy (EDS).

- Confirming the crystal structure of quantum dots by the use of X-ray Diffraction Spectroscopy (XRD).
- Using ultraviolet-visible (UV-Vis) spectroscopy to determine all bandgaps.
- Studying the electrochemical behaviour of quantum dots using cyclic voltammetry (CV) as well electrochemical impedance spectroscopy (EIS)
- Fabrication of the QDs based aptasensor and characterization by CV and EIS.
- Electrochemical detection of the AMACR biomarker by differential pulse voltammetry (DPV).

Conclusion

Prostate cancer is a major epidemic that leads to loss of many lives each year, currently the FDA approved biomarker for prostate cancer detection PSA is not specific to the cancer itself and has a high risk of false positive results. In order to improve diagnosis of the disease and to minimize the risk of unnecessary biopsy and overtreatment, a biomarker with a greater specificity towards the disease is needed. A proposed biomarker for this application is known as AMACR, which according to literature is overexpressed in patients with prostate cancer; yielding a much better diagnosis than that of PSA. A way in which prostate cancer diagnosis could become more efficient, reliable, non-invasive as well as economical is by the use of electrochemical aptasensors for the sensitive detection of disease related biomarkers. Nanomaterial can be used to fine-tune the sensitivity of an electrochemical aptasensor. Nanomaterial has great electrical, thermal and optical properties compared to their bulk material. Quantum dots are an example of this and through incorporation of this material into the electrochemical aptasensor, ultimate sensitivities can be achieved towards biomarker detection. Hence, this study proposes a potential electrochemical aptasensor for the rapid, cost effective and sensitive detection of an emerging prostate cancer biomarker known as AMACR.

References

1 F. Bray, J. Ferlay, I. Soerjomataram, R. L. Siegel, L. A. Torre and A. Jemal, Global cancer statistics 2018: GLOBOCAN estimates of incidence and mortality worldwide for 36 cancers in 185 countries., *CA. Cancer J. Clin.*, 2018, **68**, 394–424.

2 G. G. Miklos, The dilemmas of prostate cancer screening, *Med. J. Aust.*, 2013, **199**, 582.

3 A. Sharma, mona. Gupta, Surabhi. Dhole, Bodhaka. Kumar, in *Basics of Human Andrology*, Springer Healthcare, Singapore, 2017, pp. 17–35.

4 F. F. Vasanwala, M. Y. C. Wong, H. S. S. Ho and K. T. Foo, Benign prostatic hyperplasia and male lower urinary symptoms: A guide for family physicians, *Asian J. Urol.*, 2017, **4**, 181–184.

5 J. M. Chan, M. J. Stampfer and E. L. Giovannucci, What causes prostate cancer? A brief summary of the epidemiology, *Semin. Cancer Biol.*, 1998, **8**, 263–273.

6 K. Strimbu and J. A. Tavel, What are biomarkers?, *Curr. Opin. HIV AIDS*, 2010, **5**, 463–466.

7 N. Chen and Q. Zhou, The evolving gleason grading system, *Chinese J. Cancer Res.*, 2016, **28**, 58–64.

8 R. Etzioni, N. Urban, S. Ramsey, M. McIntosh, S. Schwartz, B. Reid, J. Radich, G. Anderson and L. Hartwell, The case for early detection, *Nat. Rev. Cancer*, 2003, **3**, 243–252.

9 H. A. Le Roux, R. J. Urry, B. Sartorius and C. Aldous, Prostate Cancer at a regional hospital in South Africa: We are only seeing the tip of the iceberg, *South African J. Surg.*, 2015, **53**, 1–6.

10 C. Babb, M. Urban, D. Kielkowski and P. Kellett, Prostate cancer in South Africa: pathology based national cBabb, C., Urban, M., Kielkowski, D., & Kellett, P. (2014). Prostate cancer in South Africa: pathology based national cancer registry data (1986-2006) and mortality rates (1997-2009). Prostate Canc, *Prostate Cancer*, 2014, **2014**, 419801.

11 R. Nagarajan, M. Sciences, E. Team and K. Street, Nanoparticles: Building Blocks for

Nanotechnology - Google Books, 2008, 2–14.

12 D. K. Yang, L. C. Chen, M. Y. Lee, C. H. Hsu and C. S. Chen, Selection of aptamers for fluorescent detection of alpha-methylacyl-CoA racemase by single-bead SELEX, *Biosens. Bioelectron.*, 2014, **62**, 106–112.

13 W. J. Catalona, M. A. Hudson, P. T. Scardino, J. P. Richie, F. R. Ahmann, R. C. Flanigan, J. B. DeKernion, T. L. Ratliff, L. R. Kavoussi, B. L. Dalkin, W. B. Waters, M. T. MacFarlane and P. C. Southwick, Selection of optimal prostate specific antigen cutoffs for early detection of prostate cancer: Receiver operating characteristic curves, *J. Urol.*, 1994, **152**, 2037–2042.

14 K. M. Koo, E. J. H. Wee and M. Trau, Colorimetric TMPRSS2-ERG gene fusion detection in prostate cancer urinary samples via recombinase polymerase amplification, *Theranostics*, 2016, **6**, 1415–1424.

15 P. Y. Lin, K. L. Cheng, J. D. McGuffin-Cawley, F. S. Shieu, A. C. Samia, S. Gupta, M. Cooney, C. L. Thompson and C. C. Liu, Detection of alpha-methylacyl-CoA racemase (AMACR) A biomarker of prostate cancer, in patient blood samples using a nanoparticle electrochemical biosensor, *Biosensors*, 2012, **2**, 377–387.

16 Z. Jiang, B. A. Woda, C. L. Wu and X. J. Yang, Discovery and clinical application of a novel prostate cancer marker: α-methylacyl CoA racemase (P504S), *Am. J. Clin. Pathol.*, 2004, **122**, 275–289.

17 I. E. Tothill, Biosensors for cancer markers diagnosis, *Semin. Cell Dev. Biol.*, 2009, **20**, 55–62.

18 L. Xu, Y. Wen, S. Pandit, V. R. S. S. Mokkapati, I. Mijakovic, Y. Li, M. Ding, S. Ren, W. Li and G. Liu, Graphene-based biosensors for the detection of prostate cancer protein biomarkers: A review, *BMC Chem.*, 2019, **13**, 1–12.

19 Y. Saylan, Ö. Erdem, S. Ünal and A. Denizli, An alternative medical diagnosis method: Biosensors for virus detection, *Biosensors*,Biosensors,2019 , DOI:10.3390/bios9020065.

20 C. Moina and G. Ybarr, Fundamentals and Applications of Immunosensors, *Adv. Immunoass. Technol.*, , DOI:10.5772/36947.

21 N. M. Noah and P. M. Ndangili, Current Trends of Nanobiosensors for Point-of-Care Diagnostics, *J. Anal. Methods Chem.*, , DOI:10.1155/2019/2179718.

22 S. J. Rosenthal, J. C. Chang, O. Kovtun, J. R. McBride and I. D. Tomlinson, Biocompatible quantum dots for biological applications, *Chem. Biol.*, 2011, **18**, 10–24.

CHAPTER TWO

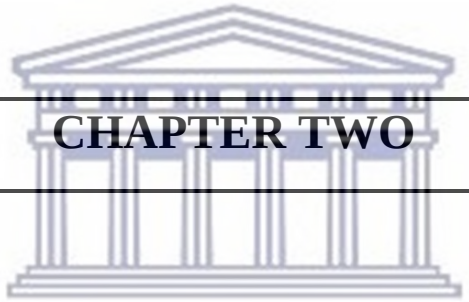

CHAPTER 2

LITERATURE REVIEW

2.0) Overview:

This chapter gives an overview on the background of QDs and their importance as surface materials in sensor fabrication systems. This chapter also deals with explaining what electrochemical sensors are and the types of sensors fabricated for different types of applications. Furthermore, this chapter gives insight into biological markers and their importance as identifiers for diseases diagnosis. In addition, this chapter outlines the working principles of the characterization methods used in this study.

2.1) Sensors

A sensor can be described as a device containing a specific recognition component, either chemical or biological which is designed in such a way as to target an analyte; and a physical transducer which converts the recognition process into a measurable signal.[1]

Globally many different types of sensors are used daily since people often rely on them for safety, health and environmental reasons. Examples of sensors include environmental sensors, food sensors and biosensors; all of these areas may overlap depending on the specific application of the sensor and the desired outcome. Environmental sensors refers to sensors which monitor the environment and are often used to protect the public from harmful pathogens or toxic contaminants.[2] The three things which are generally monitored in environmental sensors are air,[3] water[4] and soil.[5] An example of a water sensor is described in the work done by Liu et al, 2010, where a fluorescence sensor was designed in order to detect cyanide concentrations in water, which is harmful to both humans an aquatic life.[6] Food sensors are in high demand in the food industry as to make sure that food is kept free of toxic material as well prolonging its shelf life and reducing spoilage.[1] In the work done by Fu et al, 2008 a food sensor based on nanotechnology for the detection of salmonella was successfully

fabricated.[7] In the following section focus will be directed towards biosensors since this study dealt with the fabrication and application of a sensor for cancer disease diagnosis.

2.2) Biosensors

Biosensors since its first introduction in 1956 by the American biochemist Leland C Clark (for his work in oxygen detection), has become an increasing area of interest and relevant research has grown rapidly over the past few decades,[8] it was also Clarks work in 1962 which laid down the ground work for the modern day glucose sensor.[9]

A biosensor according to IUPAC can be stated as " a device that uses specific biochemical reactions mediated by isolated enzymes, immunosystems, tissues, organelles or whole cells to detect chemical compounds usually by electrical, thermal or optical signals".[10]Biosensors can also be classified as point-of-care (POC) devices which yield results in real time, whether it is at home or in the doctor's surgery. The main aspects which constitutes a good biosensor is its ability to be easily operated, inexpensive, rapid and robust.[11] A typical biosensor and its components are depicted in Figure 2.1 below.

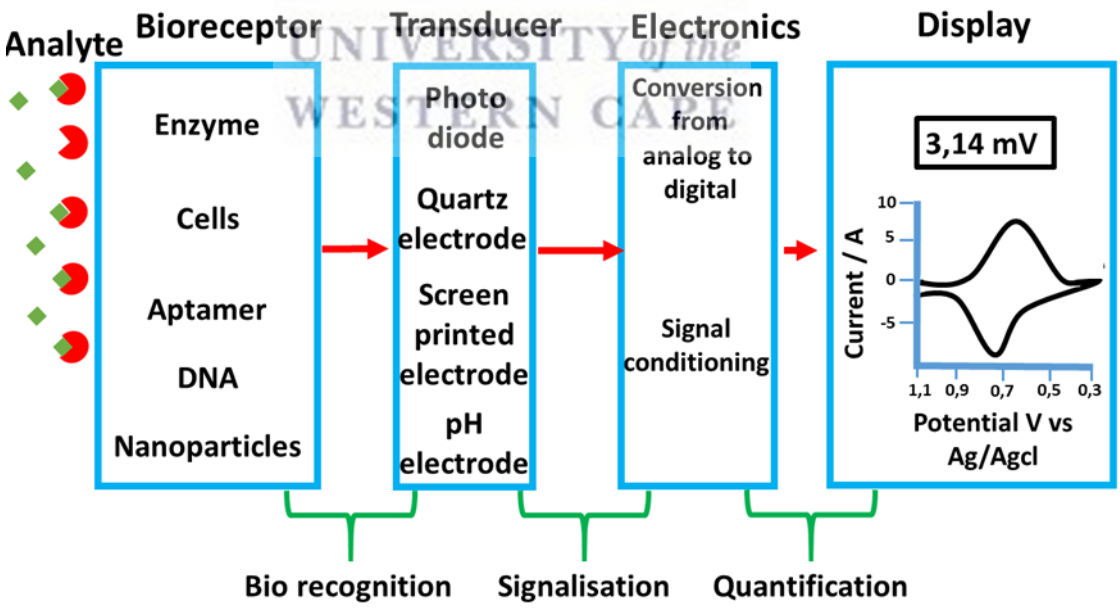

Figure 2. 1: Main components which constitutes a biosensor. Reprinted from N. Bhalla, and co-workers, Introduction to biosensors, *Essays in biochemistry* 2016, 60, 1-8.

A typical biosensor consists of five main components, that is:

- Analyte: an analyte refers to a substance/biomarker/chemical that needs to be detected or quantified
- Bio-recognition component: This is a biological molecule, either an aptamer, single stranded DNA, enzyme or anti-body that is used to detect the analyte of interest.
- Transducer: A transducer is an important part of the biosensor that converts a biological event into an electronic signal depending on the application of the sensor, different types of transducers exist and will be discussed below.
- Computer/electronics: This is the part of the biosensor that processes information from the transducer and prepares it in a way that is easy for the user to understand.
- Display/output: This allows the user to interpret information from the biosensor in the form of curves, graphical depictions as well as numbers which are understandable to the user and correlate to a biochemical change, event or specific concentration related to the analyte of interest.[9]

Biosensors can be classified by the types of bio-receptors or transducers present. Depending on the type of transducer used biosensors can be classified into four main classes, that is, optical biosensors, thermal biosensors, piezoelectric biosensors as well as electrochemical biosensors. Optical biosensors have transducers which measures the changes in optical properties of a specific analyte, these changes could be due to, absorbance, fluorescence, reflectance, refractive index, phase shift as well as wavelength.[12] Thermal biosensors on the other hand measures changes in temperature which are generated by biological reactions. Here, thermometric measurements are based on either heat evolved or heat absorbed during a biochemical reaction, these heat changes are directly proportional to molar enthalpy and thus proportional to the total number of product molecules created by the biochemical reaction.[13] Piezoelectric biosensors are based on the piezoelectric effect; this phenomenon refers to the ability of anisotropic crystals to produce a voltage when mechanically stressed. The opposite effect is also experienced when an alternating voltage is applied to any anisotropic crystal which in turn causes mechanical stress or oscillation. Thus, when an analyte is bound to the surface of a crystal it can be directly detected by the changes in frequency experienced after applying an alternating voltage.[14] The final class of biosensors are known as electrochemical

biosensors, here the transducer is electrochemical, and electrical properties could be measured by methods such as potentiometry, voltammetry, conductometry and impedance. The following sections below will give a brief overview of each.

2.3) Electrochemical Biosensors

In order to understand how electrochemical biosensors work, one first has to understand the working principle of an electrochemical cell. An electrochemical cell typically consists of a three electrode system; a working electrode (WE), a reference electrode (RE) and a counter electrode (CE).[15] These electrodes work together to form the basis of an electrochemical biosensor in the following way: A WE is usually the electrode of interest, all redox reactions takes place here,[16] as well as immobilization of the bio-receptor material. The CE could sometimes act as a RE in a two electrode system, however, the CE closes the current circuit as it provides the flow of electrons between itself and the working electrode.[15] The RE produces a reversible, stable and reproducible potential throughout the electrochemical reaction as to stabilize any event that occurs at the working electrode, usually a REDOX reaction.[16] The RE is usually not polarized by the flow of current as it sits outside the main circuit that exist between the CE and WE in an electrochemical cell. Other type of electrochemical cells besides the conventional three-electrode and two-electrode systems exist, these are known as screen printed electrodes (SPE) which encompasses a typical three-electrode system onto a single platform. Here, the WE, CE, and RE are printed onto a polymer material with a hard disc as a supporting substrate. Screen printed electrodes have advantages over conventional electrodes as it is easily mass produced and contains a simple electrochemical setup.[15]

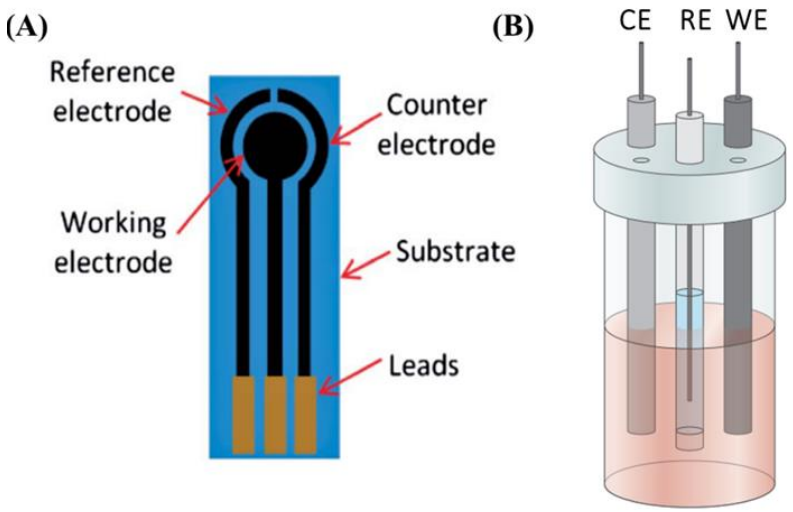

Figure 2. 2: : A typical screen printed electrode including its working components (A). Reprinted from K. Mistry and co-workers, A review on amperometric-type immunosensors based on screen printed electrodes; Royal society of chemistry. *Analyst*, 214, 139, 2289-2311. A conventional three electrode cell setup consisting of WE, CE and RE (B). Reprinted from K. Less and co-workers, Electrochemical and spectroscopic methods for evaluating molecular electrocatalyst, *Nature reviews; Chemistry*, 2017, Vol 1, article number 0039.

2.3.1) Transducers

Electrochemical biosensors can be further defined by the type of detection methods used, that is, potentiometric, voltammetric, conductometric or impedometric.

2.3.1.1) <u>Potentiometric</u>

Potentiometric sensors work by measuring the difference in potential between two electrodes under the condition that there is no current flow, the signal of a potentiometric biosensor is primarily based on the Nernst equation which states that the outcome/voltage difference is linearly related to the logarithm function of the activity of the ion species in solution. Meaning this method of detection can detect really small amounts and still release a signal.[17]

$$E = E^0 + \frac{RT}{nF}\ln[a_i] \qquad [2.1]$$

*Equation 2.1: Nernst equation (***E** = Potential (V)/ potential difference in the electrochemical cell; **R**= ideal gas constant= (8.314 J/K); **F**= Faradays constant (965485 C/mol) ;**n** = number of electrons / number of primary ions in solution ; **a**= activity of the ion in solution ; **E^{o}** = standard potential)

In the work done by Wang et al, 2010, cancer biomarker carcionoembryonic antigen (CEA) was detected using a potentiometric assay. This assay was based upon a gold coated silicon chip, which consisted of co-absorption of both hydroxyl terminated alkanethiol and template biomolecules. It works via the adsorption of biomolecules, which can then be removed creating a footprint/cavity on the chip. Re-adsorption of the same biomolecule then causes changes to the sensing chip potential and can be measured potentiometrically.[18]

2.3.1.2) Voltammetric

Voltammetric electrochemical sensors are generally based upon applying a varying potential to a working electrode and then measuring the resulting current.[19] The current generated by applying a range of potentials is directly proportional to the concentration of the electroactive species present in solution. Different types of voltammetric methods exist, such as cyclic voltammetry (CV), differential pulse voltammetry (DPV), linear sweep voltammetry (LSV), square wave voltammetry (SQV) as well as stripping voltammetry (SV).[20]

Cyclic voltammetry- Potential is applied between two points and then reversed back to the start again, while maintaining a constant potential scan rate.[21]

Square wave voltammetry- Potential is pulsed in the forward and reverse direction, and the resulting current is then sampled at each point. [22]

Differential pulse voltammetry- Potential is pulsed and superimposed on a staircase like waveform.[22]

Linear sweep voltammetry- Similar to CV but potential is only swept in one direction at a constant potential scan rate.[21]

Stripping voltammetry- Consists of two common steps, first analyte of interest is electrodeposited onto a working electrode. Once the analyte is bound, the WE is then scanned

at a potential intended to strip the material off the electrode which produces a resulting current characteristic to the REDOX reaction which took place at the WE.[23]

In the work done by Zhang et al, 2007, prostate specific antigen (PSA) a current biomarker for prostate cancer, was detected using a voltammetric enzyme linked immunoassay system with a reported limit of detection to be 10 ng/mL .The detection of PSA was done using a double antibody sandwich assay method, equipped with 3, 4 diamminobenzoic acid and horseradish peroxidase which oxidized to form an electroactive species. This species enabled second order derivative linear sweep voltammetry for the sensitive detection of PSA in human serum.[24]

2.3.1.3) Conductometric

Conductometric electrochemical sensors are based on the conductivity of a bulk solution or a thin film, here the conductivity of a thin electrolyte layer is measured adjacent to the electrode surface.[25] The conductivity is generally affected by the type of analyte present, and continuous dissociation of the dissolved substance occurs as more ions are produced, resulting in ion migration when induced by an electric field.[26] All of these factors then contribute to changes in conductivity of the bulk solution and these changes could be accounted for by different concentrations of analyte present in solution. Advantages of these types of electrochemical biosensors are: they are cost effective and can easily be mass produced; and possible multi-analysis depending on its application and fabrication in comparison to bulky desktop machinery such as HPLC.[26]

In the work done by Adams et al, 2008, circulating tumour cells were detected using an integrated microfluidic sensor. Circulating tumour cells were first isolated from whole blood samples using a microfluidic process by capturing circulating tumour cells in channels. Isolated tumour cells were then detected and quantified by the use of a conductometric electrochemical sensor.[27]

2.3.1.4) Impedimetric

Impedance first made an introduction into electrical engineering by Oliver Heaviside in the early 1880's,[28] who adapted complex numbers to study electrical circuits.[29] Electrochemical

impedance spectroscopy (EIS) is an electrochemical characterization technique that operates in the frequency domain and can be measured by applying an AC potential to an electrochemical cell and measuring the resulting current.[29]

Usually a small excitation signal is used to measure EIS as to keep the cells response pseudo linear. This is because a linear system produces a sinusoidal current response at the same frequency as that of the applied potential, however, it is shifted in phase.[22] Electrochemical impedance is an electrochemical technique which is simple to operate, sensitive in its detection and non-destructive to biological material or samples (due to low potential applied).[30] In the work done by Liu et al, 2014, a sensitive impedimetric electrochemical sensor for the detection of tumour biomarkers was developed. This sensor was based on an aptamer affinity and made use of silver nanoparticles to amplify detection.[31]

2.3.2) Bio-recognition components

So far biosensors have been classified according to their methods of transduction, however, they can also characterized by their biological recognition components used for detection of specific analytes. In Scheme 2.1 below an account for the different classifications of biosensors are represented.

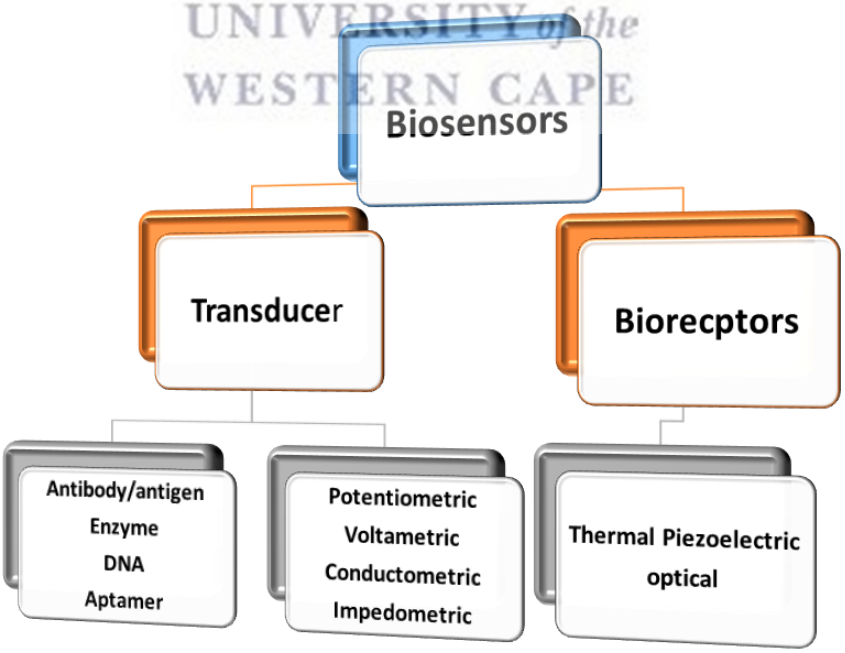

Scheme 2. 1: Showing classes of biosensors in terms of bio-receptors and transducers used.

2.3.2.1) Immunosensors

Immunosensors refers to an electrochemical biosensor which is based upon antibody/antigen interactions. The principle of an immunosensor depends on a ligand binding affinity reaction between the target analyte, and a highly specific binding agent which is immobilized onto the transducer.[32] Figure 2.3 shows a typical setup of an immunosensor which was reprinted from Zhang et al, 2018. Here, it was reported that an electrochemical immunosensor based on a glassy carbon electrode (equipped with octahedral gold nanoparticles) was fabricated for the detection of Ochratoxin A (a parasitic fungus found on contaminated crops, which poses a strong liver toxicity and possibly increases the chances of getting cancer after consumption). Zhang et al, 2019, reported a wide linear range from 0.1 pg/mL to 10 ng/mL, and limit of detection of 39 fg/mL for the detection of Ochratoxin A using an electrochemical immunosensor.[33] The sensor fabrication process is shown in Figure 2.3. The first step was immobilization of their nanomaterial onto the glassy carbon electrode surface. Next was the selective binding of an antibody specific to Ochratoxin A to the electrode surface, then bovine albumin serum (BSA) was used as a blocking agent to block any non-specific binding sites, and finally the now developed sensor was tested in the presence of Ochratoxin A, using methods such as electrochemical impedance spectroscopy (EIS) and cyclic voltammetry (CV).[33]

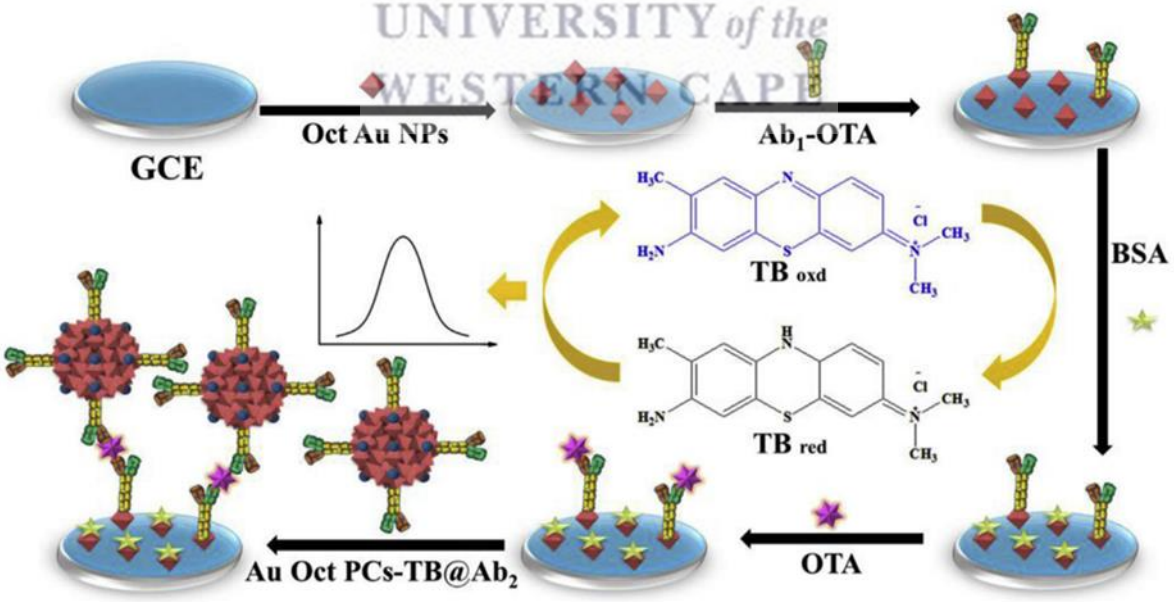

Figure 2. 3: An electrochemical immunosensor set-up, reprinted from T. Zhang and co-workers, Electrochemical immunosensor for Ochratoxin A detection based on Au octahedron plasmoniccolloidosomes, *Elsevier*, 2019, 0003-2670.

2.3.2.2) Genosensors

A genosensor on the other hand, also referred to in literature as an electrochemical DNA biosensor has a specific bio-receptor component, and this is known as a single stranded DNA (ssDNA) sequence. DNA in general consists of a double helix configuration, where its monomers are known as nucleotides. Once the single strands are separated they have a very high affinity for each other. The strands can re-join in a process known as hybridization which results in oxidation[34] of the nucleotides which make up each ssDNA. Thus, in a successful genosensor a ssDNA is used as a probe which is attached to an electrode, the complementary strand of DNA is usually suspended in solution for detection by the genosensor. Once hybridization occurs the oxidation event then generates an electrical signal which can be measured.[35] Figure 2.4 shows an electrochemical genosensor fabrication process reprinted from Senel et al, 2019. Here, an electrochemical DNA biosensor for the detection of a breast cancer gene BRAC1, based on self-assembled dendrimers are illustrated.[36]

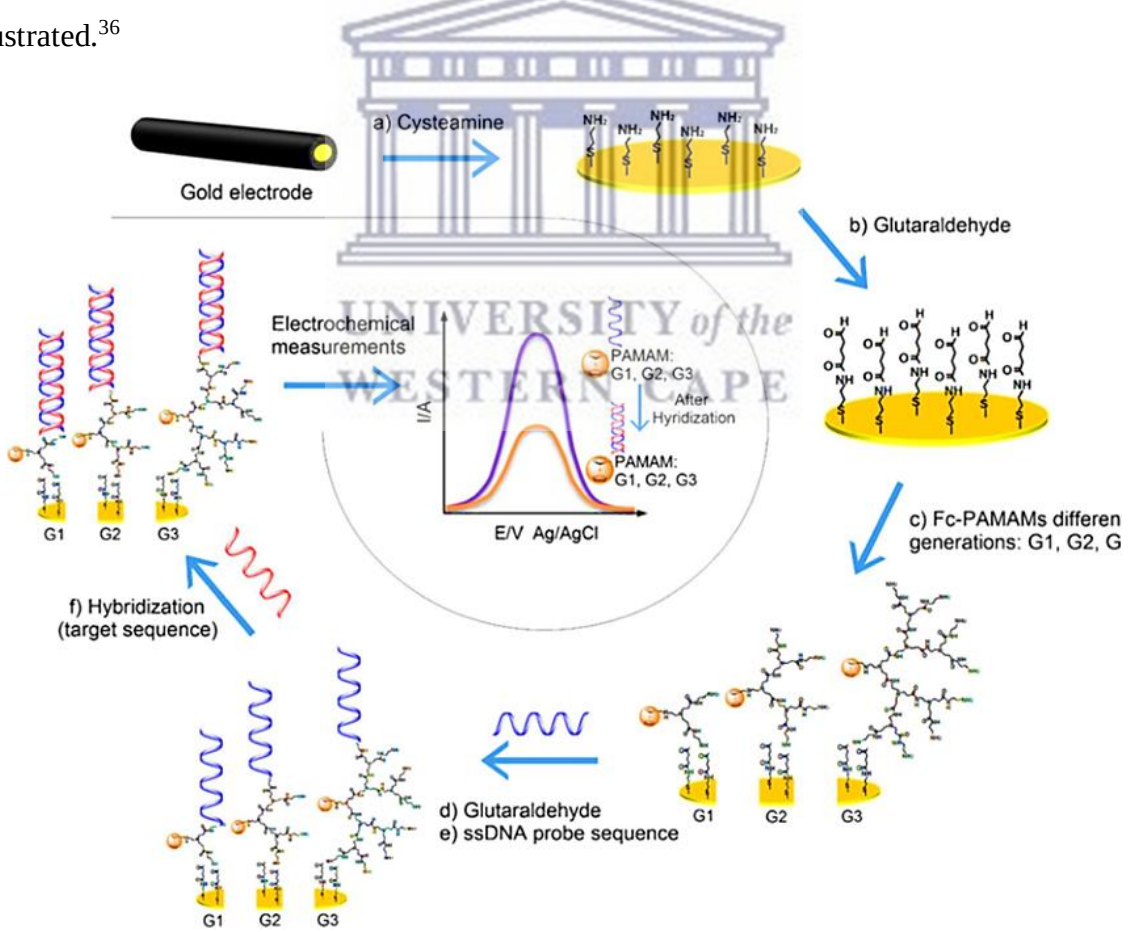

Figure 2. 4: Fabrication steps for the DNA biosensor based on three different generation self-assembled dendrimers to which single stranded DNA probe sequence was immobilized for

the detection of the target sequence via a hybridization mechanism shown above. Image reprinted from M. Senel, and co-workers, Electrochemical DNA biosensors for label free breast cancer gene marker detection, *Analytical and Bioanalytical Chemistry*, 2019, 2925 – 2935.

From Figure 2.4 it can be seen that cysteamine and glutaraldehyde was used as linking agents in order to immobilize different generation dendrimers onto the electrode surface, glutaraldehyde was then again used to immobilize ssDNA specific to the target sequence. The target was 'detected' via a hybridization reaction between the ssDNA probe sequence and the target itself, this then generated an electrochemical response which was then measured.[36]

2.3.2.3) <u>Aptasensors</u>

Aptasensors have recently gained a lot of interest in the detection of analytes such as cancer biomarkers,[37] bacteria[38] and general environmental and food contaminants.[39] Biosensors which consist of an aptamer are formally known as an aptasensor. Aptamers are single stranded nucleic acids which are isolated using method called SELEX (Systematic evolution of ligands by exponential enrichment).[40] This process works by generating nucleic acid ligands (aptamers) against many small molecules such as amino acids, proteins and drugs. Aptamers are then isolated from a library of different synthetic nucleic acids which are specific to the target molecule, it works through an adsorption, recovery and re-amplification process.[41]

The in vitro SELEX process as shown in Figure 2.5 below consists of four main steps, that is, (i) the introduction of the target molecule to an already acquired library of random DNA/RNA molecules;[42] (ii) the specific DNA/RNA molecules gravitation towards the surface of the target till it is physically bound; (iii) separation of bound material from unbound material until only the target molecule and its specific counterpart are captured; and finally (iv) the amplification of the DNA/RNA molecules which match the analyte in order to form the appropriate aptamer sequence.[43]

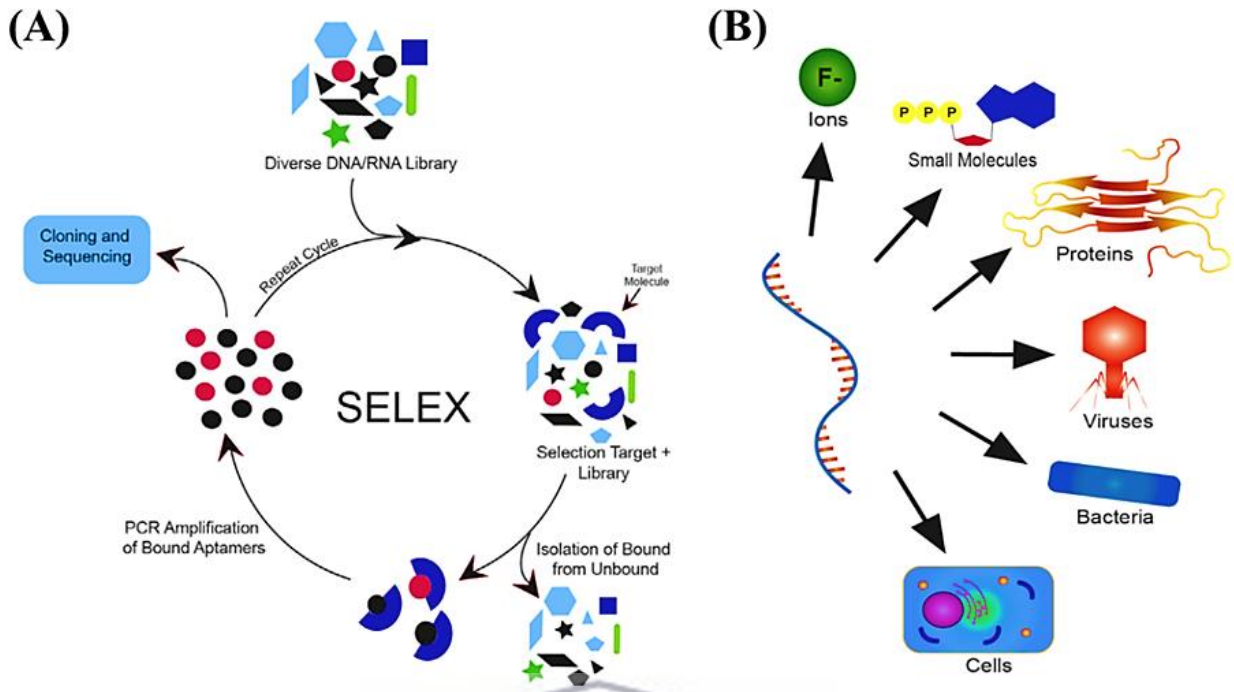

Figure 2. 5: (A) Showing the in vitro SELEX process, (B) showing diverse molecules which can be detected by aptamers. Reprinted from Y. Wu, and Y. Kwon, Aptamers: The "evolution" of SELEX, Methods, *Elsevier*, 2016, 1046-2023.

Aptamers can specifically recognize a range of targets including cells, proteins and small molecules.[40] This is possible because the aptamer undergoes a conformational change when interacting with analytes of interest to form three dimensional structures which often wrap around its targets.[44] Aptamers has many advantages in comparison to antibodies, as they are easily modified, has a higher selectivity, good temperature stability, as well as a large surface density which contributes to greater binding properties.[15]

Immobilization procedure of an aptamer plays a really crucial role in the fabrication of an aptasensor, as the orientation of the aptamer plays a huge role in the aptasensor's performance.[45] Factors such as affinity, specificity and stability of the aptamer are all affected by its immobilization onto the sensor surface. The reason for this is the orientation of the aptamer has to be correct in order to maximize its stability, also the aptamer needs to be immobilized in such a way as to minimize non-specific binding and to ensure binding to the analyte is made easier.[45] There are different immobilization methods these include: physical adsorption, chemical adsorption, streptavidin/avidin/neutravidin-biotin interaction as well as covalent attachment via functional groups.[46] Physical adsorption relies on electrostatic forces

to hold the aptamer onto the transducer/electrode; this method is simple given that the aptamer does not have to go through any initial modification steps. The other three methods all require modification of the aptamer either via a thiol group, a biotin protein or an amino group.[45] In the present study immobilization of the aptamer to the sensor surface was achieved via covalent attachment. Aptamers are modified with chemical groups, such as amine or hydroxyl groups, these groups interact with terminal carboxylic groups which are activated using 1-ethyl-3-[3-dimethylaminopropyl]-carbodiimide hydrochloride (EDC)/N-hydroxysulfosuccinimide (sulfo-NHS).[47] This method can be performed on different types of electrodes, the functionalization/preparation of the surface of the electrode also plays a role in the type of modification the aptamer should undergo.[45] A way in which the sensitivity of aptasensors or biosensors can be increased is via the incorporation of nanomaterials[40] such as, quantum dots, nanorods, graphene and carbon nanotubes.

Nanomaterials play a huge role in the immobilization of aptamers onto electrode surfaces. It has many advantages as seen below:

- Nanomaterial has its own characteristic properties, such as good electrical and chemical properties.[48] Electrical properties and chemical properties help link aptamers to the electrode through covalent points of attachment.
- These nanomaterials act as a mediating platform for electron transfer from the aptamer to the transducer.[49] Hence, resulting in signal amplification for the biological redox event which occurs at the surface of the electrode.
- Its high surface area to volume ratio allows a larger surface area for aptamer immobilization, and in essence, greater detection of the analyte of interest.[50]

Table 2.1 shows an account for recent aptasensors which used nanomaterials for clinical and environmental analyte detection in the last decade.

Table 2. 1: Aptasensors enriched with nanomaterial over the past ten years.

Nanomaterial	***Electrode***	***Transduction***	***analyte***	***LOD***	***Bioreceptor***	***REF***
AuNp's	Au	EIS	IL-6	0.02*pg/ml*	Aptamer	(Kumar et al,2016)[51]
GQDs-AUNRs	SCE	EIS,DPV,CV	PSA	0.4*ng/ml*	Aptamer	(Srivasta et al,2018)[52]
CdSe QDs	GCE	DPV	Thrombin	0.08*μg/ml*	Aptamer	(Li et al,2011)[53]
AuNP's/BNNS	FTO	DPV,EIS	Myoglobin	34.6g/ml	Aptamer	(Adeel et al,2019)[54]
GQD's	---	Fluorescence	Lead ions	0.6 nM	Aptamer	(Qian et al,2015)[55]
AuNP's	---	Fluorescence	AflatoxinB1	3.4nM	Aptamer	(Sabet et al,2017)[56]
GO films	Au-SCE	CV	BNP-32	0.9pg/ml	Aptamer	(Grabwaska et al,2018)[57]
SWNT	Au	DPV	Cocaine	105pM	Aptamer	(kumar et al,2016)[51]
AuNP's	---	Colorimetric	17b-estradiol	200pM	Aptamer	(Alsager et al,2015)[58]

Note: Interleukin-6 (IL-6); Prostate Specific Antigen (PSA); Brain natriuretic peptide (BNP); Screen printed electrode (SCE); Au (Gold electrode); Glassy carbon electrode (GCE); Fluorine doped tin oxide electrode (FTO); Screen printed gold electrode (Au-SCE). Electrochemical impedance (EIS); Differential pulse voltammetry (DPV); Cyclic voltammetry (CV); Gold nanoparticles (AuNP's); Graphene Quantum dots Gold nanorods composite (GQDs-AUNRs); Cadmium selenide quantum dots (CdSe-QDs); Boron nitride nano sheets (BNNS); Graphene Quantum Dots (GQDs); Graphene oxide (GO); Single walled carbon nanotubes (SWNT).

In this study aptamers were used as the bio-recognition component, and nanomaterials such as quantum dots used as a mediating platform between the electrode and the aptamer. The following section gives an overview of quantum dots types and uses.

2.4) Quantum dots

Quantum dots (QDs) first discovered around 1981 by Russian physicist Alexei Ekimov, in his time at the Vavilov State optics institute,[59] can be broadly described as nanocrystals composed of a semiconductor core (including group II-IV or group III-V elements) encased inside a shell which is made up of a second semiconductor material.[60] These nanocrystals has incredible properties compared to their bulk counterparts which make them useful in many fields such as medical diagnostics,[61] biological imaging,[62] electronics[59] and photovoltaics.[63] QDs sizes range from 2 nm to 10 nm. QDs has size tuneable fluorescence properties, broad excitation range, narrow emission spectrum high resistance to photo bleaching and a strong fluorescence.[64] The size tuneable properties of quantum dots refer to different colours observed in relation to the size of the quantum dots. When a semiconductor absorbs a photon of a certain amount of energy, an electron in the valence band is promoted to the conduction band, and an electron hole pair is generated (the hole is left behind in the valence band after the electron has been promoted to the conduction band).[65] The electron-hole pair is held together by a coulomb attraction and the pair is able to move around in the bulk material, similar to the Bohr model of the atom.[66] Once the radius of the electron orbit in the bulk material is smaller than the Bohr excitation radius, the electron and hole pair starts becoming 'squashed' resulting in a confinement energy. This phenomenon is known as the quantum confinement effect.[67] Thus, the energy shifts to higher levels or blue shifts once the 'squeezing' of the electron-hole pair becomes greater. In essence this means that as the QDs become smaller, the energy level becomes higher and as such results in a blue shift. Larger QDs will result in lower energy level and as such will red shift. Thus, the QDs wavelength of emission can be fine-tuned depending on its size. The composition of the QDs also plays a role in the wavelength of its emission.[61] QDs can be classified into three different types:

-Core type quantum dots

Core type QDs consist of a single component semi-conductor nanocrystal, with a uniform centre.

-Core shell quantum dots

Core shell QDs can be described as semiconductor nanomaterial which is embedded inside another material with a wider bandgap. By coating the nanocrystallites with a higher band

gap inorganic material, it will passivate the surface non-radiative recombination sites, thus resulting in improved photoluminescence quantum yields.[68]

-Alloyed quantum dots

These QDs on the other hand, are formed by alloying together two semiconductor materials which has different band gap energies. These QDs not only display different properties from their bulk material, but also display differences in their electrochemical properties of their parent material.[69]

2.4.1) Capping agents

Capping agents are frequently used to inhibit nanoparticle overgrowth as well as change the surface properties of the quantum dots based on their application.[70] Properties such as size, surface composition and metal composition influence the toxicity and ultimately the biocompatibility of QDs. QDs are classified as biocompatible when they form a dispersion within aqueous media with a pH of 7.4 and a temperature of approximately 37 degrees Celsius. Biocompatibility is achieved by introducing a stabilizing agent during the aqueous route synthesis. However, QDs synthesized organically can also become biocompatible by exchanging of surface capping ligands.[71]

An example of water soluble capping agents usually contain thiol functional groups such as mercaptosuccinic acid (MSA), mercaptopropionic acid (MPA), thioglycolic acid (TGA), glutathione (GSH), and L-cysteine.[61] These ligands consist of a thiol molecule at one end and a carboxylic molecule at the other end. The carboxylic molecule normally exists at the surface of the QDs and allows the QDs to be water soluble and also serves as a point of attachment for biomolecules.[72]

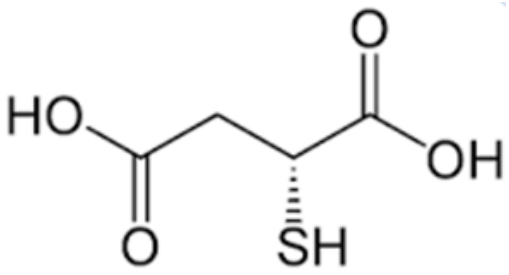

Figure 2. 6: Structure of mercaptosuccinic acid capping/stabilising agent.

In this study water soluble tungsten telluride QDs were successfully synthesized using mercaptosuccinic acid as a capping agent in order to allow the quantum dots to become biocompatible for use in an Aptasensor.

2.5) Biomarkers

A biomarker can be defined as a measurement that exists between any biological system and a potential threat. The measured response may be physiological or biochemical and is indicative of disease.[73] Many different forms of biomarkers exist, but they are mainly categorized into the following classes, predictive biomarkers, diagnostic biomarkers, prognostic biomarkers, staging biomarkers, as well as pharmacodynamic biomarkers.[74] Predictive biomarkers, indicates the potential threat of disease; diagnostic biomarkers, assist in disease diagnosis; prognostic biomarkers, provide the information needed to provide the best care and treatment for a particular disease, staging biomarkers, classify the stage of the disease; and pharmacodynamic biomarkers, predict the bodies response to treatment via drugs.[75] Most times a biomarker could fall into one if not more of these categories and give multiple information about a patient's wellbeing. Biomarkers are often graded by its sensitivity and specificity, where sensitivity refers to the percentage of individuals who have a particular disease and still test positive when screened via a biomarker. Specificity of a biomarker, however, relates to the percentage of individuals who do not have the disease but test negative when screened via test involving a biomarker related to the disease.[75] In this study an emerging biomarker known as Alpha-methylacyl-CoA racemase (AMACR) for prostate cancer was detected. A brief discussion on this biomarker follows below.

2.5.1) Alpha-Methylacyl-CoA Racemase

In order to understand the relevance of alpha-methylacyl-CoA racemase (AMACR) as an emerging biomarker for prostate cancer, one first has to become familiar with the current food and drug administration approved prostate biomarker that is used to screen men at risk for prostate cancer. This approved biomarker is known as prostate specific antigen (PSA).

PSA is a serine protease which is produced in high concentrations by normal and malignant prostatic tissue.[76] Its job is to help liquefy the semen after ejaculation, normally only small amounts are released into the blood stream from a healthy prostate, but larger amounts are released during prostatic disease. Even though PSA is considered a biomarker for prostate cancer; it can also be used as a marker for benign prostate hyperplasia (a case of severe swelling of the prostate).[77] For this reason, it is suggested that the specificity of PSA towards prostate cancer are low and as such can lead to unnecessary biopsies for patients who do not have the disease.[78] Furthermore, PSA is not a reliable marker for aggressive prostate cancers because at this stage the prostate produces less PSA, and the concentration of PSA present does not accurately predict the aggressiveness of the disease.[79] The following points outlined below describe the characteristics of an ideal biomarker for prostate cancer. The biomarker should correctly predict the significant presence or progression of prostate cancer with the main objective of eliminating unnecessary biopsies. The biomarker should contribute to reducing morbidity and unnecessary expenses, it should be detected non-invasively, and it should be specific to prostate cancer and not benign prostate hyperplasia.

AMACR is an enzyme that is involved in peroxisomal beta-oxidation of branched chain fatty acids.[79] Unlike PSA, AMACR is specific to prostate cancer and is not present in samples of males who have cases of severe benign prostate hyperplasia. It has been reported AMACR expression in prostate cancer has a specificity ranging from 88% to 100% and a sensitivity of 83% to 100%. In comparison to PSA (specificity of 20% and a sensitivity of 80%), AMACR seems like a reliable cancer biomarker which can be used to diagnose prostate cancer.[80]

2.6) Characterization Techniques

2.6.1) Spectroscopic Techniques

2.6.1.1) UV-Vis Spectroscopy

Ultraviolet-visible spectroscopy denoted by (UV-Vis) is a characterization technique associated with measuring the absorption of radiation (by an analyte of interest), as a function of wavelength.[81] It is a beneficial tool for characterizing nanoparticles/nanomaterials as they have optical properties that are sensitive to size, shape and concentration.[82] Each molecule consist of their own characteristic energy levels, which are discrete and can absorb significant amounts of radiation in the visible or ultraviolet region by causing an electron transition within its structure.[83] Energy supplied by visible or ultra-violet light can promote electrons from the ground state to an excited state orbital or antibonding orbitals. Possible electronic transitions which can occur by the absorption of either visible or ultra-violet light are listed below:

$\sigma \; to \; \sigma^*$

$n \; to \; \sigma^*$

$n \; to \; \pi^*$

$\pi \; to \; \pi^*$

Where, $\sigma \; and \; \pi$ refers to bonding orbitals, $\sigma^* and \; \pi^*$ refers to anti bonding orbitals and n refers to non-bonding orbitals respectively.[83]

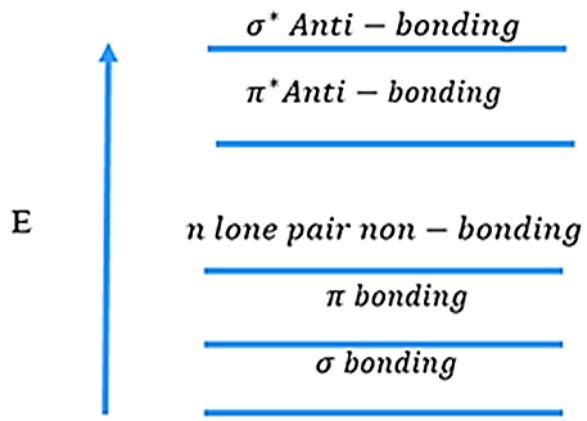

Figure 2. 7: Showing electronic transitions and their energies

Using the beer lamberts law the concentration of a sample can be calculated, this law relates the attenuation of light to the path length of the beam travelled as well as to the concentration of the absorbing species. This is given by Equation 2.2.[84]

$$A = -log_{10}\frac{P}{P_0} = abc \qquad [2.2]$$

Where,

A = absorbance

p_0 =intensity of the light emitted (cd)

P = intensity of the attenuated light after passing through the sample (cd)

a =absorptivity($L.mol^{-1}.cm^{-1}$)

b =path length(cm)

c =concentration of absorbing species ($mol.L^{-1}$)

Using the beer lamberts law the concentration of quantum dots can be calculated once the molar absorptivity is known. The size of quantum dots can also be approximated by UV-Vis in the following way: The minimum energy required to excite an electron from the valence

band to the conduction band of a quantum dot is dependent on its band gap. From this information a rough estimate of the quantum dot size can be estimated by fitting experimental data of absorbance versus wavelength of known particle size.[81] Qualitative information about quantum dots can also be extracted from its absorption data, such as size distribution, shape and crystal lattice information.[81]

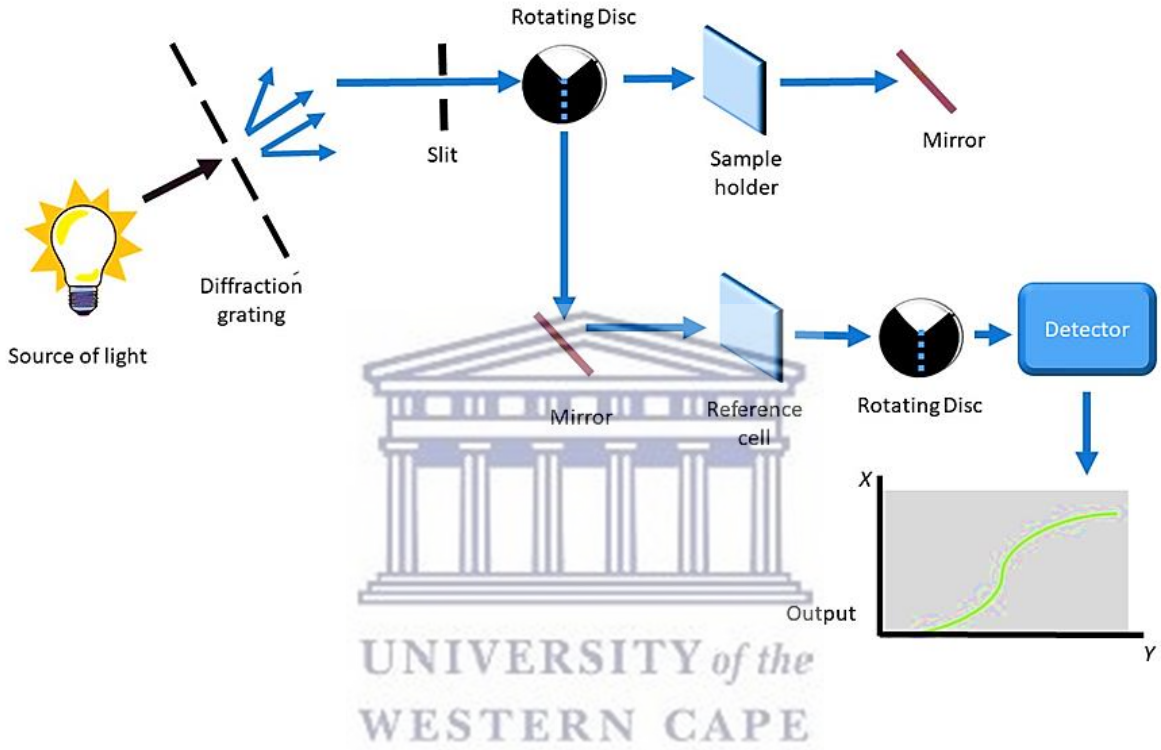

Figure 2. 8: Working principle of UV-Vis spectroscopy, figure reprinted from A. Oudhia, UV-Vis spectroscopy as a non-destructive and effective characterization tool for II-VI compounds; *Recent Research in Science and Technology*, 2012, 4(8): 109-111.

In UV-vis a deuterium lamp or tungsten/halogen lamp is used as the source of ultraviolet and visible radiation, respectively, in the range of 200 nm - 800 nm. This light passes through a diffraction grating (which is used to separate the light into its component wavelengths), and is then focused on to the sample compartment by making use of a slit. Once the beam of light passes through the sample the attenuation can then be measured by a detector.[85] A reference cell is used to measure only the solvent in which the analyte can dissolve, and its absorbance is then subtracted (background subtraction) from the analyte of interest, resulting in the

absorbance of the material itself and not its solvent.[81] Figure 2.8 shows the working principle of UV-Vis.

2.6.1.2) Fourier Transform Infra-red Spectroscopy

Fourier transform infrared spectroscopy (FT-IR) is a form of vibrational spectroscopy wherein the molecular structure and molecular environment of an analyte is studied.[86] FT-IR is a time saving method used to detect a range of functional groups, non-destructively. As it provides information based on the chemical composition and physical state of the sample.[87]

The operating principle of FT-IR is based upon irradiating a sample with infrared radiation, originating from an infrared source. The radiation absorbed by the sample then promotes the deposition of quanta of energy into vibrational modes. However, a molecule will only correspond to radiation that is related to its characteristic molecular modes of vibration. These changes of vibrational motion within a molecule give rise to the bands in a vibrational spectrum generated by FT-IR, each band is then denoted by its specific frequency and amplitude value.[86]

All molecules generally exhibit characteristic absorbance peaks which are expressed in reciprocal centimetres known as the wavenumber. These peaks are often described as the molecular fingerprints as peaks in the 1350 cm^{-1} to the 1000 cm^{-1} region give the most information about the sample analysed.[86] Figure 2.9 below, shows and example of a typical FT-IR spectrum, where a sample's main functional groups are expressed. [88]

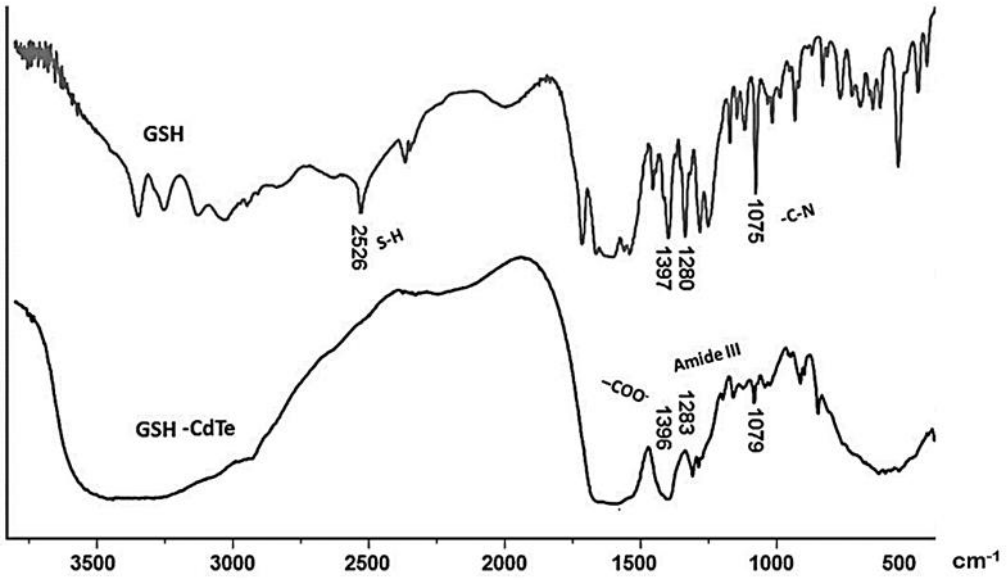

Figure 2. 9: An example of a FT-IR Spectrum image reprinted from J. Donoso and co-workers, Biomimetic, Mild Chemical Synthesis of CdTe-GSH Quantum Dots with Improved Biocompatibility, *PloS ONE* 2012, volume 7, issue 1, 1-9.

In the work done by Perez and co-workers, glutathione (GSH) capped cadmium telluride (CdTe) QDs were synthesized chemically, and FT-IR was used to characterize the QDs as seen in the FT-IR spectrum in Figure 2.9. Here, it can be seen that the capping agent glutathione and the capped quantum dots GSH-CdTe were both analysed via FT-IR independently. The results show that there is a disappearance of a thiol vibrational peak at around 2526 cm^{-1}, suggesting that the QDs were successfully 'capped' with GSH by forming a covalent bond between the thiol and the Cd atom at the surface of the CdTe quantum dot. The same principle is applied to this study, however, the only difference is the type of capping agent used, which is mercaptosuccinic acid.

2.6.2) Structural techniques

2.6.2.1) X –ray diffraction

X-ray diffraction (XRD), an extensively used technique for the characterization of nanoparticles provides information related to the crystalline structure, lattice parameters and nature of the phase of nanomaterials.[89] One of its main advantages are that experiments can

be performed on dried samples (of colloidal solutions) which results in volume averaged values.[89] In simpler terms XRD is based upon the constructive interference of X-rays and a crystalline sample.[90] The peaks which result from XRD are produced by constructive interference, of a beam of monochromatic X-rays scattered at specific angles from each lattice set present in a given sample. These peaks are characteristic to the sample of interest. The composition of material under study can be determined by making a comparison between the intensity of the peaks with that of the standard patterns available from the International Centre for Diffraction Data (ICDD) database.[89]

The working principle of XRD is based upon satisfying Bragg's law, only until Bragg's law is satisfied the incident beam of X-rays interacts constructively with that of the crystal structure, producing a diffracted ray.[90] Brags law is denoted in Equation 2.3 below:

$$n\lambda = 2dsin\Theta \qquad [2.3]$$

Braggs Law (where n is an integer, λ is the wavelength of the x-rays, d is the inter-planar spacing responsible for generating the diffraction, and Θ is the diffraction angle.

Brags Law relates the wavelength of incidence x-ray radiation to the diffraction angle and lattice spacing experienced in a sample of crystalline nature.[91] X-rays that are diffracted are collected by a detector and analysed. Crystalline samples can be identified by using XRD as each compound has a characteristic set of d-spacing's/inter-planar spacings and can be compared to standard reference patterns.[90] In a typical XRD system three main elements are always present, that is, an X-ray tube, a detector as well as the sample holder. X-rays are generated by the use of a cathode ray tube. In this tube a filament is heated to produce electrons, after which a voltage is applied in order to direct electrons to a target material. These electrons if given sufficient energy can dislodge inner shell electrons of the target material in order to produce X-rays.[90]

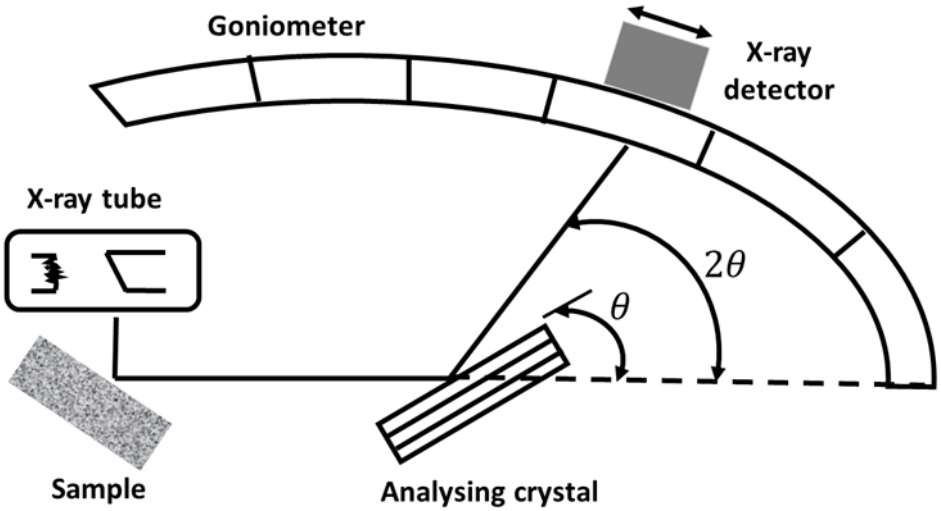

Figure 2. 10: Working principle of X-ray Diffraction instrument. X-ray tube/cathode tube (used as a source of electrons), sample (used to generate x-rays via interacting with electrons), analysing crystal (material of interest/under study) and the goniometer, is a tool used to measure angles accurately.[90] Image reprinted from A. Bunaciu and co-workers, X-ray Diffraction: Instrumentation and applications, Critical reviews in *analytical chemistry*, 2015, 45,289-299.

In the work done by Qiao and co-workers, zinc oxide (ZnO) QDs were synthesized and their agglomeration mechanisms were studied. XRD was used to characterize the ZnO QDs and it was reported from the XRD pattern that the QDs are indeed ZnO with a hexagonal wurzite crystal structure in accordance with the ICCD. Its diameter was approximated to be 4.8 nm by the use of Scherrer's formula.[92]

$$D_c = 0.89\,\lambda/Bcos(\Theta) \qquad [2.4]$$

Scherrer's Formula, where B is the half peak width, λ is the wavelength of incident X-rays and Θ is the diffraction angle.

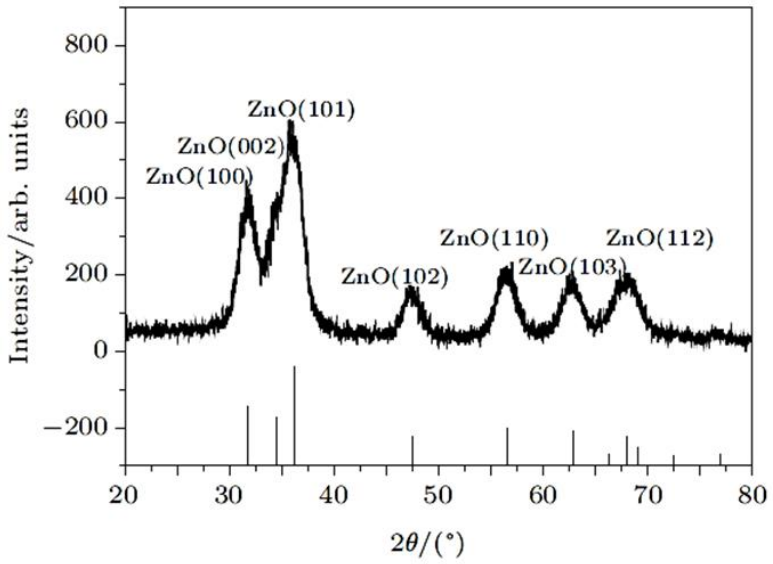

Figure 2. 11: Diffraction pattern obtained for ZnO QDs, image reprinted from B, Qiao and co-workers, Synthesis of ZnO quantum dots and their agglomeration mechanisms along with emission spectra based on ageing time and temperature, Chinese physical society and IOP publishing Ltd, 2016, vol.25, no.9.

2.6.2.2) Small Angle X-ray Scattering

Small angle X-ray scattering (SAXs) is a high resolution characterization technique that is able to express features in the 1-100 nm range. SAXs has the advantage of studying biological material in aqueous media, which makes it more stable and easier to analyse.[93] Applications of SAXs are broadly distributed across many fields, such as synthetic polymers, metal alloys, macromolecules, emulsions, and provides information about shape, size and distributions of various nanostructures.[94]

The working principle of SAXs is based upon an incident beam of monochromatic X-rays (typical wavelength range of 0.1 nm - 0.2 nm) which are allowed to make contact with a sample. Some of the X-rays scatter and some move through the sample, however, the X-rays that are scattered are detected by the use of a two-dimensional flat X-ray detector, which is situated behind the sample. Only the X-rays recorded at low angles (typically 0.1 degrees - 10 degrees) are used to form a scattering pattern which is then detected by the detector. The

scattering pattern contains important information about the sample such as its size, shape and surface to volume ratio of particles.[95]

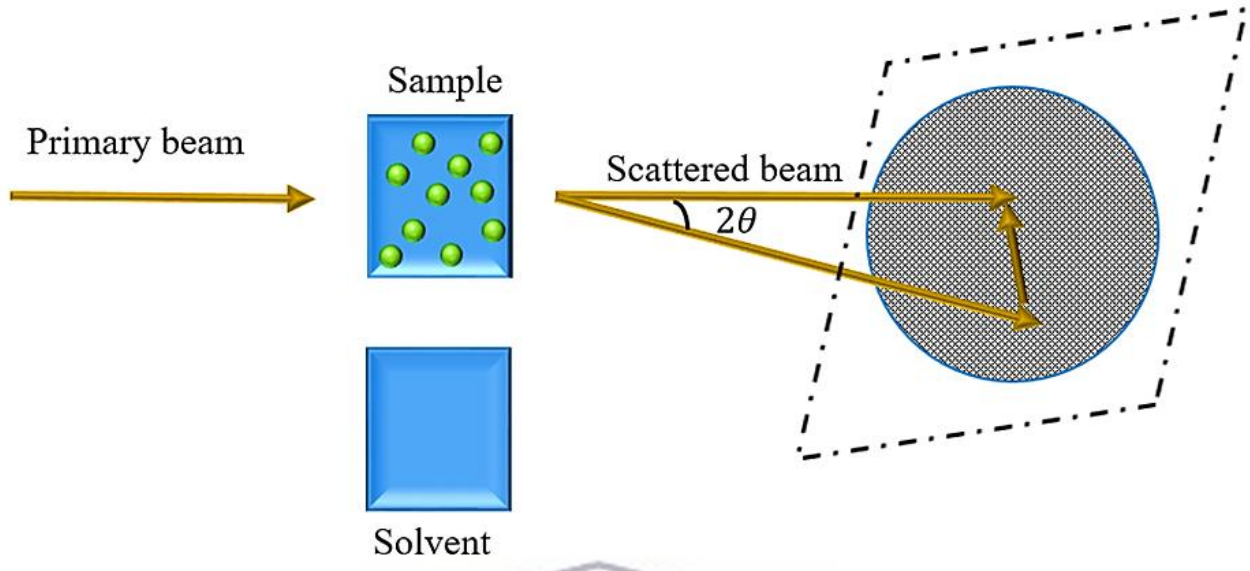

Figure 2.12: Schematic representation of a SAXs experiment, image reprinted from D. Svergun and co-workers, Small-angle scattering studies of biological macromolecules in solution, 2003, *IOp* publishing ltd, 1 – 12.

SAXs is a great alternative for sizing nanocrystals; and it has some advantages over transmission electron microscopy (TEM) for the characterization of nanocrystals;[96]

- Experiments in SAXs are performed in solution, this gets rid of destructive drying techniques or even the possibility of agglomeration induced by evaporation steps
- A larger amount of particles are studied during a SAXs experiment, in comparison to that of TEM, it differs by 7 orders of magnitude
- Data obtained from SAXs experiments is not as dependent on the operator, in comparison to that of TEM.

In the work done by Dabbousi and co-workers, SAXs was used to analyse the particle size distribution of highly luminescent (CdSe)ZnS composite QDs. The source of x-rays was a copper anode, and the x-ray beam was then collimated onto a position sensitive detector. The size of the QDs in a polymer matrix was calculated to exist in a range of 47 angstrom - 50 angstrom.[97]

2.6.3) Microscopic Techniques

2.6.3.1) High Resolution Scanning Electron Microscopy

High Resolution Scanning Electron Microscopy (HR-SEM) is a characterization technique that offers various information about the surface phenomena of materials.[98] Information such as the topography, morphology, crystallographic information as well as composition of material can be obtained. Here detailed images of particles are a result with a spatial resolution of 1 nm, which is not possible using a conventional optical microscope.[98]

It works in the following way; a beam of electrons are produced by an electron gun situated above the sample,[99] these electrons are then accelerated by applying heat or a voltage. Electrons are then allowed to travel in a vacuum towards the sample as to minimize the risk of obstruction of the electrons (so energy is not lost). Electrons are then allowed to scan over the sample in a raster fashion. These electrons also known as primary electrons can now provide energy to electrons in the sample and allow it to release electrons known as secondary electrons, or x-rays.[99] These secondary electrons as well as x-rays can be collected by a detector which picks up rebounding electrons. Once this information is analysed a three dimensional image can be generated for the sample under analysis.[98] Figure 2.13 below shows the interaction of an electron beam with the sample of interest and the resultant electrons or x-rays which are emitted.

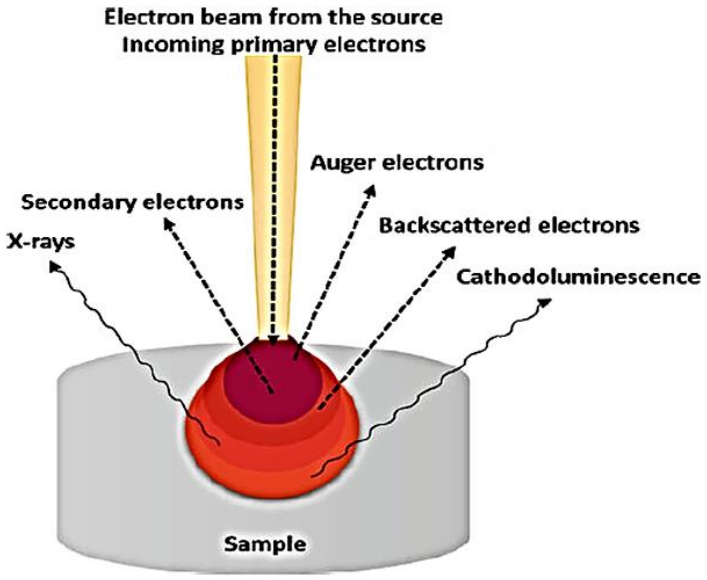

Figure 2. 13: Electron beam interacting with a sample in a SEM set-up, where secondary electrons refer to electrons emitted by the sample that gained enough energy to leave when hit. Image reprinted from K. Akhtar and co-workers, Scanning Electron Microscopy: Princicple and Applications in Nanomaterials Characterization, *Springer international publishing*, 2018, 113 – 145.

Sample preparation for SEM is usually dependent on whether the specimen is a metal or a non-metal, metals require very little preparation as they respond in a favourable manner to electrons, however, non-metal samples has to be modified before analysis by coating with conductive material.[99] In the work done by (Kapatkar et al, 2009) SEM was used to confirm the size and shape of high quality CdSe quantum dots synthesised via an aqueous route by making use of thioglycholic acid as a capping agent. Here, the QDs were prepared at room temperature, and SEM was used to confirm a particle size reported to be 2 nm - 3 nm in diameter. Also from the SEM images, clear lattice fringes present indicated good crystallinity of the sample. The QDs were also found to be monodispersed and spherical without any agglomeration. This could be due to the correct amount of capping agent used to prevent QDs from 'sticking together'.[100]

2.6.3.2) High Resolution Transmission Electron Microscopy

High resolution transmission electron microscopy (HR-TEM) is an imaging technique that is used to characterize the size and shape of nanomaterials directly.[101] The Transmission electron microscope has a similar structure to a normal optical microscope, however, differs by replacing the light bulb in optical microscopes with an electron gun, and glass lenses are replaced by magnetic lenses in transmission electron microscopy.[102] Other features which make this type of microscopy unique is the use of three different lenses which work together to form an image, these lenses are known as the objective, intermediate and projection lenses. In transmission electron microscopy electrons are concentrated into the central axis of the microscope column by the use of a vacuum as a medium for the electrons to travel, the electrons are then passed through the sample and converged by a series of lenses, until which a final image is generated on a phosphor screen.[102] The working principle of a transmission electron microscope is shown in Figure 2.14 below.

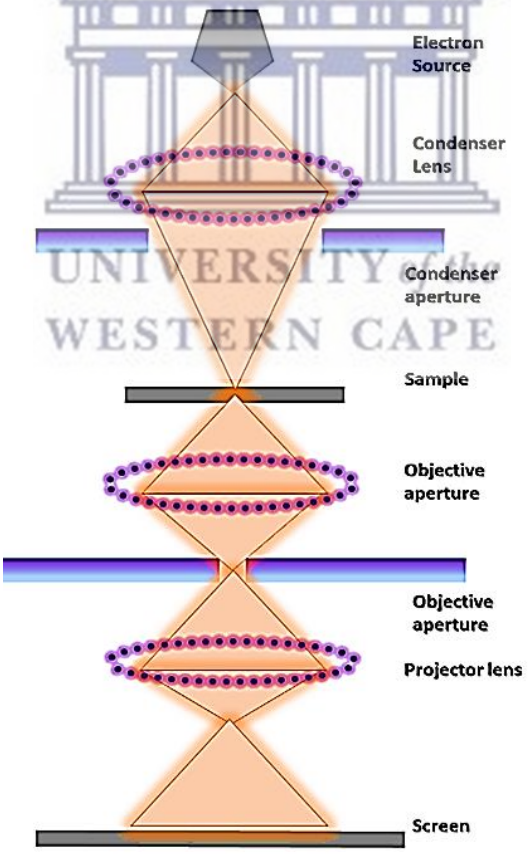

Figure 2. 14: Showing the working principles of HR-TEM.

In the work done by Chen and co-workers, HR-TEM was used to characterize their GSH-CdTe quantum dots synthesized via a one-pot synthesis method. A diameter of 6 nm and a spherical shape, with a well dispersed crystalline structure was reported for their quantum dots.[103]

2.6.4) Electrochemical techniques

2.6.4.1) Electrochemical Impedance

Impedance first made an introduction into electrical engineering by Oliver Heaviside in the early 1880's,[28] who adapted complex numbers to study electrical circuits.[29] Electrochemical impedance spectroscopy (EIS), is an electrochemical characterization technique that operates in the frequency domain and can be measured by applying an AC potential to an electrochemical cell and measuring the resulting current.[29] The applied sinusoidal excitation potential E_t can be expressed by:

$$Et = E_0 \,.Sin(\omega t) \qquad [2.5]$$

Applied sinusoidal excitation potential in impedance is represented by the above equation, where E_t is the potential at time t, E_0 is the amplitude of the signal and $\omega = 2\pi f$ is the radial frequency, fis the frequency expressed in hertz (Hz).[29] The response to the AC potential is an AC current signal, which can be represented by Equation 2.6 below:

$$I_t = I_0 Sin(\omega t + \emptyset) \qquad [2.6]$$

The resulting current after an AC potential was applied can be represented by the formula above, where I_t represents the intensity of the resulting current, I_o being the amplitude and a phase angle $\emptyset$.[29]

If we relate Equation 2.5 and 2.6 above to ohms law the impedance of the electrochemical system can then be represented by equation 2.7 below:

$$Z = \frac{E_t}{I_t} = \frac{E_0 Sin(\omega t)}{I_0 Sin(\omega t + \emptyset)} = Z_0 \frac{Sin(\omega t)}{Sin\ (\omega t + \emptyset)} \quad [2.7]$$

Impendence of an electrochemical cell by its relation to ohms law. [29]

From the above equation it can be seen that impedance can be treated as a vector quantity with a magnitude represented by $Z_0$and a direction given by $\emptyset$.[29]

In order to mathematically treat impedance data, the real and imaginary axis are often depicted, the real part is accounted for by the resistance as it doesn't produce a phase shift, whereas the imaginary part is accounted for the by capacitor/double capacitance layer as it does produce a phase shift.[29] Graphical representations of impedance data is usually represented by the 'Nyquist plot' which plots the imaginary (Z_i) versus the real part (Z_r) of the impedance. A graphical representation is shown in Figure 2.15 below, each point represented here corresponds to its own unique frequency value.[29]

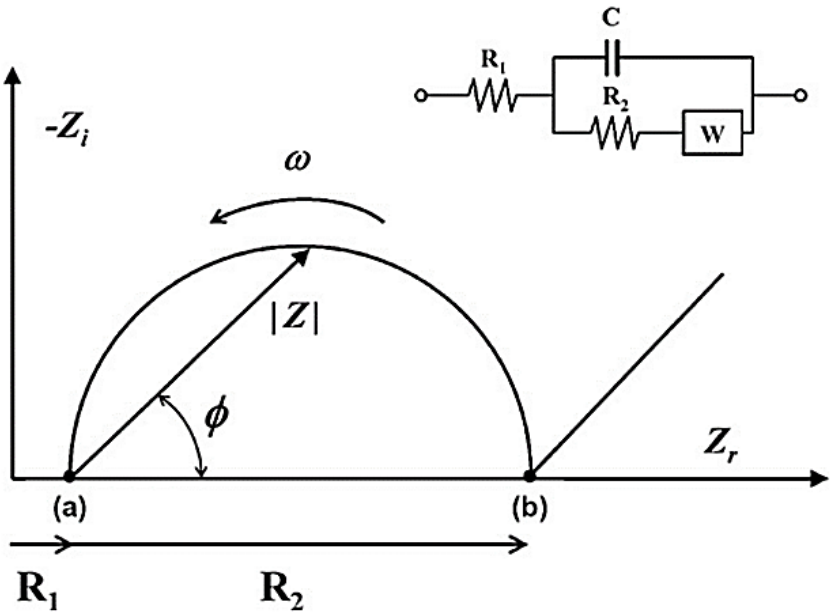

Figure 2. 15: Example of a Nyquist plot and its equivalent Randles circuit. Image reprinted from A. Bonanni and M. Del Valle, Use of nanomaterials for impedimetric DNA biosensors: A Review, *Elsevier*, 2010, 7 – 17.

Electrochemical impedance is an electrochemical technique which is simple to operate, sensitive in its detection and non-destructive to biological material or samples, and has been a popular area of research in terms of biosensor fabrication.[30]

In the work done by (Wang et al, 2019) an electrochemical aptasensor for the sensitive detection of malachite green was reported. This sensor was equipped with a nanocomposite material which consisted of gold nanoparticles (Au-NPs), graphene quantum dots as well as tungsten disulphide nanosheets. Malachite green is a dye which has been very popular in the agricultural community but studies have shown that it does have carcinogenic effects amongst others.[104] The electrochemical performance of the sensor was studied using EIS. Nyquist plots for each step in sensor fabrication was studied using a ferricyanide probe, as shown in Figure 2.16, the linear portion of the graph corresponds to diffusion limited processes and the diameter of the respective semi-circles corresponds to the charge transfer resistance (R_{ct}).[104]

In Figure 2.16 below different fabrication steps were reported for the fabrication of the aptasensor. The first step denoted by ‘curve a’, represents the bare glassy carbon electrode platform. While ‘curve b’ refers to the second fabrication stage, where the nanomaterial was

implemented as an electron mediator onto the sensing platform. It can be seen that when 'curve b' is compared to 'curve a' there is a decrease in the R_{ct} value, this means that the nanomaterial were more conductive than the bare electrode. However, 'curve c' refers to aptamer immobilization onto the electrode surface. The aptamer is the sensing component of this sensor and is specific to the analyte being detected namely 'malachite green' and a clear increase in the R_{ct} was observed implying successful immobilization of the aptamer onto the surface (this increase is due to the repulsion between the negatively charged redox probe and the aptamer).[104] The second last step is denoted by 'curve d', here, mercaptohexanoic acid was used as a blocking agent to block non-specific binding sites (R_{ct} decreased as MCH hindered electron transfer).[104]

In this study EIS will be implemented to study the electrode fabrication steps as well as to characterize the QDs produced.

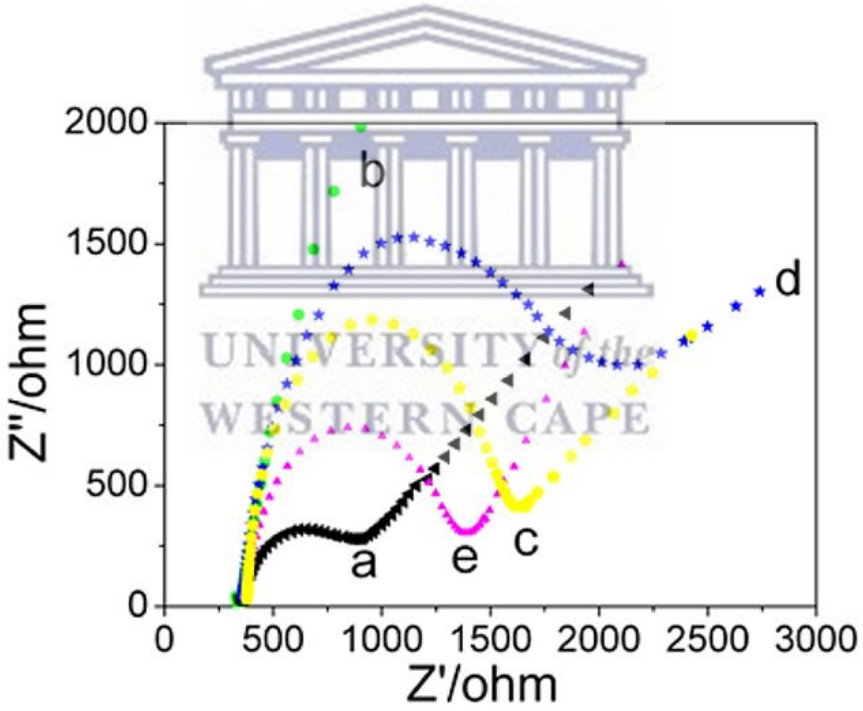

Figure 2. 16: EIS spectra of different fabrication steps in aptasensor design, (a) bare GCE, (b) GCE/GQDs-WS_2/Au-NPs, (c) GCE/GQDs-WS_2/Au-NPs/aptamer, (d) GCE/GQDs-WS_2/Au-NPs/aptamer/MCH and (e) GCE/GQDs-WS_2/Au-NPs/aptamer/MCH in the presence of malachite green. Image reprinted from Q. Wang and co-workers, Label-free Electrochemical Aptasensor for Sensitive Detection of Malachite Green Based on Au Nanoparticle/Graphene Quantum Dots/Tungsten Disulfide Nanocomposites, *Nanomaterials* 2019, 1 – 14.

2.6.4.2) Cyclic Voltammetry

Cyclic voltammetry (CV) is a powerful technique used to study the reduction and oxidation processes of molecular species.[105] It also gives qualitative information about the stability of the REDOX processes and electron transfer kinetics.[106] This technique is based upon cycling a potential at a particular scan rate and measuring the resulting current.[107] Unlike Linear sweep voltammetry (LSV), CV reverses potential directions from either a negative to a positive scan or vice versa. Once the scan reaches the set potential, the potential is then reversed and return to the initial potential that was applied to the working electrode. Cyclic voltammetry can be used to find out if a system is reversible, quasi reversible or irreversible, assuming a reversible reaction we can analyse the cyclic voltammogram shown in Figure 2.17 below by the following set of Equations.

Assuming an electroactive species R gets oxidized into species O when potential is ramped positively;

$$R \leftrightarrow O + ne^{-1} \quad [2.8]$$

Electrochemical oxidation of species R

Once potential is reversed and scanned negatively, the following occurs;

$$O + ne^{-1} \leftrightarrow R \quad [2.9]$$

Electrochemical Reduction of species O

If we were to run a cyclic voltammetry experiment on the species shown above, the following cyclic voltammogram as shown in Figure 2.17 below would be obtained.

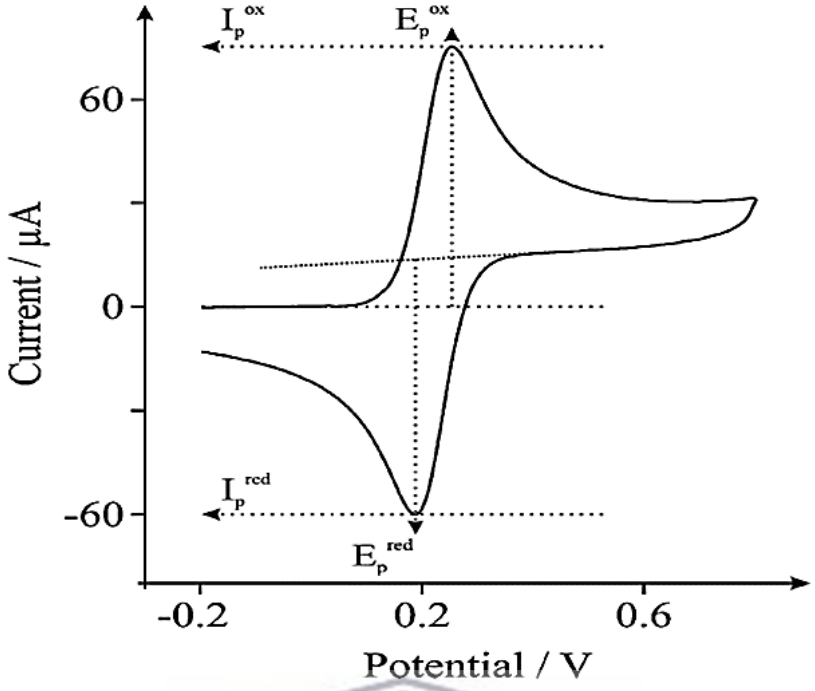

Figure 2. 17: A simple voltammogram, image reprinted from D. Brownson and co-workers, Graphene electrochemistry: Fundamental concepts through to prominent applications, *Royal society of chemistry*, 2012, 6994 – 6977.

Where:

- E_P^{red} Cathodic peak potential
- E_p^{ox} Anodic peak potential
- i_p^{red} Cathodic peak current
- i_p^{ox} Anodic peak current

For a reversible process the ratio between the peak currents should equate to one;

Where, $\frac{i_{p,c}}{i_{p,a}} = 1^{10s1}$ [2.10]

When the redox process is reversible the peak current is given by the equation

$i_p = 0.4463nFDA(Da)^{\frac{1}{2}}C^b$ [2.11]

Peak current for fixed parameters:

Where, $a = \frac{nFV}{RT} = \frac{nV}{0.026}\ at\ 25^0C$ [2.12]

Here: i_p is the peak current, n is the number of electrons, F is faradays constant (c/mol), a is the geometric area of the electrode, R is the ideal gas constant, T is the absolute temperature, V is the scan rate in V/s and D is the diffusion coefficient in cm^2/s

In the work done by Senet and co-workers, an electrochemical DNA biosensor was reported for breast cancer gene BRAC1 detection. The sensor was designed by implementing three different dendrimer ferrocene-cored poly(amidoamine) generations, this was then chemically adsorbed onto a gold electrode surface (AuE) and single stranded DNA was immobilized onto the electrode to detect BRAC1 gene. Figure 2.18 below shows sensor fabrication steps which were studied for first generation dendrimer immobilization.

In the cyclic voltammogram represented by Figure 2.18, it can be seen that no reversible peaks were shown for the bare AuE, however, once the ferrocene-cored poly(amidoamine) first generation dendrimers were immobilized onto the electrode surface a pair of well-defined redox peaks were observed, indicating a good electron mediator characteristic.[36] Further modification steps such as the binding of single stranded DNA which was done using glutaraldehyde as a linking agent between the dendrimer and DNA, the cyclic voltammogram shows a decrease in peak currents, which could be due to repulsion between the negative DNA backbone and the electrolyte solution.[36]

In this study CV was also used to study the different steps in the aptasensor fabrication process.

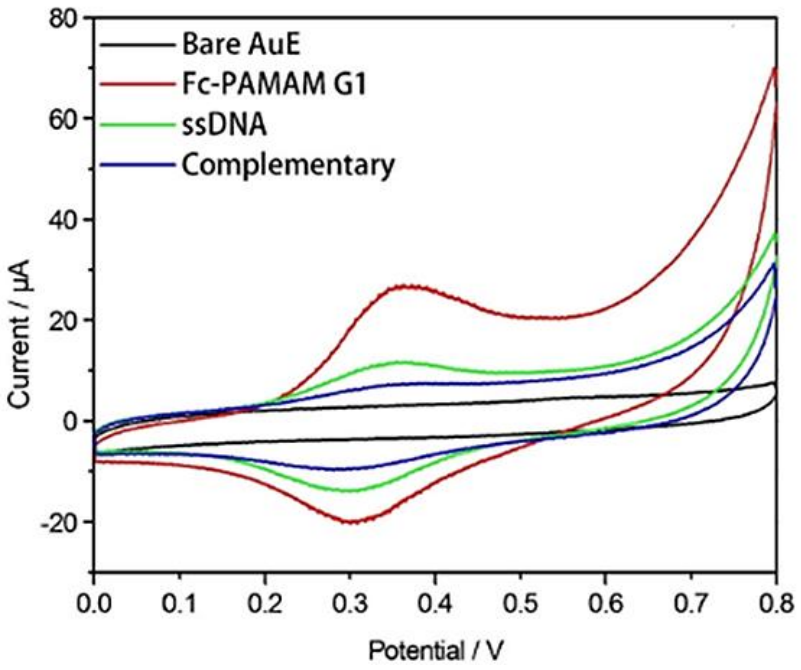

Figure 2. 18: Fabrication steps of an electrochemical aptasensor (in 10 mM PBS, pH 7.4). Image reprinted form M. Senet and co-workers, Electrochemcial DNA biosensors for label free breast cancer gene marker detection, *Analytical and Bioanalytical Chemistry*, 2019, 2925 -2935.

2.6.5.3) Differential Pulse voltammetry

Differential pulse voltammetry (DPV) is a sensitive electrochemical technique which relies on discrimination of faradaic currents.[22] In DPV the potential applied is different in comparison to methods like CV. In CV potential is applied directly to the system and is reversed at a certain point to return to its original starting potential. DPV, however, implements a potential which consists of small pulses which are often superimposed on a stair case waveform.[22,108] Here, the resulting current is measured at two points, before the pulse is applied and one taken after the pulse has been applied. The current measured before the pulse is subtracted from the current measured after, and this difference is then plotted verses the potential applied to the system.[108] The highest peak current obtained is proportional to the concentration of analyte present in the system and this can be depicted by equation 2.13 below.[108]

$$i_p = \frac{nFAD^{1/2}C}{\sqrt{\pi t_m}}\left(\frac{1-\alpha}{1+\alpha}\right) \quad [2.13]$$

Where, $\alpha = exp\left[\left(\frac{nF}{RT}\right)\left(\frac{\Delta E}{2}\right)\right]$ and AE is pulse amplitude, i_p= peak current, n= number of electrons involved in the redox reaction system, A= area of electrode, D= diffusion coefficient, F=faradays constant, T=ambient temperature and R = ideal gas constant.

In the work done by Yao and co-workers, a single use biosensor for the detection of prostate cancer biomarker AMACR was reported. AMACR antigen was prepared in 0.1 M PBS solution with concentrations ranging from 10 µg/mL to 0.05 µg/mL. DPV was used to study the biosensor response. Figure 2.19 shows DPV measurements of the AMACR antigen in 0.1 M PBS. A LOD of 0.05 µg/mL for the detection of AMACR was reported using DPV as detection method.

In this study DPV will also be used as a method of detection for emerging prostate cancer AMACR using an aptasensor equipped with MSA-WTe_3 QDs.

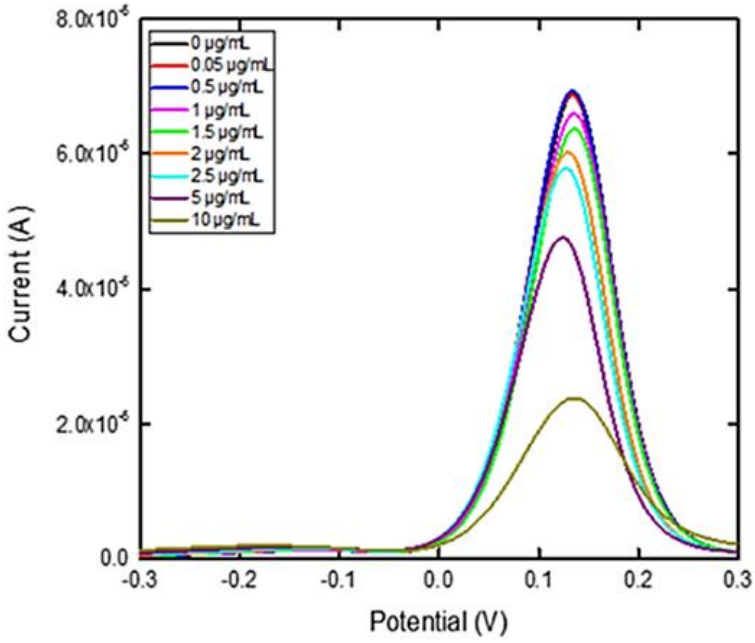

Figure 2. 19: DPV measurements of AMACR antigen in 0.1 M PBS. Image reprinted from J. Yao and co-workers, Bio-conjugated, single-use Biosensor for the Detection of Biomarkers of Prostate Cancer, *American Chemical society Omega*, 2018, 3, 6411-6418.

Conclusion

This chapter gave insight to the different types of electrochemical biosensors and how they replace heavy desktop machinery for applications in disease diagnostics, different transduction methods as well as different bio-receptors were made mention of in order to classify different types of biosensor and their respective classes. In this study an electrochemical aptasensor was reported for AMACR detection equipped with MSA-WTe_3 QDs for prostate cancer disease diagnosis applications. Topics such as biomarkers, and aptamers as well as quantum dots were all introduced and made reference to in order to aid the understanding of the work done in this study. Different methods for characterization of QDs produced in this study were mentioned and explained, as well as the information that these techniques would be expected to provide. Methods of biomarker detection are also introduced in order to execute a good understanding of each method of detection and how it applies to this study.

References

1 F. Mustafa and S. Andreescu, Chemical and biological sensors for food-quality monitoring and smart packaging, *Foods*, , DOI:10.3390/foods7100168.

2 B. L. Saul and M. Sc, Types of Sensors for Environmental Monitoring, 2018, 2–5.

3 A. Lewis and P. Edwards, Validate personal air-pollution sensors, *Nature*, 2016, **535**, 29–31.

4 C. G. Niu, A. L. Guan, G. M. Zeng, Y. G. Liu and Z. W. Li, Fluorescence water sensor based on covalent immobilization of chalcone derivative, *Anal. Chim. Acta*, 2006, **577**, 264–270.

5 J. W. Hummel, K. A. Sudduth and S. E. Hollinger, Soil moisture and organic matter prediction of surface and subsurface soils using an NIR soil sensor, *Comput. Electron. Agric.*, 2001, **32**, 149–165.

6 Y. Liu, K. Ai, X. Cheng, L. Huo and L. Lu, Gold-nanocluster-based fluorescent sensors for highly sensitive and selective detection of cyanide in water, *Adv. Funct. Mater.*, 2010, **20**, 951–956.

7 J. Fu, B. Park, G. Siragusa, L. Jones, R. Tripp, Y. Zhao and Y. J. Cho, An Au/Si hetero-nanorod-based biosensor for Salmonella detection, *Nanotechnology*, , DOI:10.1088/0957-4484/19/15/155502.

8 N. Olson and J. Bae, Biosensors—publication trends and knowledge domain visualization, *Sensors (Switzerland)*, , DOI:10.3390/s19112615.

9 N. Bhalla, P. Jolly, N. Formisano and P. Estrela, Introduction to biosensors, *Essays Biochem.*, 2016, **60**, 1–8.

10 B. Jurado-Sánchez, Nanoscale biosensors based on self-propelled objects, *Biosensors*, 2018, **8**, 1–15.

11 P. Mehrotra, Biosensors and their applications - A review, *J. Oral Biol. Craniofacial Res.*, 2016, **6**, 153–159.

12 P. Damborský, J. Švitel and J. Katrlík, Optical biosensors, *Essays Biochem.*, 2016, **60**, 91–100.

13 K. Ramanathan and B. Danielsson, Principles and applications of thermal biosensors, *Biosens. Bioelectron.*, 2001, **16**, 417–423.

14 M. Pohanka, Overview of piezoelectric biosensors, immunosensors and DNA sensors and their applications, *Materials (Basel).*, , DOI:10.3390/ma11030448.

15 K. Dziąbowska, E. Czaczyk and D. Nidzworski, Application of Electrochemical Methods in Biosensing Technologies, *Biosensing Technol. Detect. Pathog. - A Prospect. W. Rapid Anal.*, , DOI:10.5772/intechopen.72175.

16 R. Raccichini, M. Amores and G. Hinds, Critical review of the use of reference electrodes in li-ion batteries: A diagnostic perspective, *Batteries*, 2019, **5**, 1–24.

17 M. S. Cosio, M. Scampicchio and S. Benedetti, Electronic Noses and Tongues, *Chem. Anal. Food Tech. Appl.*, 2012, 219–247.

18 Y. Wang, Z. Zhang, V. Jain, J. Yi, S. Mueller, J. Sokolov, Z. Liu, K. Levon, B. Rigas and M. H. Rafailovich, Potentiometric sensors based on surface molecular imprinting: Detection of cancer biomarkers and viruses, *Sensors Actuators, B Chem.*, 2010, **146**, 381–387.

19 S. Roy and S. Pandit, *Microbial Electrochemical System*, Elsevier B.V., 2019.

20 K. Mahato, S. Kumar, A. Srivastava, P. K. Maurya, R. Singh and P. Chandra, *Electrochemical Immunosensors: Fundamentals and Applications in Clinical Diagnostics*, Elsevier Inc., 2018.

21 C.J. Theresa, Square Wave Voltammetric Determination of Various Pharamaceuticals, Department of applied chemistry, Thesis, COCHIN UNIVERSITY OF SCIENCE AND TECHNOLOGY, 2015.

22 K. Scott, *Electrochemical Principles and Characterization of Bioelectrochemical Systems*, Elsevier Ltd., 2015.

23 A. H. Alghamdi, Applications of stripping voltammetric techniques in food analysis,

Arab. J. Chem., 2010, **3**, 1–7.

24 S. Zhang, P. Du and F. Li, Detection of prostate specific antigen with 3,4-diaminobenzoic acid (DBA)-H2O2-HRP voltammetric enzyme-linked immunoassay system, *Talanta*, 2007, **72**, 1487–1493.

25 N. R. Stradiotto, H. Yamanaka and M. V. B. Zanoni, Electrochemical sensors: A powerful tool in analytical chemistry, *J. Braz. Chem. Soc.*, 2003, **14**, 159–173.

26 N. Jaffrezic-Renault and S. V. Dzyadevych, Conductometric microbiosensors for environmental monitoring, *Sensors*, 2008, **8**, 2569–2588.

27 A. A. Adams, P. I. Okagbare, J. Feng, M. L. Hupert, D. Patterson, J. Götten, R. L. McCarley, D. Nikitopoulos, M. C. Murphy and S. A. Soper, Highly efficient circulating tumor cell isolation from whole blood and label-free enumeration using polymer-based microfluidics with an integrated conductivity sensor, *J. Am. Chem. Soc.*, 2008, **130**, 8633–8641.

28 U. of N. C. J. Ross Macdonald (Department of Physics and Astronomy, Impedance Spectroscopy, *Ann. Biomed. Eng.*, 1992, **20**, 289–305.

29 A. Bonanni and M. Del Valle, Use of nanomaterials for impedimetric DNA sensors: A review, *Anal. Chim. Acta*, 2010, **678**, 7–17.

30 L. Fan, G. Zhao, H. Shi, M. Liu and Z. Li, A highly selective electrochemical impedance spectroscopy-based aptasensor for sensitive detection of acetamiprid, *Biosens. Bioelectron.*, 2013, **43**, 12–18.

31 X. Liu, Y. Qin, C. Deng, J. Xiang and Y. Li, A simple and sensitive impedimetric aptasensor for the detection of tumor markers based on gold nanoparticles signal amplification, *Talanta*, 2015, **132**, 150–154.

32 P. B. Luppa, L. J. Sokoll and D. W. Chan, Immunosensors - Principles and applications to clinical chemistry, *Clin. Chim. Acta*, 2001, **314**, 1–26.

33 T. Zhang, B. Xing, Q. Han, Y. Lei, D. Wu, X. Ren and Q. Wei, Electrochemical immunosensor for ochratoxin A detection based on Au octahedron plasmonic

colloidosomes, *Anal. Chim. Acta*, 2018, **1032**, 114–121.

34 A. C. Honorato Castro, E. G. França, L. F. De Paula, M. M. C. N. Soares, L. R. Goulart, J. M. Madurro and A. G. Brito-Madurro, Preparation of genosensor for detection of specific DNA sequence of the hepatitis B virus, *Appl. Surf. Sci.*, 2014, **314**, 273–279.

35 S. F. Douman, The Response Dynamics of Indium Telluride Quantum Dots Impedimetric Genosensor for Telomerase Cancer Biomarker, Thesis, University of the Western Cape, 2013.

36 M. Senel, M. Dervisevic and F. Kokkokoğlu, Electrochemical DNA biosensors for label-free breast cancer gene marker detection, *Anal. Bioanal. Chem.*, 2019, **411**, 2925–2935.

37 P. F. Rostamabadi and E. Heydari-Bafrooei, Impedimetric aptasensing of the breast cancer biomarker HER2 using a glassy carbon electrode modified with gold nanoparticles in a composite consisting of electrochemically reduced graphene oxide and single-walled carbon nanotubes, *Microchim. Acta*, , DOI:10.1007/s00604-019-3619-y.

38 S. Wu, N. Duan, Z. Shi, C. Fang and Z. Wang, Simultaneous aptasensor for multiplex pathogenic bacteria detection based on multicolor upconversion nanoparticles labels, *Anal. Chem.*, 2014, **86**, 3100–3107.

39 G. K. Mishra, V. Sharma and R. K. Mishra, Electrochemical aptasensors for food and environmental safeguarding: A review, *Biosensors*, 2018, **8**, 1–13.

40 M. Yousefi, S. Dehghani, R. Nosrati, H. Zare, M. Evazalipour, J. Mosafer, B. S. Tehrani, A. Pasdar, A. Mokhtarzadeh and M. Ramezani, Aptasensors as a new sensing technology developed for the detection of MUC1 mucin: A review, *Biosens. Bioelectron.*, 2019, **130**, 1–19.

41 T. Sampson, Aptamers and SELEX: The technology, *World Pat. Inf.*, 2003, **25**, 123–129.

42 R. Stoltenburg, C. Reinemann and B. Strehlitz, SELEX-A (r)evolutionary method to

generate high-affinity nucleic acid ligands, *Biomol. Eng.*, 2007, **24**, 381–403.

43 Y. X. Wu and Y. J. Kwon, Aptamers: The "evolution" of SELEX, *Methods*, 2016, **106**, 21–28.

44 L. Zhao, Y. Huang, Y. Dong, X. Han, S. Wang and X. Liang, Aptamers and Aptasensors for Highly Specific Recognition and Sensitive Detection of Marine Biotoxins: Recent Advances and Perspectives, *Toxins (Basel).*, , DOI:10.3390/toxins10110427.

45 S. G. Meirinho, L. G. Dias, A. M. Peres and L. R. Rodrigues, Voltammetric aptasensors for protein disease biomarkers detection: A review, *Biotechnol. Adv.*, 2016, **34**, 941–953.

46 S. Balamurugan, A. Obubuafo, S. A. Soper and D. A. Spivak, Surface immobilization methods for aptamer diagnostic applications, *Anal. Bioanal. Chem.*, 2008, **390**, 1009–1021.

47 L. Zhou, M. H. Wang, J. P. Wang and Z. Z. Ye, Application of biosensor surface immobilization methods for aptamer, *Fenxi Huaxue/ Chinese J. Anal. Chem.*, 2011, **39**, 432–438.

48 A. Erdem, H. Karadeniz, G. Mayer, M. Famulok and A. Caliskana, Electrochemical sensing of aptamer-protein interactions using a magnetic particle assay and single-use sensor technology, *Electroanalysis*, 2009, **21**, 1278–1284.

49 I. Palchetti and M. Mascini, Electrochemical nanomaterial-based nucleic acid aptasensors, *Anal. Bioanal. Chem.*, 2012, **402**, 3103–3114.

50 M. Vidotti, R. F. Carvalhal, R. K. Mendes, D. C. M. Ferreira and L. T. Kubota, Biosensors based on gold nanostructures, *J. Braz. Chem. Soc.*, 2011, **22**, 3–20.

51 L. S. S. Kumar, X. Wang, J. Hagen, R. Naik, I. Papautsky and J. Heikenfeld, Label free nano-aptasensor for interleukin-6 in protein-dilute bio fluids such as sweat, *Anal. Methods*, 2016, **8**, 3440–3444.

52 M. Srivastava, N. R. Nirala, S. K. Srivastava and R. Prakash, A comparative Study of

Aptasensor Vs Immunosensor for Label-Free PSA Cancer Detection on GQDs-AuNRs Modified Screen-Printed Electrodes, *Sci. Rep.*, 2018, **8**, 1–11.

53 Y. Li, M. Han, H. Bai, Y. Wu, Z. Dai and J. Bao, A sensitive electrochemical aptasensor based on water soluble CdSe quantum dots (QDs) for thrombin determination, *Electrochim. Acta*, 2011, **56**, 7058–7063.

54 M. Adeel, M. M. Rahman and J. J. Lee, Label-free aptasensor for the detection of cardiac biomarker myoglobin based on gold nanoparticles decorated boron nitride nanosheets, *Biosens. Bioelectron.*, 2019, **126**, 143–150.

55 Z. S. Qian, X. Y. Shan, L. J. Chai, J. R. Chen and H. Feng, A fluorescent nanosensor based on graphene quantum dots-aptamer probe and graphene oxide platform for detection of lead (II) ion, *Biosens. Bioelectron.*, 2015, **68**, 225–231.

56 F. S. Sabet, M. Hosseini, H. Khabbaz, M. Dadmehr and M. R. Ganjali, FRET-based aptamer biosensor for selective and sensitive detection of aflatoxin B1 in peanut and rice, *Food Chem.*, 2017, **220**, 527–532.

57 I. Grabowska, N. Sharma, A. Vasilescu, M. Iancu, G. Badea, R. Boukherroub, S. Ogale and S. Szunerits, Electrochemical Aptamer-Based Biosensors for the Detection of Cardiac Biomarkers, *ACS Omega*, 2018, **3**, 12010–12018.

58 O. A. Alsager, S. Kumar, B. Zhu, J. Travas-Sejdic, K. P. McNatty and J. M. Hodgkiss, Ultrasensitive colorimetric detection of 17-estradiol: The effect of shortening dna aptamer sequences, *Anal. Chem.*, 2015, **87**, 4201–4209.

59 S. Ornes, Core Concept: Quantum dots, *Proc. Natl. Acad. Sci.*, 2016, **113**, 2796–2797.

60 Y. Li and C. W. Peng, Application of quantum dots-based biotechnology in cancer diagnosis: Current status and future perspectives, *J. Nanomater.*, , DOI:10.1155/2010/676839.

61 S. J. Rosenthal, J. C. Chang, O. Kovtun, J. R. McBride and I. D. Tomlinson, Biocompatible quantum dots for biological applications, *Chem. Biol.*, 2011, **18**, 10–24.

62 M. Green, Semiconductor quantum dots as biological imaging agents, *Angew. Chemie*

- *Int. Ed.*, 2004, **43**, 4129–4131.

63 I. Mora-Seró, S. Giménez, T. Moehl, F. Fabregat-Santiago, T. Lana-Villareal, R. Gómez and J. Bisquert, Factors determining the photovoltaic performance of a CdSe quantum dot sensitized solar cell: The role of the linker molecule and of the counter electrode, *Nanotechnology*, , DOI:10.1088/0957-4484/19/42/424007.

64 R. D. Singh, R. Shandilya, A. Bhargava, R. Kumar, R. Tiwari, K. Chaudhury, R. K. Srivastava, I. Y. Goryacheva and P. K. Mishra, Quantum Dot Based Nano-Biosensors for Detection of Circulating Cell Free miRNAs in Lung Carcinogenesis: From Biology to Clinical Translation, *Front. Genet.*, 2018, **9**, 1–23.

65 A. E. M. Aly and A. Nasr, Theoretical study of one-intermediate band quantum dot solar cell, *Int. J. Photoenergy*, , DOI:10.1155/2014/904104.

66 R. S. Pawar, P. G. Upadhaya and V. B. Patravale, *Quantum Dots : Novel Realm in Biomedical and Pharmaceutical Industry*, Elsevier Inc., 2018.

67 O. D. Neikov and N. A. Yefimov, *Nanopowders*, Elsevier Ltd., 2nd edn., 2019.

68 A. R. AbouElhamd, K. A. Al-Sallal and A. Hassan, Review of core/shell quantum dots technology integrated into building's glazing, *Energies*, , DOI:10.3390/en12061058.

69 R. E. Bailey and S. Nie, Alloyed semiconductor quantum dots: Tuning the optical properties without changing the particle size, *J. Am. Chem. Soc.*, 2003, **125**, 7100–7106.

70 Z. Niu and Y. Li, Removal and utilization of capping agents in nanocatalysis, *Chem. Mater.*, 2014, **26**, 72–83.

71 A. Valizadeh, A. Valizadeh, H. Mikaeili, H. Mikaeili, M. Samiei, M. Samiei, S. M. Farkhani, S. M. Farkhani, N. Zarghami, N. Zarghami, M. Kouhi, M. Kouhi, A. Akbarzadeh, A. Akbarzadeh, S. Davaran and S. Davaran, Quantum dots: synthesis, bioapplications, and toxicity., *Nanoscale Res. Lett.*, 2012, **7**, 480.

72 A. Banerjee, T. Pons, N. Lequeux, B. Dubertret, P. Marie and B. Dubertret, Quantum dots – DNA bioconjugates : synthesis to applications.

73 K. Strimbu and J. A. Tavel, What are biomarkers?, *Curr. Opin. HIV AIDS*, 2010, **5**, 463–466.

74 L. M. Babrak, J. Menetski, M. Rebhan, G. Nisato, M. Zinggeler, N. Brasier, K. Baerenfaller, T. Brenzikofer, L. Baltzer, C. Vogler, L. Gschwind, C. Schneider, F. Streiff, P. M. A. Groenen and E. Miho, Traditional and Digital Biomarkers: Two Worlds Apart?, *Digit. Biomarkers*, 2019, **3**, 92–102.

75 J.D. Pierce, S. McCabe, N. White and R.L. Clancy, Biomarkers: An Important Clinical Assesment Tool, AJN, 2012, Vol. **112**, No. 9

76 S. P. Ingle, I. Ramona and Sukesh, The efficiency of the serum prostate specific antigen levels in diagnosing prostatic enlargements, *J. Clin. Diagnostic Res.*, 2013, **7**, 82–84.

77 R. Lang, V. Rolny, A. Leinenbach, J. Karl, M. Swiatek-de Lange, U. Kobold, M. Schrader, H. Krause, M. Mueller and M. Vogeser, Investigation on core-fucosylated prostate-specific antigen as a refined biomarker for differentiation of benign prostate hyperplasia and prostate cancer of different aggressiveness, *Tumor Biol.*, 2019, **41**, 1–12.

78 F. H. Schröder, J. Hugosson, M. J. Roobol, T. L. J. Tammela, M. Zappa, V. Nelen, M. Kwiatkowski, M. Lujan, L. Määttänen, H. Lilja, L. J. Denis, F. Recker, A. Paez, C. H. Bangma, S. Carlsson, D. Puliti, A. Villers, X. Rebillard, M. Hakama, U. H. Stenman, P. Kujala, K. Taari, G. Aus, A. Huber, T. H. Van Der Kwast, R. H. N. Van Schaik, H. J. De Koning, S. M. Moss and A. Auvinen, Screening and prostate cancer mortality: Results of the European Randomised Study of Screening for Prostate Cancer (ERSPC) at 13 years of follow-up, *Lancet*, 2014, **384**, 2027–2035.

79 P. Y. Lin, K. L. Cheng, J. D. McGuffin-Cawley, F. S. Shieu, A. C. Samia, S. Gupta, M. Cooney, C. L. Thompson and C. C. Liu, Detection of alpha-methylacyl-CoA racemase (AMACR) A biomarker of prostate cancer, in patient blood samples using a nanoparticle electrochemical biosensor, *Biosensors*, 2012, **2**, 377–387.

80 D. K. Yang, L. C. Chen, M. Y. Lee, C. H. Hsu and C. S. Chen, Selection of aptamers for fluorescent detection of alpha-methylacyl-CoA racemase by single-bead SELEX,

Biosens. Bioelectron., 2014, **62**, 106–112.

81 A. Oudhia, {UV}-{VIS} spectroscopy as a nondestructive and effective characterization tool for {II}-{VI} compounds, *Recent Res. Sci. Technol.*, 2012, **4**, 109–111.

82 UV/Vis/IR Spectroscopy Analysis of Nanoparticles, nanoComposix, 2012, v**1.1,** 1–6.

83 V. Kothekar, Basic UV-Vis Theory, Concepts and Applications Basic UV-Vis Theory, Concepts and Applications, *Protocol*, 2012, 1–28.

84 J. Clark, Absorbance The Beer-Lambert Law, 2016, **39**, 1–8.

85 B. S. Hameed, C. S. Bhatt, B. Nagaraj and A. K. Suresh, *Chromatography as an Efficient Technique for the Separation of Diversified Nanoparticles*, Elsevier Inc., 2018.

86 D. Duygu, T. Baykal, I. Açikgöz and K. Yildiz, Fourier transform infrared (FT-IR) spectroscopy for biological studies, *Gazi Univ. J. Sci.*, 2009, **22**, 117–121.

87 R. M. Amir, F. M. Anjum, M. I. Khan, M. R. Khan, I. Pasha and M. Nadeem, Application of Fourier transform infrared (FTIR) spectroscopy for the identification of wheat varieties, *J. Food Sci. Technol.*, 2013, **50**, 1018–1023.

88 J. M. Pérez-Donoso, J. P. Monrás, D. Bravo, A. Aguirre, A. F. Quest, I. O. Osorio-Román, R. F. Aroca, T. G. Chasteen and C. C. Vásquez, Biomimetic, mild chemical synthesis of Cdte-GSH quantum dots with improved biocompatibility, *PLoS One*, , DOI:10.1371/journal.pone.0030741.

89 S. Mourdikoudis, R. M. Pallares and N. T. K. Thanh, Characterization techniques for nanoparticles: Comparison and complementarity upon studying nanoparticle properties, *Nanoscale*, 2018, **10**, 12871–12934.

90 A. A. Bunaciu, E. gabriela Udriştioiu and H. Y. Aboul-Enein, X-Ray Diffraction: Instrumentation and Applications, *Crit. Rev. Anal. Chem.*, 2015, **45**, 289–299.

91 C. G. Pope, X-ray diffraction and the bragg equation, *J. Chem. Educ.*, 1997, **74**, 129–131.

92 B. Qiao, S. Zhao, Z. Xu and X. Xu, Synthesis of ZnO quantum dots and their agglomeration mechanisms along with emission spectra based on ageing time and temperature, *Chinese Phys. B*, , DOI:10.1088/1674-1056/25/9/098102.

93 N. Allec, M. Choi, N. Yesupriya, B. Szychowski, M. R. White, M. G. Kann, E. D. Garcin, M. C. Daniel and A. Badano, Small-angle X-ray scattering method to characterize molecular interactions: Proof of concept, *Sci. Rep.*, 2015, **5**, 1–12.

94 D. I. Svergun and M. H. J. Koch, Small-angle scattering studies of biological macromolecules in solution, *Reports Prog. Phys.*, 2003, **66**, 1735–1782.

95 D. M. A. M. Luykx, R. J. B. Peters, S. M. Van Ruth and H. Bouwmeester, A review of analytical methods for the identification and characterization of nano delivery systems in food, *J. Agric. Food Chem.*, 2008, **56**, 8231–8247.

96 J. Maes, N. Castro, K. De Nolf, W. Walravens, B. Abécassis and Z. Hens, Size and concentration determination of colloidal nanocrystals by small-angle x-ray scattering, *Chem. Mater.*, 2018, **30**, 3952–3962.

97 B.O. Dabbousi, J.Rodriguez-Viejo, F.V.Mikulec, J.R.Heine, H.Mattoussi, R.Ober, K.F.Jensem and M.G. Bawendi, (CdSe)ZnS Core-shell Quantum Dots: Synthesis and characterization of a Size Series of Highly Luminescent Nanocrystallites, *Am. Chem. Soc.*, 1997, **101**, 9463–9475.

98 S. K. Sharma, D. S. Verma, L. U. Khan, S. Kumar and S. B. Khan, *Handbook of Materials Characterization*, 2018.

99 A. De Gree, The History and Working Principle of the Scanning Electron Microscope (SEM), 2015, 1–8.

100 P. S. Kapatkar, R. B. Shettar, S. B. Kapatkar and N. R. Patil, Synthesis, Structural and Optical Investigation of CdSe semiconductor Quantum Dots, *IOP Conf. Ser. Mater. Sci. Eng.*, , DOI:10.1088/1757-899X/360/1/012009.

101 K. Scheerschmidt and P. Werner, Characterization of Structure and Composition of Quantum Dots by Transmission Electron Microscopy, 2002, 67–98.

102 T. Kogure, *Electron Microscopy*, Elsevier Ltd., 2nd edn., 2013, vol. 5.

103 X. Chen, Z. Guo and P. Miao, One-pot synthesis of GSH-Capped CdTe quantum dots with excellent biocompatibility for direct cell imaging, *Heliyon*, 2018, **4**, e00576.

104 Q. Wang, X. Qin, L. Geng and Y. Wang, Label-free electrochemical aptasensor for sensitive detection of malachite green based on au nanoparticle/graphene quantum dots/tungsten disulfide nanocomposites, *Nanomaterials*, , DOI:10.3390/nano9020229.

105 N. Elgrishi, K. J. Rountree, B. D. McCarthy, E. S. Rountree, T. T. Eisenhart and J. L. Dempsey, A Practical Beginner's Guide to Cyclic Voltammetry, *J. Chem. Educ.*, 2018, **95**, 197–206.

106 P. Sobrova, M. Ryvolova, J. Hubalek, V. Adam and R. Kizek, Voltammetry as a tool for characterization of CdTe quantum dots, *Int. J. Mol. Sci.*, 2013, **14**, 13497–13510.

107 J. K. Bhattarai, D. Neupane, B. Nepal, V. Mikhaylov, A. V. Demchenko and K. J. Stine, Preparation, modification, characterization, and biosensing application of nanoporous gold using electrochemical techniques, *Nanomaterials*, , DOI:10.3390/nano8030171.

108 O. A. Farghaly, R. S. Abdel Hameed and A. A. H. Abu-Nawwas, Analytical application using modern electrochemical techniques, *Int. J. Electrochem. Sci.*, 2014, **9**, 3287–3318.

CHAPTER THREE

CHAPTER 3

EXPERIMENTAL

3.0) Overview

This chapter describes the procedures for the synthesis of mercaptosuccinic acid capped tungsten telluride quantum dots (MSA Capped WTe_3 QDs), using a biocompatible water soluble synthesis route. Fabrication of a quantum dot based aptasensor is also described as well as the method used for detection of the analyte of interest, namely, AMACR. In addition, all reagents, materials and instrumentation employed in this study were outlined.

3.1) Reagents

Analytical reagent grade tungsten hexachloride (WCL_6) (≥ 99.9 trace metals basis), Tellurium powder (-30 mesh, 99.997% trace metals basis), Mercaptosuccinic acid (MSA) (≥ 99.0%), Sodium Borohydride ($NaBH_4$) (Powder, 98.0%), Sodium hydroxide (≥99.0%), Hydrochloric acid (HCL) (37%), Cysteamine (≥ 98.0%), 1-ethyl-3-(3-dimethylaminopropyl) carbodiimide hydrochloride (EDC) and N-hydroxysuccinimide (NHS) (98.0%) as well as Dulbecco's phosphate buffered saline (10 mM and 0.1 M, pH 7.4) were all purchased from Merck.

Aptamer sequence:

(CCCTACGGCGCTAACCCCATGCTACGAATTCGTTGTTAAACAATAGGCCACCGT GCTACAA-NH_2)

was purchased from Inqaba biotech, and recombinant alpha-methylacyl coenzyme A racemase (AMACR) was purchased from Biomatik USA.

3.2) Instrumentation

All electrochemical measurements were done using a PalmSens3 Potentiostat from PalmSens electrochemical interfaces (Netherlands) as well as a CHI electrochemical workstation. Conventional working electrodes, Ag/AgCl reference electrode and platinum wire counter electrode were all purchased from BASi®, polishing pads and slurries were all purchased from Buehler. Screen printed gold and carbon electrodes from Dropsens supplied by Metrohem. UV-Vis measurements were made using a Nicolet Evolution 100 UV-Visible spectrometer (Thermo electron, UK). HR-TEM images were taken using a Tecnai G2 F2OX-Twin MAT 200kV Field Emission Transmission Microscopy from FEI (Eindhoven, Neatherlands). All FT-IR spectra were recorded using a 100 FT-IR spectrometer by PerkinElma, USA. Small angle X-ray scattering was done by a SAXs instrument from Anton paar. And XRD measurements were taken using D8 advance diffractometer from Bruker AXS (Germany).

3.3) Experimental Procedure

3.3.1) Synthesis of MSA-WTe_3QDs

The MSA-WTe_3 QDs was prepared according to methods reported by (Yu et al, Elsevier Ireland, 2013) with some modifications.[1]

3.3.1.1) Preparation of Sodium hydrogen telluride (NaHTe) Solution

Tellurium (Te) powder (2.5 mM) was added to Sodium borohydride ($NaBH_4$) (5 mM) in a glass vial, the molar ratio between Tellurium and Sodium Borohydride was 1:2 respectively. 10 mL of doubly distilled water (Millipore systems) was added and used as a medium to allow the two powders to react. The glass vial was then covered in foil and parafilm used to seal the opening, after which holes were made to allow hydrogen gas produced as a product to escape. The following reaction resulted in the formation of hydrogen gas:

$$4NaBH_4 + 2Te + 7H_2O \rightarrow 2NaHTe + 14H_2 + Na_2B_4O_7 \quad [3.1]$$

NaHTe precursor reaction

This vial was then left overnight in a fridge at 4 ºC (as Tian et al, 2009, reported that this reaction works best in a place that is cold and dark),[2] after which a purple colour was obtained, indicating the completion of the NaHTe precursor reaction.

3.3.1.2) Preparation of MSA-WCl_6 ion solution

The second step of the MSA-WTe_3 synthesis required the preparation of an MSA-WCl_6 ion solution. WCl_6 (3.75 mM) was added to MSA (7.5 mM) with a molar ratio of 1,5:3 between tungsten hexachloride and mercaptosuccinic acid. 10 mL of doubly distilled water was added and mixed in a three neck round bottom flask, under a steady stream of nitrogen gas. After 5 minutes the pH of the solution was adjusted in order to enable the capping capabilities of MSA. The pH was adjusted to 8.21 using 5 M NaOH. Once the pH was adjusted the solution was allowed 40 minutes to react.

After 40 minutes 5 mL of NaHTe precursor was added drop wise into the MSA-WCl_6 ion solution and allowed a further 5 minutes to enable a good distribution of tellurium throughout the solution. Once mixed the solution was transferred to a Teflon vessel and placed into the microwave instrument and heated for 15 minutes at a constant temperature of 90 ºC.

Once the MSA-WTe_3 quantum dots were formed, they were removed from the microwave and quenched immediately by placing them in an amber bottle and into the freezer at -20 ºC.

After 5 minutes the QDs were then purified by a three step ethanol washing process, where ethanol was added to the MSA-WTe_3 QDs and centrifuged for 10 minutes at 1400 rpm. After each step the supernatant liquid was discarded carefully and the steps were repeated until a pellet of quantum dots sunk to the bottom of centrifuge tube. Finally, after three washing steps, all the liquid was discarded and the leftover pellet was dispersed in doubly distilled water for further characterization and application.

3.4) Sample Preparation

3.4.1) UV-Vis spectroscopy

10 cm^2 Quartz cuvettes were used for UV-Vis spectroscopy studies, quantum dots and its respective precursor solutions were analysed by UV-Vis following the procedure below:

First the cuvettes were cleaned using ethanol, and doubly distilled water, and allowed to dry under a steady stream of nitrogen gas. Then 2 mL of water (the solvent used in this study) was inserted into both the sample holder and reference cell in order to subtract the background signal of the solvent from the analyte UV-Vis spectrum. After this the QDs and its precursors were analysed, respectively.

3.4.2) FT-IR

FT-IR measurements were done using a flow cell. Here, the flow cell was cleaned using ethanol and water successively. The background was subtracted by running the solvent before any analysis was done. The MSA-WTe_3 quantum dots were then injected into the flow cell using two 5 mL syringes and allowed to coat the visible window of the cell in order to perform FT-IR analysis.

3.4.3) SAXs

Small angle x-ray scattering (SAXs) was done using a SAXspace small and wide angle scattering instrument from Anton paar, using 35 µL of QD sample in an aqueous solvent. Scattering curves where then collected in SaxDrive software, and treated using SaxQuiant and GIFT software in order to Fourier transform scattering curves into the appropriate PDDF distribution curves.

3.4.4) XRD

XRD samples were prepared by dropping 50 µL successively onto glass substrates in order to form a thin film. Measurements are performed using a multipurpose X-ray diffractometer D8-Advance from Bruker operated in a continuous 9-9 scan in locked coupled mode with Cu-K radiation. The sample is mounted in the center of the sample holder on a glass slide and leveled up to the correct height. The measurements run within a range in 2Θ defined by the user with a typical step size of 0.034° in 2Θ. A position sensitive detector, Lyn-Eye, is used to record diffraction data at a typical speed of 0.5 sec/step which is equivalent to an effective time of 92 sec/step for a scintillation counter.

3.4.5) HR-TEM

High resolution Transmission electron microscopy (HR-TEM), selected area electron diffraction together with EDS was performed using a Tecnai F20 Field emission transmission electron microscopy from FEI, Oregon, US. Samples were sonicated for about 30 minutes before successful dropping onto a nickel/copper grid and allowed to dry. Images were then taken and further analysed using ImageJ software in order to determine D-spacing.

3.5) Preparation of electrodes for electrochemical analysis of QDs

3.5.1) Characterization of MSA-WTe_3 using a Conventional Gold electrode

Conventional gold electrodes (AuEs) from Basi© were polished using 1.00 , 0.30 and 0.05 µM alumina polish slurries on separate polishing pads for 10 minutes. The AuEs was then sonicated using ethanol and distilled H_2O for 10 minutes, respectively, after which it was dried using nitrogen gas. Once dried, the AuEs was dipped into a 15 mM cysteamine solution and left in a dark space overnight in order to form a self-assembled monolayer (SEM). Once formed the electrodes was then rinsed gently with distilled water and dried with nitrogen to prepare for quantum dots immobilization. MSA-WTe_3 quantum dots were allowed to react with a (1:3) ratio EDC/NHS solution mixture in order to activate carboxyl groups present on its surface. After 30 minutes 10 µL of QDs were dropped onto the electrode and left to dry overnight in a dark cool space before electrochemical analysis.

3.5.2) Characterization of MSA-WTe_3 using a screen printed Gold electrode

Screen printed gold electrodes SPAuEs were purchased from Dropsense/Metrohem. Firstly 50 uL of 15 mM cysteamine was dropped onto the active surface of the SPAuEs and left overnight to allow the formation of a SAM on the surface, after this the electrodes were lightly rinsed with distilled water to remove any unbound molecules. MSA-WTe_3 QDs activated using the same method as mentioned in ***section 3.5.1*** above and dropped onto the electrodes and left to dry overnight before electrochemical analysis.

3.5.3) Characterization of MSA-WTe_3 using a Conventional Glassy carbon electrode

Conventional glassy carbon electrodes (GCEs) were thoroughly polished and cleaned using 1.00, 0.30 and 0.05 µM alumina polish slurries on separate polishing pads for 10 minutes. The GCEs was then sonicated using ethanol and distilled H_2O for 10 minutes, respectively, after which it was dried using nitrogen gas. Once dried the electrode was modified with the following electrochemical grafting steps:

i. Electrochemical grafting of 4-nitrophenyl layers on GCEs

400 µL of a 0.1 M $NaNO_2$ (or 2 mM) was added to 20 mL of solution containing 1 mM 4-nitroaniline and 0.5 M HCl under stirring at room temperature. The mixture was left to react for 5 minutes before using 2 mL of the solution in an electrochemical cell containing an Ag/AgCl reference electrode and platinum wire counter electrode that is connected to a Palmsens3 electrochemical workstation. Electrochemical modification of the GCEs surface is performed by 1 cycle of cyclic voltammetry scanned from + 0.7 V to - 0.4 V at a scan rate of 0.05 V/s and rinsed gently with distilled water.

ii. Electrochemical reduction of grafted 4-nitrophenyl layers to 4-aminophenyl

Once rinsed, the second step was underway where 2 mL of 1 M KCl was used in an electrochemical cell containing the GCEs. Electrochemical reduction was performed

by 5 cycles of cyclic voltammetry scanned from + 0.4 V to - 1.2 V at a scan rate of 0.05 V/s and rinsed with distilled water.

$MSA\text{-}WTe_3$ QDs were activated using the same method as mentioned ***in section 3.51*** and dropped onto the electrodes and left to dry overnight before electrochemical analysis.

3.5.4) Characterization of $MSA\text{-}WTe_3$ using a screen printed carbon electrode

Screen printed carbon electrodes (SPCEs) were first modified via electro-grafting of amine groups (***as described in section 3.5.3 (i) and 3.5.3 (ii)***), before QDs immobilization as reported in ***section 3.5.2***.

3.6) Fabrication of $MSA\text{-}WTe_3$ Aptasensor

For the final aptasensor fabrication, SPCEs were used as the substrate and modification steps are outlined below:

i. Electrografting of 4-aminophenyl layers onto SPCE surface

(*See section 3.5.3 above*).

ii. Immobilization of $MSA\text{-}WTe_3$ QDs onto the electrode

50 uL of quantum dots activated with EDC/NHS (250 mM /50 mM) was dropped onto the electrode and left in a dark, to dry overnight. At this point the electrode can be denoted by SPCE/QDs.

iii. Immobilization of aptamer onto SPCE surface.

50 uL of 4 µM amine modified aptamer specific to AMACR were dropped onto the electrode. First carboxylic groups present on the SPCE/QDs were activated using EDC/NHS (250 mM / 50 mM) for 30 minutes before washing the electrode with distilled water to get rid of any unbound material. The electrode at this stage is denoted by SPCE/QDs/APT (where APT=aptamer). The sensor was then stored in the fridge at 4 ºC and left overnight.

iv. Blocking buffer MCH

Non-specific binding site were blocked using 1 mM mercaptohexanol (MCH). After rinsing off unbound/excess amine modified aptamer, the SPCE/QDs/APT surface was incubated with 50 µL of MCH for 60 minutes, at 4 ºC. At this point the complete Aptasensor is denoted by: **SPCE/QDs/APT/MCH**

v. Incubation of AMACR biomarker on Aptasensor.

Different concentrations of the AMACR biomarker were allowed to incubate on the aptasensor overnight, at 4 ºC. The SPCE/QDs/APT/MCH surface was first rinsed, and thereafter incubated with 50 µL of different concentration of AMACR analyte. The aptasensor (SPCE/QDs/APT/MCH) were stored at 4 ºC when not in use, PBS at pH 7.4 was used as washing buffer during the washing step after each surface modification process. Scheme 3.1 below illustrates the different steps in the aptasensor fabrication process.

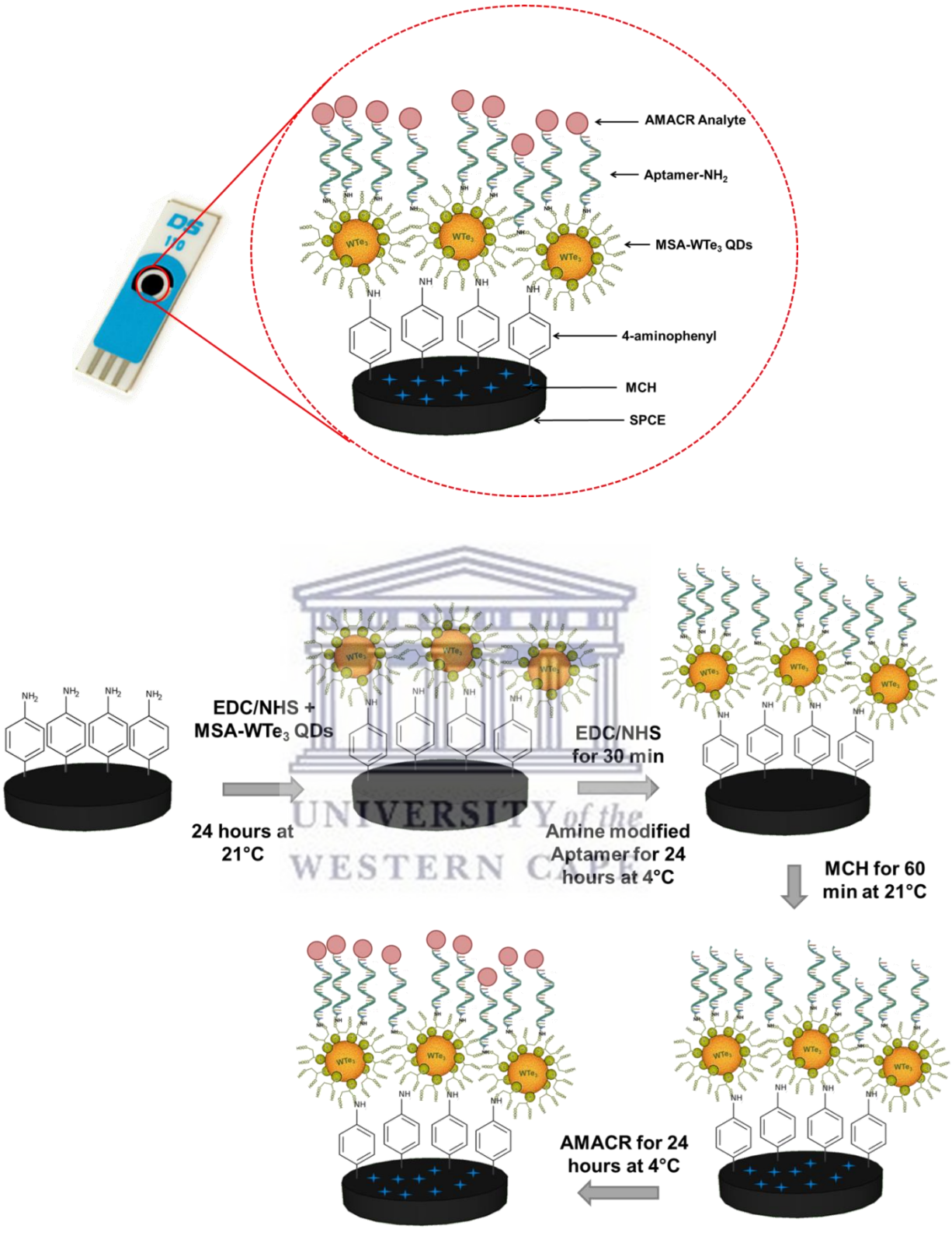

Scheme 3. 1: Fabrication steps in aptasensor development process. First QDs were immobilized onto the electrode, then aptamer was attached, and finally AMACR detected.

3.7) Electrochemistry Experimental Parameters

All experiments were done using Palmsens 3 electrochemical interfaces, Netherlands. All experiments were conducted in 10 mM PBS (phosphate buffer saline) pH 7.4 unless stated otherwise, as this buffer provided the ideal conditions for the system when working with biological material.

3.7.1) Electrochemical Impedance

All electrochemical impedance experiments were performed using the parameters listed below, unless stated otherwise:

Table 3. 1: Parameters for electrochemical impedance spectroscopy

Equilibration time (sec)	Scan type	Edc (V)	Eac (V)	Freq type	Number of freq	Max freq (Hz)	Min freq (Hz)	tMax,OCP (sec)	Stability criterion (mV/s)
3	Fixed potential	0.0	0.01	scan	41 = 10 dec	10 000	1.0	1.0	0.001

3.7.2) Cyclic Voltammetry and Differential Pulse Voltammetry

All cyclic voltammetric experiments were performed using the parameters listed below, unless stated otherwise:

Table 3. 2: Parameters for both CV and DPV experiments

Technique	Scan Rate	Potential window	Electrolyte solution
CV	10 mV/s – 100 mV/s	- 1.0 V to + 1.0 V	10 mM PBS pH 7.4
DPV	0.05 V/s	- 5.0 V to + 5.0 V	5 mM ferricyanide made in 10 mM PBS pH 7.4

Conclusion

Chapter three included specific details regarding reagents used in this study as well as instrumentation and their respective parameters used during operation of experiments. QDs synthesis was also discussed to give insight into the parameters that were optimized for MSA-WTe_3 QDs development (more on this will be discussed in chapter four). Fabrication steps of the sensor was also listed in this chapter, as each step has a specific role in overall sensor development and performance.

References

1 X. Yu, J. Liu, S. Zuo, Y. Yu, K. Cai and R. Yang, Application of mercaptosuccinic acid capped CdTe quantum dots for latent fingermark development, *Forensic Sci. Int.*, 2013, **231**, 125–130.

2 J. Tian, R. Liu, Y. Zhao, Q. Xu and S. Zhao, Controllable synthesis and cell-imaging studies on CdTe quantum dots together capped by glutathione and thioglycolic acid, *J. Colloid Interface Sci.*, 2009, **336**, 504–509.

CHAPTER FOUR

CHAPTER 4

RESULTS AND DISCUSSION

4.0) Overview

This chapter deals with the characterization of novel mercaptosuccinic acid capped WTe_3 QDs. Here, the optical, electronic and physical properties were studied using techniques such as UV-Vis and FT-IR spectroscopy, cyclic voltammetry (CV) and electrochemical impedance spectroscopy (EIS), as well as XRD. In addition, the size of the MSA-WTe_3 QDs was determined by SAXs and further confirmed by HR-TEM microscopic technique. In this chapter the properties of MSA-WTe_3 QDs are thoroughly discussed in accordance with literature standards as well as understanding the techniques and interpreting the information deduced from it. The response of the MSA-WTe_3 QDs based aptasensor in the absence and presence of AMACR analyte was also studied by DPV. Furthermore, the limit of detection (LOD) and limit of quantification (LOQ) of the MSA-WTe_3 QDs based aptasensor towards AMACR were also determined and compared to LODs reported in literature.

4.1) Quantum Dot Characterization

4.1.1) Ultraviolet-visible (UV-vis) Spectroscopy

Absorbance and band gap of QDs

The optical properties of the MSA-WTe_3 QDs was explored using absorbance. Precursors such as sodium hydrogen telluride (NaHTe) as well as tungsten hexachloride + mercaptosuccinic acid (WCl_6 + MSA) were also analysed using this technique. The absorbance spectrum for both the QDs and its respective precursors are shown in Figure 4.1.

As can be seen in Figure 4.1, the MSA capping agent exhibited a characteristic band at 233 nm while the combination of WCl_6 + MSA precursor resulted to an absorbance band at 241 nm which shifted from 233 nm to 241 nm due to the ligand to metal charge transfer. Interestingly, tellurium precursor obtained three characteristic profile bands at 234 nm, 282

nm and 370 nm. These bands are associated with the reduction of Te^{6+} to Te^{0} and Te^{0} to Te^{2-}, respectively.

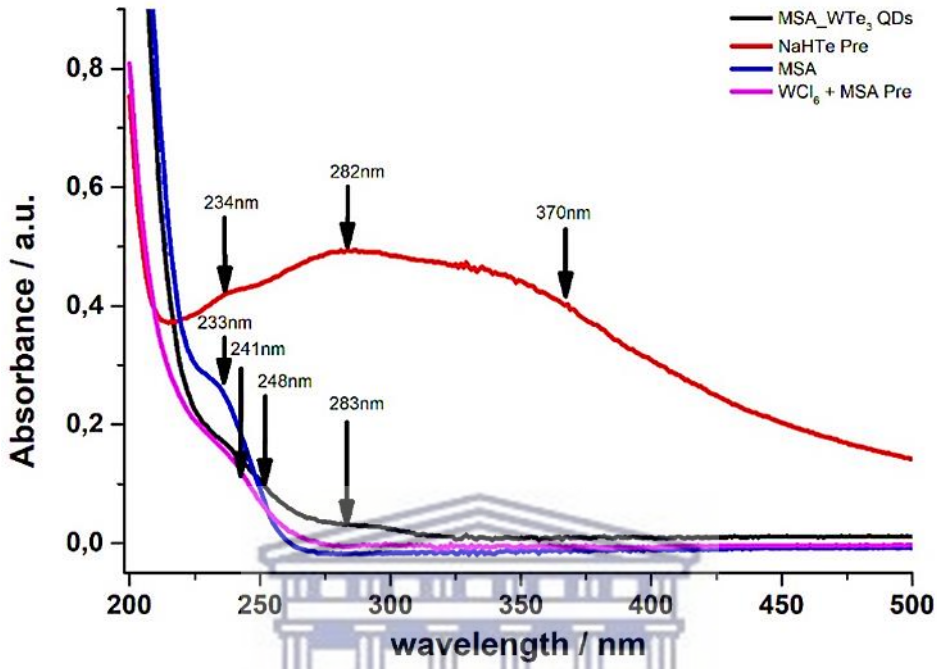

Figure 4. 1: Absorbance spectra of MSA-WTe_3 QDs, NaHTe and WCL_6 + MSA precursors, and MSA capping agent.

The lowest energy absorption feature of MSA-WTe_3 QDs is seen at 283 nm which could suggest that the quantum dots have a very broad size distribution. Due to broad size distribution, different band gap energies exist and thus electrons will get excited at a variety of wavelengths.[1] Optical properties of QDs arise due to the process where electrons are excited from the outer valence band to the conduction band, and this energy difference is known as the bandgap energy. When an electron is excited from the valence band a hole is left. The electron and its respective hole pair are then held together by electrostatic forces of attraction which forms an exciton. An exciton Bohr radius can be described as the distance between the hole and its electron pair, hence when the QDs diameter is smaller than the Bohr radius a phenomenon known as quantum confinement occurs. Here, electrons are only allowed to transition to discrete energy levels and continuous transitions are no longer

allowed. The energy levels of both the valence and the conduction band are now termed as 'quantized' and the energy values of each level are characteristic to the size of the particle.[2]

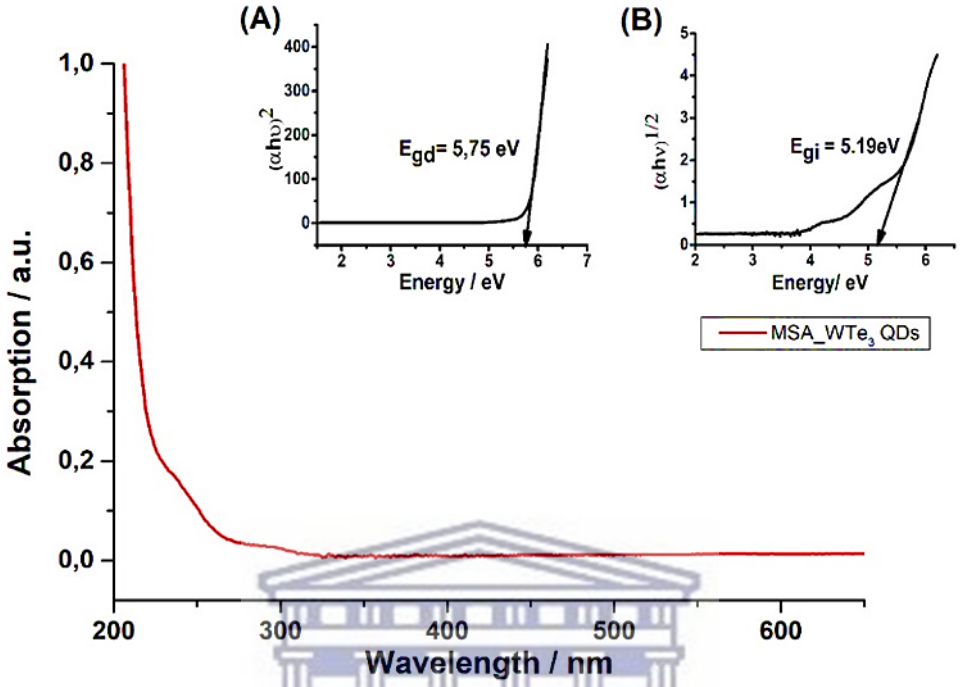

Figure 4. 2: MSA-WTe_3 QDs absorption band, where the left inset corresponds to the direct bandgap energy (A) and right inset corresponds to the indirect bandgap energy (B).

From the absorbance data the direct and indirect bandgap energies can be determined using the Tauc-relation as illustrated by Equation 4.1 below.[3]

$$\alpha h\nu = A\left(hV - E_g\right)^n \qquad [4.1]$$

Where, α = Absorption coefficient; h = Planck's constant; ν = frequency; A = constant and E_g = energy band gap; n = 2 when calculating the direct bandgap (Egd) and n = ½ when calculating the indirect bandgap (Egi).[3] Plotting the energy (hν) against either $\alpha h\nu^2$ or $\alpha h\nu^{0.5}$, the respective direct and indirect bandgaps can be determined by extrapolating the linear portion of the graph as shown in Figure 4.2 above. The bandgap energy of the QDs was found to be 5.75 for Eg_d and 5.19 for Eg_i, respectively.

4.1.2) Fourier Transform Infrared (FT-IR) Spectroscopy

Molecular bonding of capping agent

Structural properties of the quantum dots were further investigated using FT-IR. Figure 4.3 (A) and (B) below shows spectra obtained for both the MSA-WTe_3 QDs and its capping agent MSA, respectively.

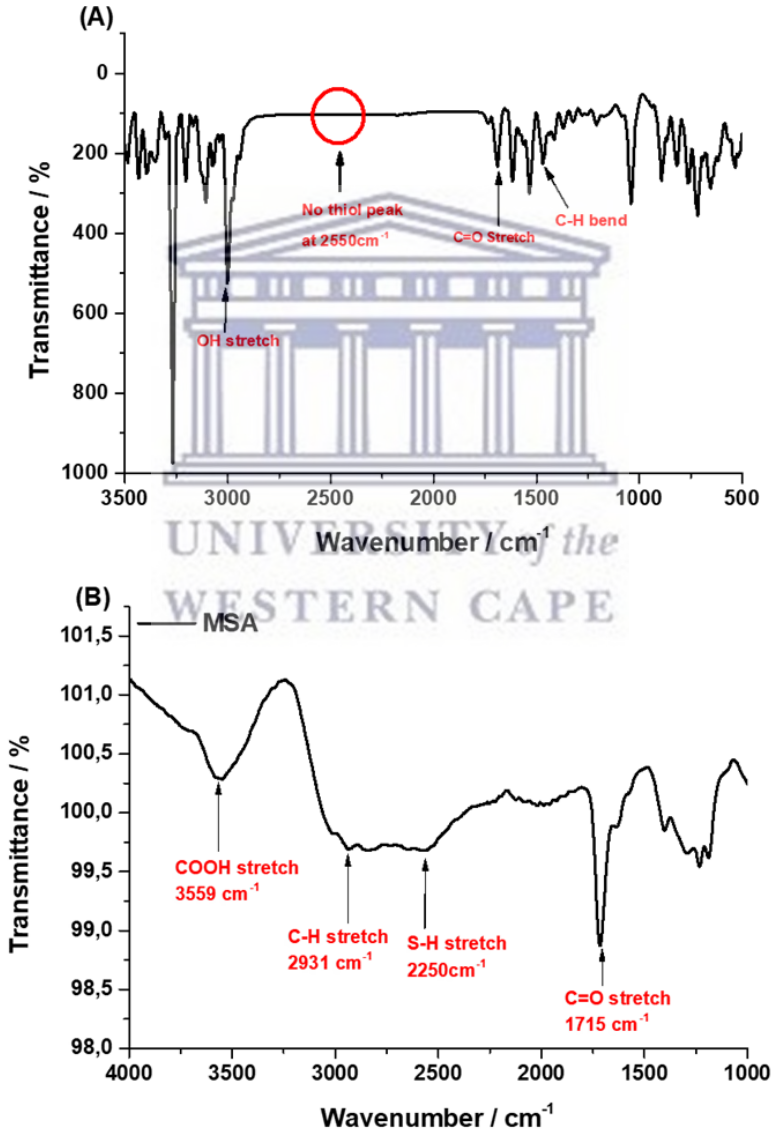

Figure 4. 3: FT-IR spectrum for MSA-WTe_3 QDs (A) and MSA capping agent (B).

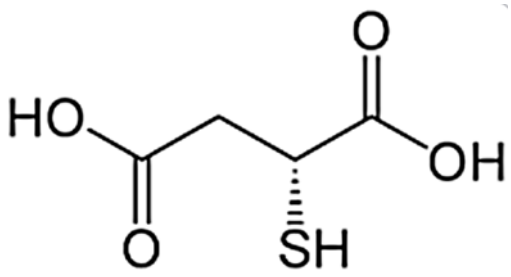

Figure 4. 4: Structure of mercaptosuccinic acid capping agent.

In Figure 4.3 (B), a characteristic peak at around 2550 cm^{-1} is observed and can be attributed to the stretching vibration of S-H (thiol bond),[4] however, the S-H bond diminished (as seen in Figure 4.3 (A)) indicating deprotonation of the S-H group and the formation of S-W bonds between the MSA molecule and the WTe_3 core. Further investigation of Figure 4.3 (A), reveals a peak at around 3000 cm^{-1} which could be due to the OH stretching vibrations of water molecules.[5] In addition, absorption bands at around 1430 cm^{-1} - 1560 cm^{-1} could be attributed to the stretching of carboxylic acid groups of the capping agent MSA, thus confirming successful capping of the MSA-WTe_3 QDs with MSA.[6] Figure 4.3 (B) also shows distinct peaks for C=O stretch at around 1715 cm^{-1}, a C-H stretch at 2931 cm^{-1} and a COOH stretch at 3559 cm^{-1}. These peaks are less prominent in comparison to the peaks observed in Figure 4.3 (A), which reveals that MSA characteristic peaks have diminished due to the formulation of QDs in aqueous solution.

4.1.3) X-ray Diffraction (XRD)

Chemical composition and Structure

X-ray diffraction was used to study the chemical composition and the stoichiometry of the MSA-WTe_3 QDs. The scanning angle range corresponds to 2 theta and ranged from 10º to 90º. Figure 4.5 below, shows the XRD pattern of the MSA-WTe_3 QDs. Here, characteristic bands corresponding to (100), (101), (102), (110), (111), (200), (201), (112) and (202) planes can be observed and it is in good agreement with the JCPDS (Joint committee on Powder diffraction standards) with a hexagonal structure. The amorphous hump at around 30º is related to the glass substrate used to immobilize the MSA-WTe_3 QDs on. The narrow intense peak represented by the (101) plane suggests that the MSA-WTe_3 QDs are crystalline.

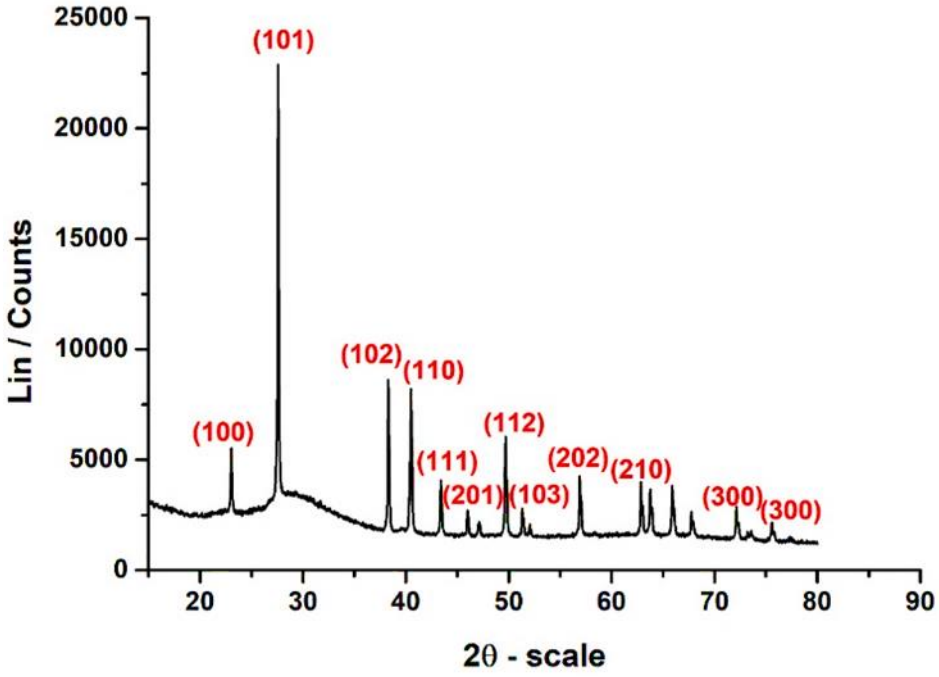

Figure 4. 5: X-ray diffractograms of MSA-WTe_3 QDs.

4.1.4) Small Angle X-ray Scattering (SAXs)

Particle Size, dispersion and stability in aqueous media

SAXs was used to investigate the particle size and size dispersion of the MSA-WTe_3 QDs in an aqueous medium. Information regarding the stability of the respective MSA-WTe_3 QDs and its agglomeration patterns were all studied using this technique. The advantage of using SAXs is that the MSA-WTe_3 QDs can be studied in its existing solvent thus eliminating the need for re-dispersion or drying steps.[7] The results obtained from the SAXs analysis was transformed into pair distance distribution function (PDDF) by volume, size distribution and by number function $N_N(r)$. The spectra of these parameters can be seen in Figure 4.6 and Figure 4.7 below. Here, MSA-WTe_3 QDs synthesized at different time periods are investigated, that is, QDs synthesized for 5 minutes and QDs synthesized for 30 minutes, respectively.

From Figure 4.6 (B), it is evident that the MSA-WTe_3 QDs had an average radius of 2 nm, and hence, an average diameter of 4 nm when studied in aqueous media. Figure 4.6 (A), however, gives information about the largest particle size detected which is around 17 nm. The irregular shape of the PDDF curve is indicative of aggregation occurring between the

particles; this means that the particles stick together to create particles with a larger radius. The PDDF curve in Figure 4.6 (A) also shows a dip into the negative region indicating the presence of the capping agent and confirms successful capping of the WTe_3 QDs with MSA capping agent.

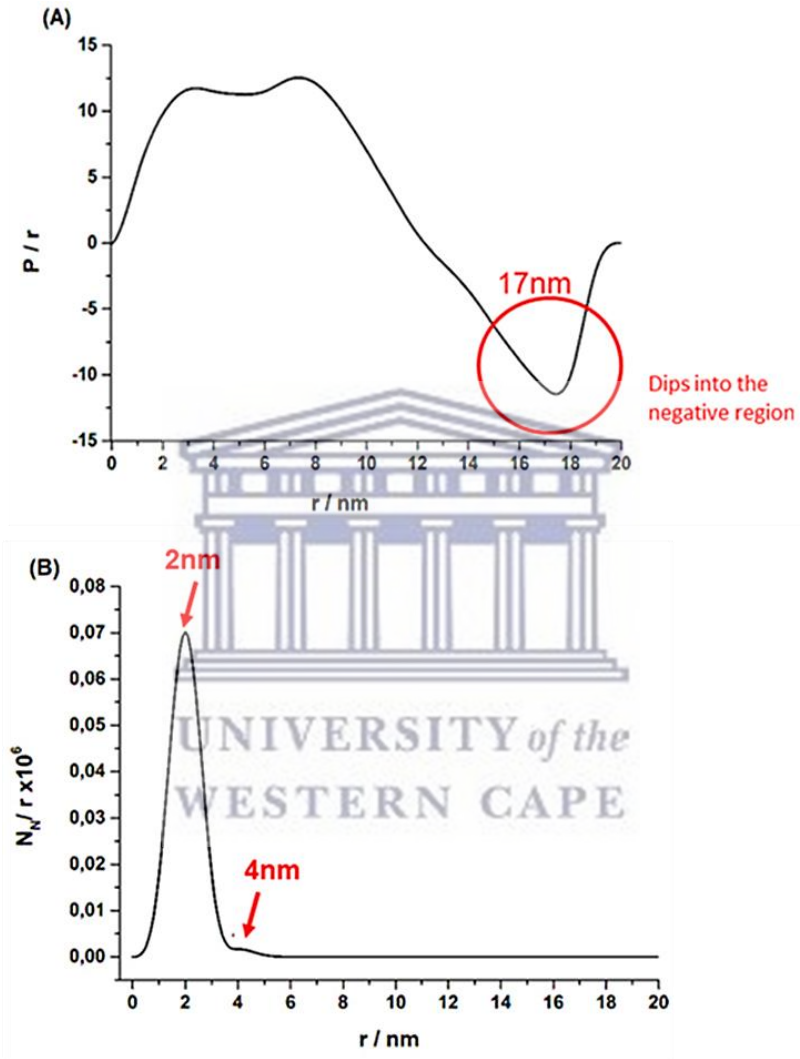

Figure 4. 6: SAXs data for MSA-WTe_3 QDs produced in 5 minutes by microwave irradiation. Here, the data are illustrated by PDDF (A) and particle radius (r) distributed by the number of particles (B), respectively.

A clear distinction can be seen between Figure 4.6 (B) and Figure 4.7 (B), where particle radius average has doubled, from 2 nm during the 5 minute synthesis to 4 nm radius during the 30 minutes synthesis. This observation confirms that the growth of the QDs during

microwave irradiation is time dependent,[8] and it is an important parameter which can be altered to optimize the electronic properties of the QDs. It should be noted that the electronic and optical properties of QDs are closely related to its size.[9]

Furthermore, the PDDF curve shown in Figure 4.7 (A) indicates that the largest QDs particle size is observed around 17 nm to 18 nm and that agglomeration of the particles still occurs. The dip into the negative region as seen in Figure 4.7 (A) confirms that MSA was still playing its role in terms of capping the WTe_3 QDs.

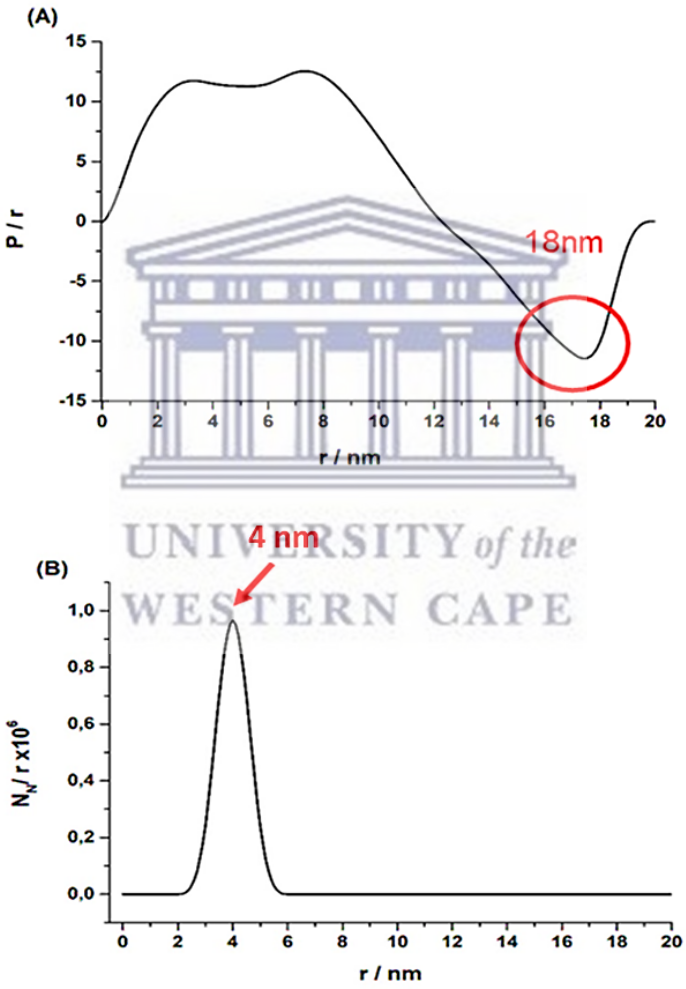

Figure 4. 7: Water soluble MSA-WTe_3 QDs produced in 30 minutes by microwave irradiation. Here, the data are illustrated by PDDF (A) and particle radius (r) distributed by the number of particles (B), respectively.

4.1.5) High Resolution Transmission Electron Microscopy (HR-TEM)

Particle size, morphology and crystallinity

MSA-WTe_3 QDs were studied using HR-TEM to confirm their size, morphology and crystallinity. Figure 4.8 (A) and (B) suggest that QDs are poly-dispersed and spherical in shape with sizes within the nanometer range. Figure 4.8 (C), shows that the QDs has an estimated size of 4 nm in diameter, with lattice fringes indicating good crystallinity of the sample. The distance between the lattice fringes are equivalent to the interplanar spacing also known as the 'd-spacing'. In the case of MSA-WTe_3 QDs the lattice fringes experienced are at 2.02, 2.17 and 3.70 angstrom. From the selected area electron diffraction pattern (SAED), it can be seen that small bright spots make up circular rings, indicating a polycrystalline sample.

MSA-WTe_3 QDs shown in Figure 4.8 was synthesized according to the following specific parameters, that is, (i) the QDs were synthesized for 5 minutes by microwave irradiation; (ii) the pH of the reaction medium was adjusted to 8.21; and (iii) a molar ratio of tungsten hexachloride to mercaptosuccinic acid to tellurium (WCl_6:MSA:Te) was 1.5:2:1, respectively. These parameters were optimized by isolating one parameter at a time, and studying the size and shape of the QDs produced. By optimizing different parameters like time, pH and molar ratios different types of nanomaterials can be obtained. It was evident that longer synthesis times resulted in larger tungsten telluride nanomaterial, either rods, or nanospheres or both.[10] The pH was also a very important parameter which had to be taken into account, as pH adjustment is important to de-protonate thiol groups present on mercaptosuccinic acid so successful capping of the QDs could take place. Ratios are also very important to ensure that limiting reagents are sufficient to allow the formation of QDs. Figure 4.9 to Figure 4.11 shows the different outcomes when synthesis parameters were isolated and studied.

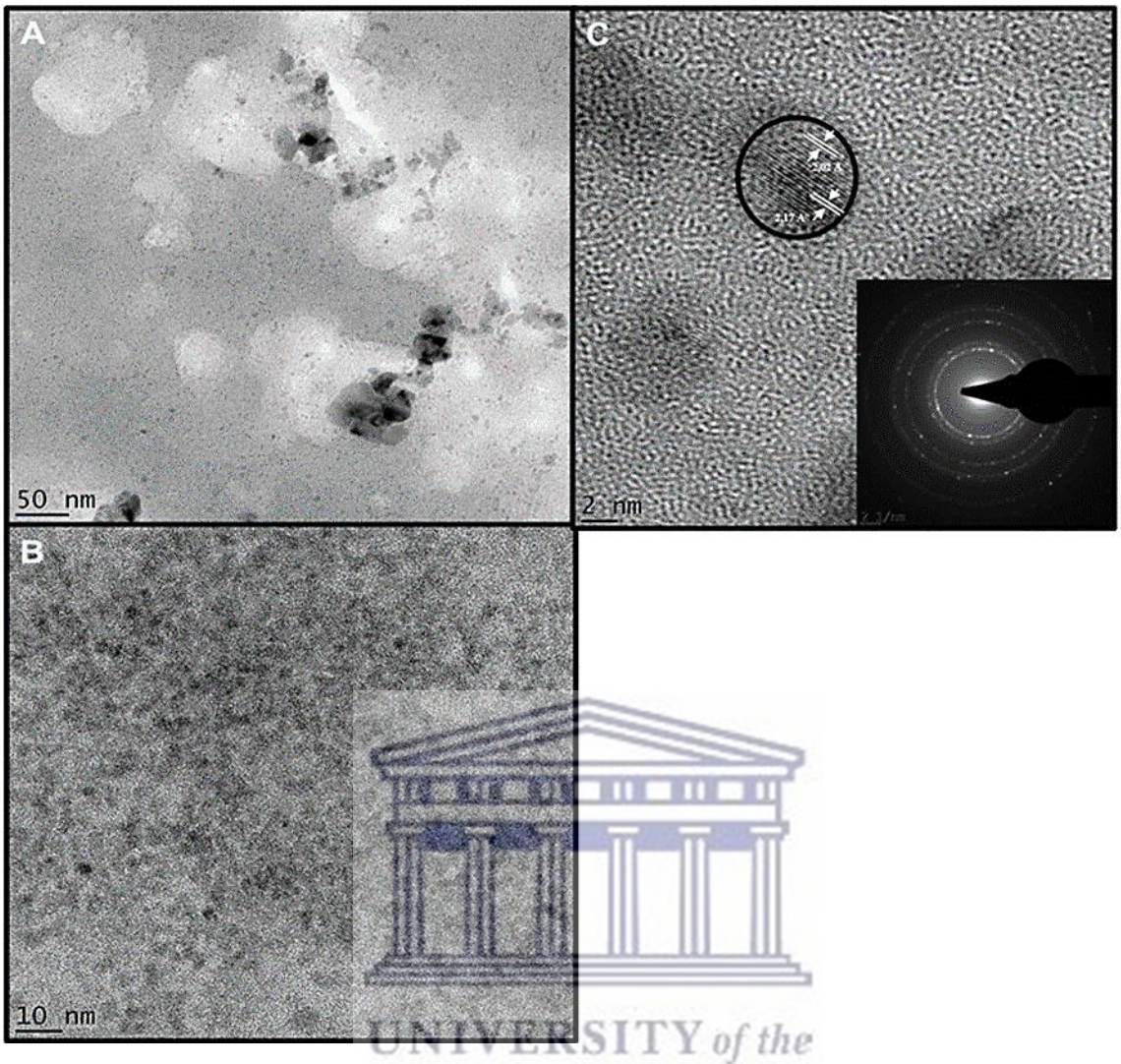

Figure 4. 8: HR-TEM images of MSA-WTe_3 QDs at different magnitudes, that is, 50 nm (A), 10 nm (B) and 2 nm (C). The inset in (C) represents the selected area electron diffraction pattern (SAED). *[Parameters for synthesis: Time = 5 min, pH = 8.21 and ratios (WCl_6:MSA:Te) were 1.5:2:1].*

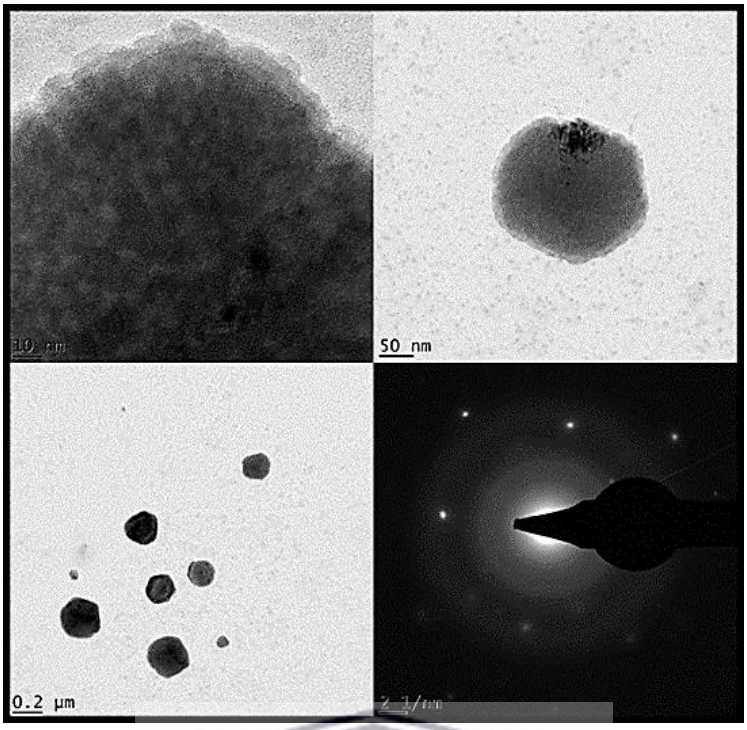

Figure 4. 9: HR-TEM images of MSA-WTe_3 QDs at different magnitudes, that is, 0.2 µm, 50 nm and 10 nm with the selected area electron diffraction pattern (SAED). *[Parameters for synthesis: Time = 20 min, pH = 8.21 and ratios (WCl_6:MSA:Te) was 1.5:2:1].*

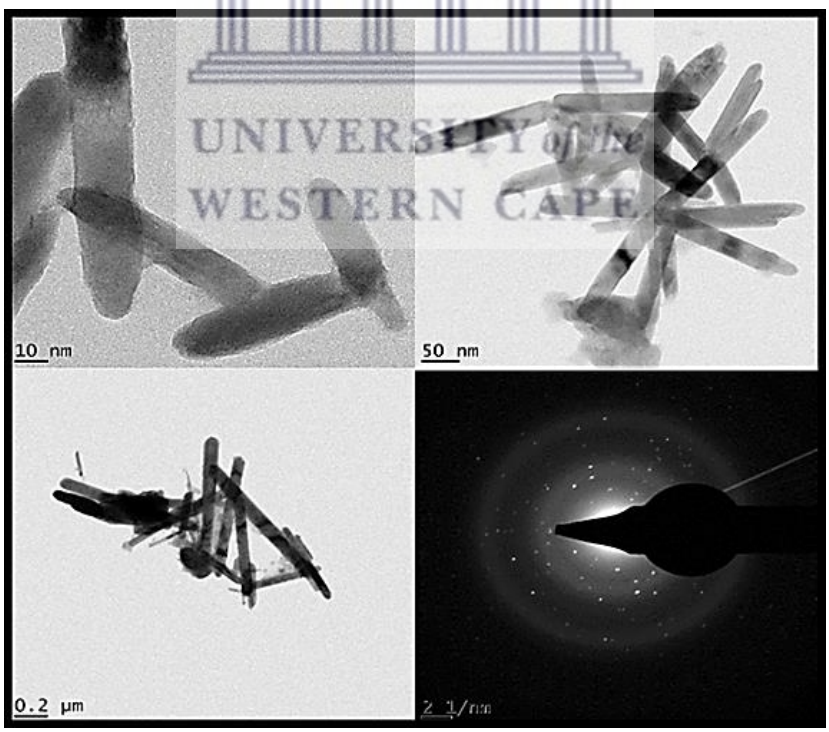

Figure 4. 10: HR-TEM images of MSA-WTe_3 QDs at different magnitudes, that is, 0.2 µm, 50 nm and 10 nm with the selected area electron diffraction pattern (SAED). *[Parameters for synthesis: Time = 20 min, pH = 9.5 and ratios (WCl_6:MSA:Te) was 1.5:2:1].*

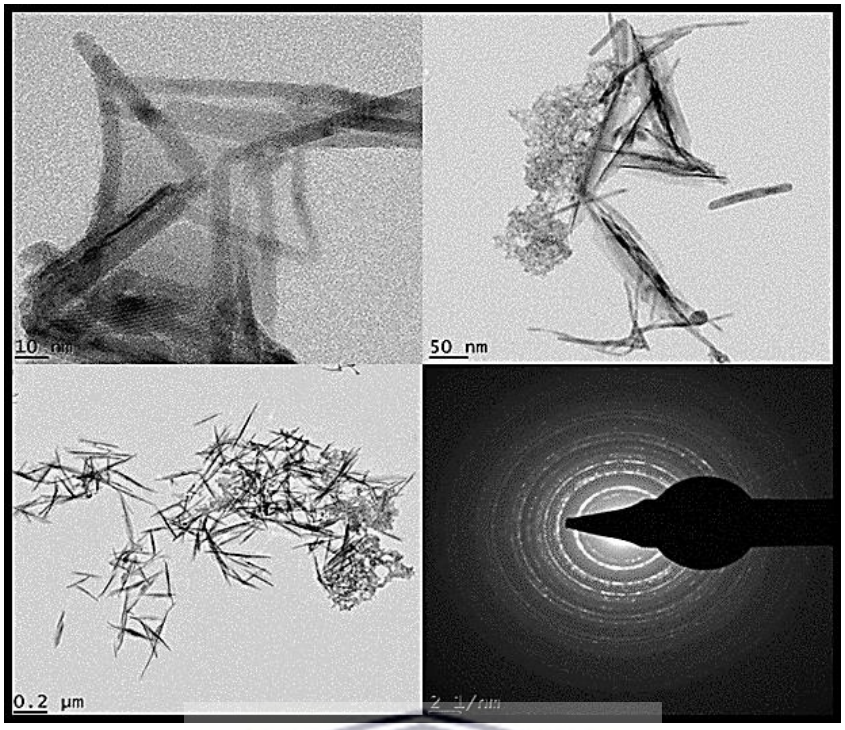

Figure 4. 11: HR-TEM images of MSA-WTe_3 QDs at different magnitudes, that is, 0.2 µm, 50 nm and 10 nm with the selected area electron diffraction pattern (SAED). *[Parameters for synthesis: Time = 1 Hour, pH = 8.21 and ratios (WCl_6:MSA:Te) was 1.5:2:1].*

Figure 4.9 shows HR-TEM micrographs for tungsten telluride nanomaterials produced via microwave synthesis, where time for the reaction was 20 minutes. From Figure 4.9, it is evident that different sized nanoclusters are formed. The bright spots observed in the SAED image suggest that the nanoclusters are crystalline. Figure 4.10 shows the formation of tungsten telluride nanorods. Here, the time for synthesis was kept at 20 minutes, but the pH of the reaction solution was adjusted to 9.5. The SAED confirms that the nanorods have a crystalline component to it. Figure 4.11 shows wire like nanostructures, which were formed over a time period of an hour. The SAED shows diffuse rings which suggest that the nanowires are amorphous. It should be noted that all other parameters were kept constant for the different nanomaterial structures formed and only those mentioned was changed. These HR-TEM micrographs prove that QDs size and shape are highly dependent on reaction parameters and are especially sensitive to changes in pH.

4.1.6) High Resolution Scanning Electron Microscopy (HR-SEM)

Morphology of Quantum dots and aptamer binding

From Figure 4.12 (B) and (C) below the QDs appeared to be spherical in shape and it seems like they are fused together. The pH of the reaction solution also plays a huge role as the capping agent might not have been successfully de-protonated during the synthesis process and as such could not maintain its colloidal stability (as seen in accordance with TEM data in Figure 4.8).[11] The elemental composition of MSA-WTe_3 QDs was studied using EDS, as seen in Figure 4.12 (D). It is evident that the QDs are rich in both tellurium and tungsten. Other elements such as carbon (C), sulphur (S), as well as oxygen (O) are also present and can be attributed to the capping agent, mercaptosuccinic acid. Furthermore, other elements such as sodium (Na) results from using sodium borohydride ($NaBH_4$) as a reducing agent in order to reduce tellurium and Cl is a result of the tungsten hexachloride (WCl_6) precursor.

Upon further study MSA-WTe_3 QDs still remained aggregated, however, the HR-SEM micrograph showed some distinct visible changes upon the introduction of the amine modified aptamer, as shown in Figure 4.13 (B) and (C). These morphological changes could be attributed to the nature of the aptamers and how they bind to the QDs. In the work done by Jones and co-workers, similar changes were observed when single stranded DNA was immobilized onto spherical gold nanoparticles, the nanoparticles then arranged themselves into two different types of cubic crystals, face centred and body centred. In Figure 4.12 the QDs were first spherical in shape, but addition of the aptamer caused the QDs to rearrange and form cubic like structures, as seen in Figure 4.13 (C).

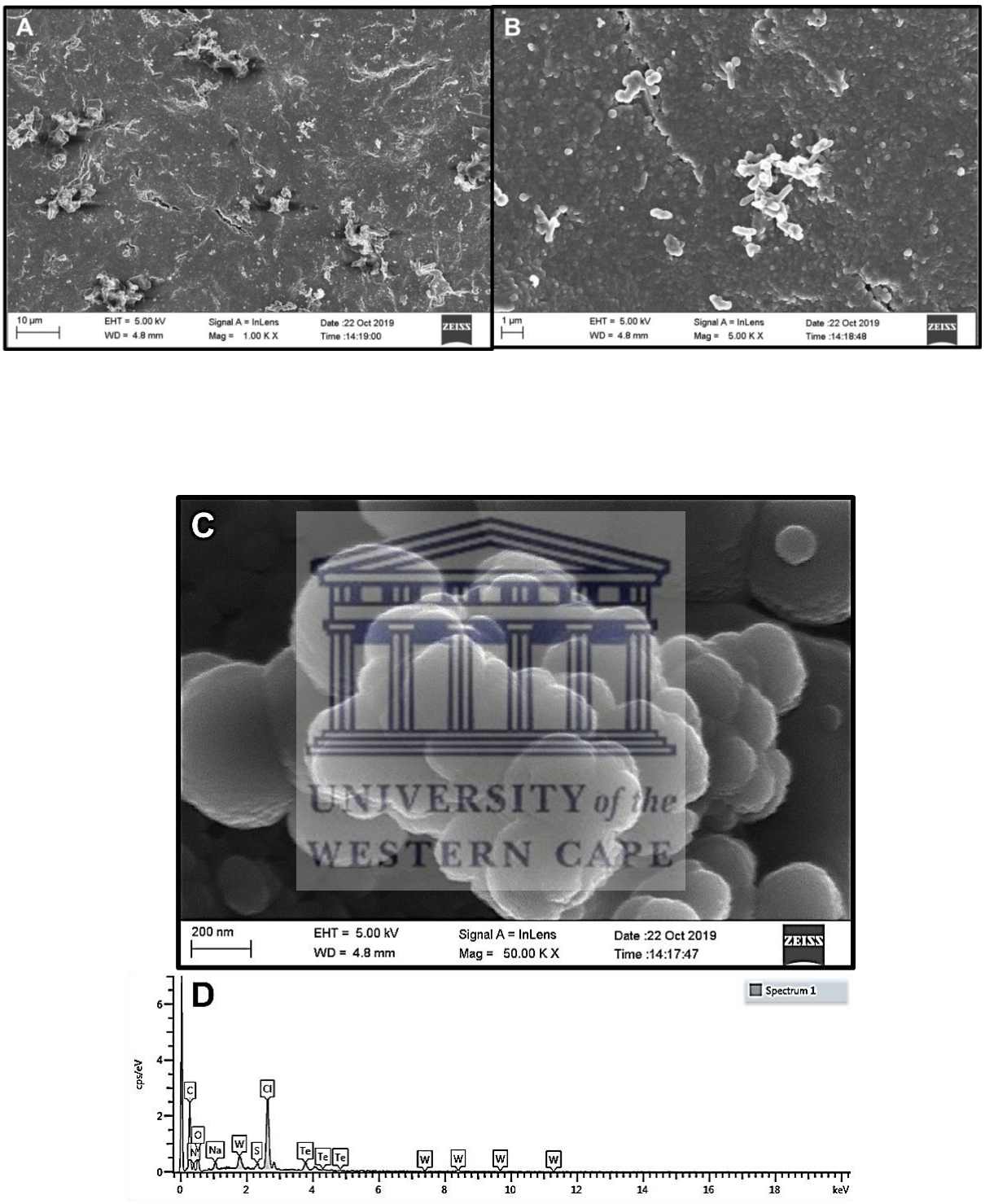

Figure 4. 12: HR-SEM micrographs of MSA-WTe_3 QDs at different magnifications, that is, 10 µm (A), 1 µm (B) and 200 nm (C), respectively, while the EDS spectrum of the MSA-WTe_3 QDs is shown in (D).

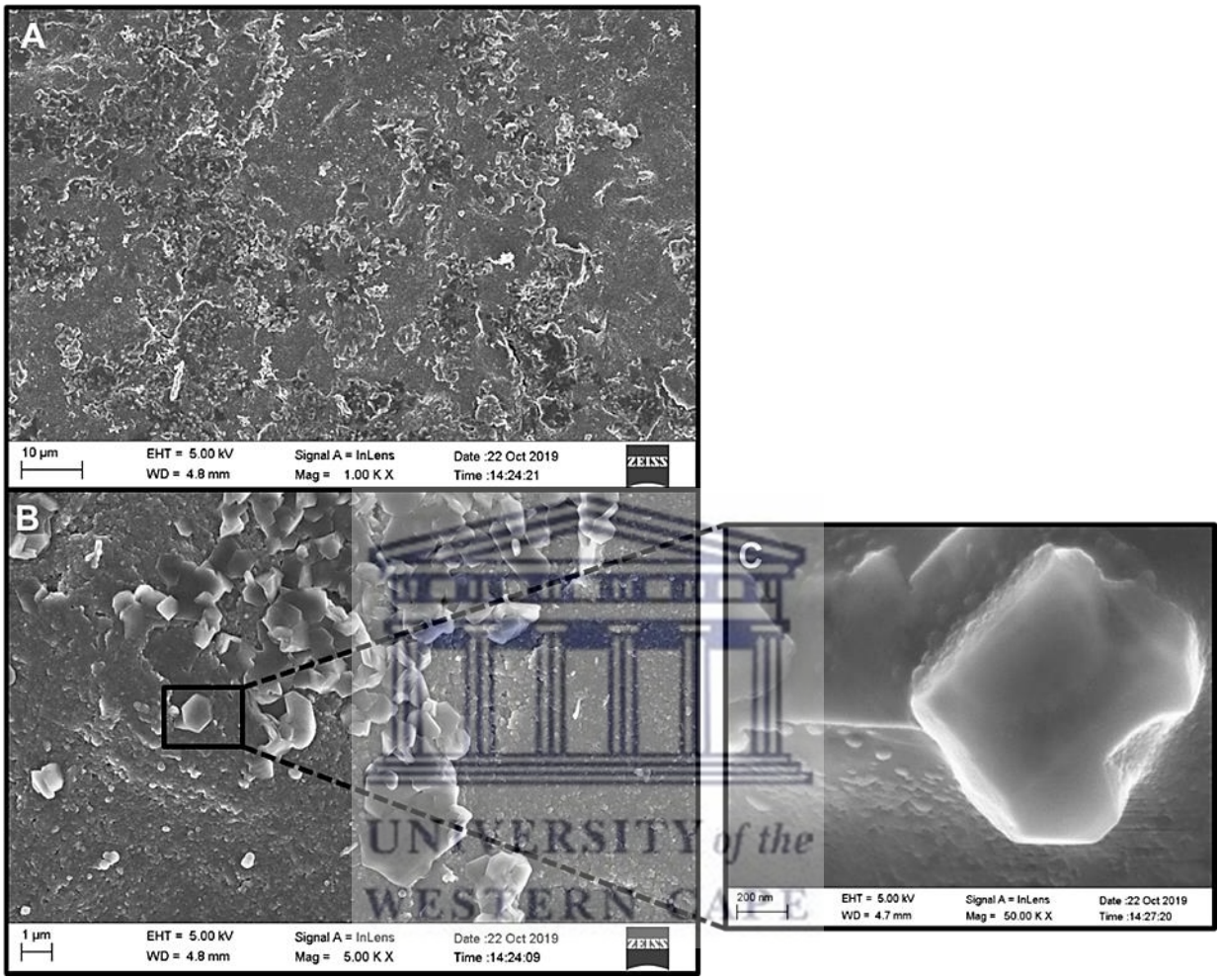

Figure 4. 13: HR-SEM micrographs of APT-MSA-WTe_3 QDs at different magnifications, that is, 10 µm, 1 µm and 200 nm, respectively.

4.1.7) Cyclic Voltammetry (CV)

Electrochemical properties

The electrochemical behaviour of MSA-WTe_3 QDs was investigated using techniques such as cyclic voltammetry and electrochemical impedance spectroscopy. The novel MSA-WTe_3 QDs were studied in solution as well as immobilized onto various electrode substrates by methods described in ***chapter three, section 3.5*** in order to establish which platform would yield the best results for further applications in biosensor/aptasensor fabrication protocols.

Conventional Au and GC electrodes were used to explore the electrochemical properties of the MSA-WTe_3 QDs precursors. Peaks for the MSA-WTe_3 QDs were accounted for by first investigating the cyclic voltammograms of both precursor solutions, that is, NaHTe and MSA-WCl_6. Figure 4.14 (A) and (B) shows the CVs of NaHTe and MSA-WCl_6, respectively, in 10 mM PBS, pH 7.4. Here, 'A' denotes anodic peaks and 'C' denotes cathodic peaks. From Figure 4.14 (A) it is evident that two anodic peaks are visible, that is, A_2 at $E_{p,a}$ = + 325 mV, which can be associated with Te^{4+}, while A_1 at $E_{p,a}$ = + 550 mV might be due to the oxidation of Te^{4+} to Te^{6+}.

In addition, two reduction peaks can also be observed, that is, C_1 with an $E_{p,c}$ = - 315 mV, which can be attributed to the reduction of tellurium from Te^{4+} to Te^0, and C_2 with an $E_{p,c}$= - 600 mV, which might be due to the reduction of tellurium from Te^0 to Te^{2-}.

Peaks observed at more negative potentials approximately around - 700 mV is due to onset of hydrogen evolution.[12] However, peaks observed at more positive potentials beyond + 500 mV could be associated with the formation of gold oxide. [13]

*4.1.7.1) **Precursors Characterization using cyclic voltammetry***

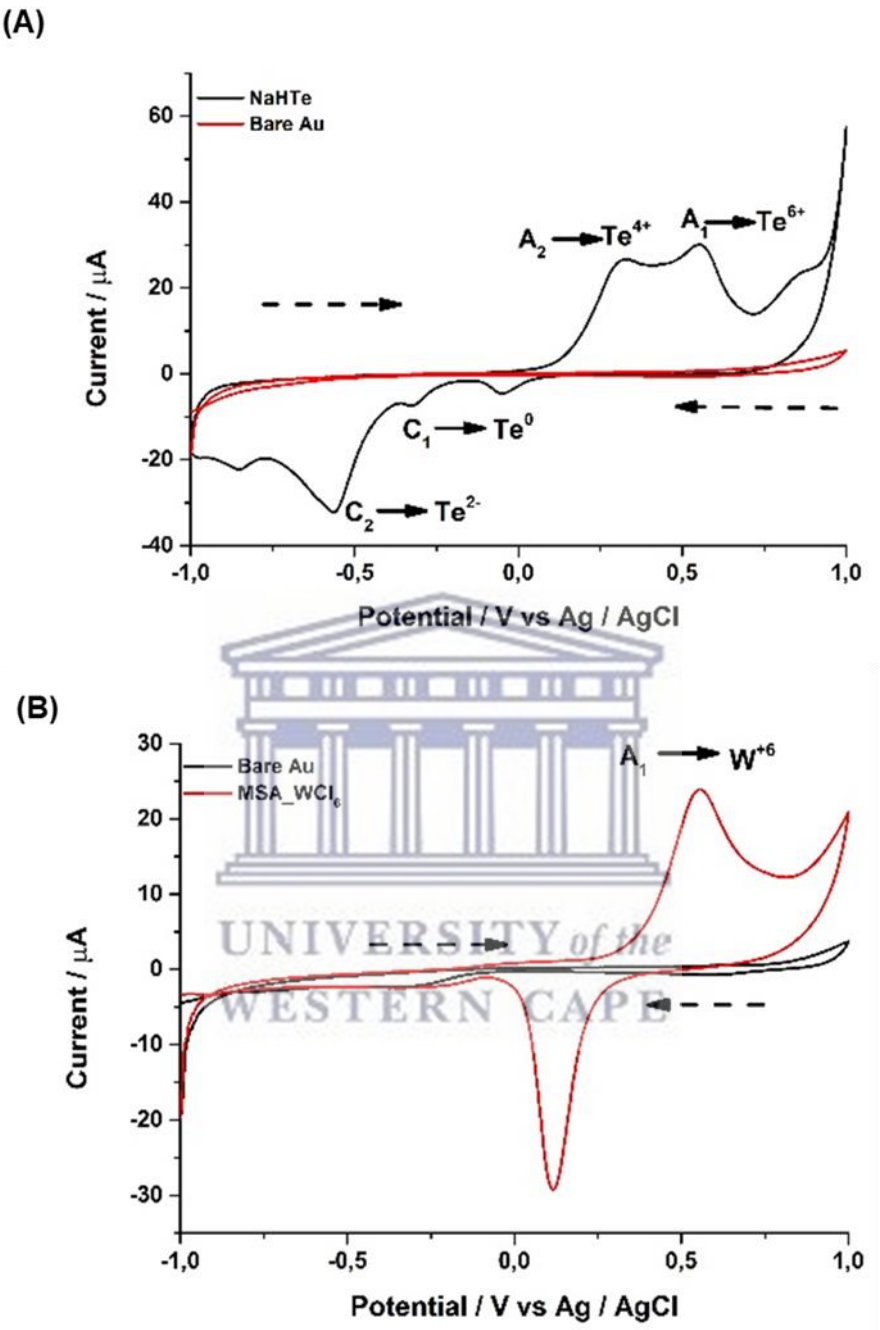

Figure 4. 14: Cyclic voltammograms of NaHTe (A) and MSA-WCl_6 (B) at a conventional gold electrode (AuE), in 10 mM PBS, pH 7.4, at a scan rate of 100 mV/s.

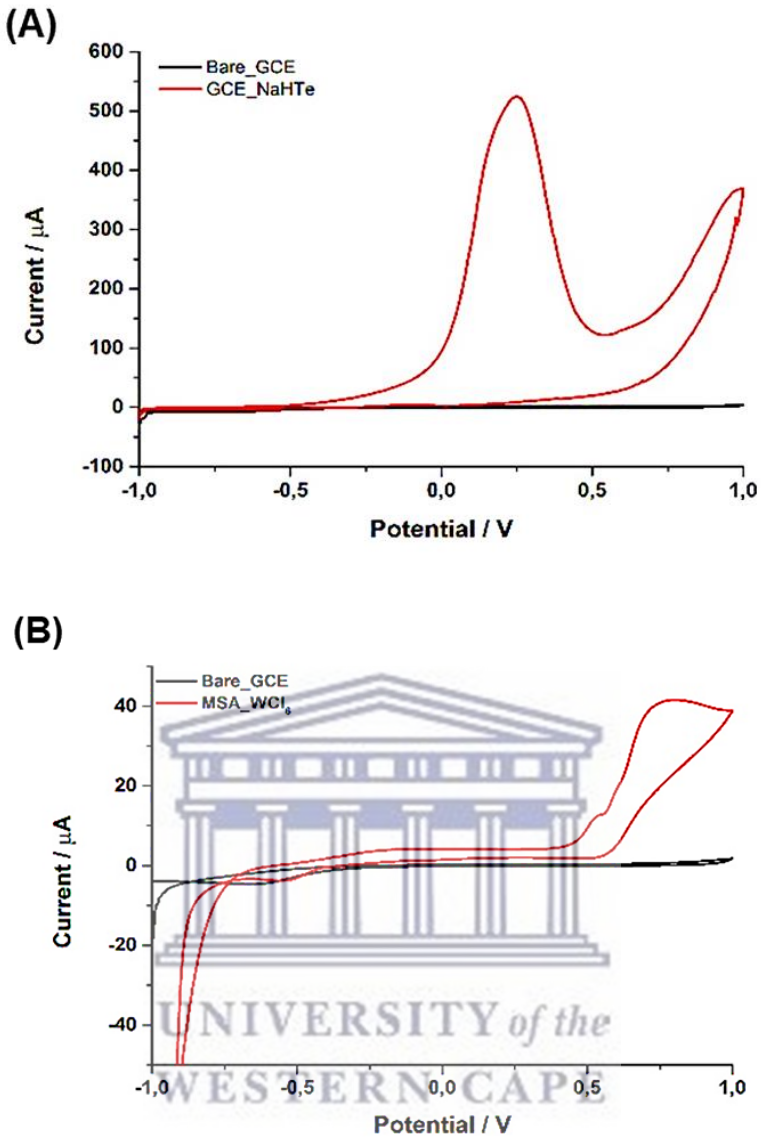

Figure 4. 15: Cyclic voltammograms of NaHTe (A) and MSA-WCl_6 (B) at a conventional glassy carbon electrode (GCE), in 10 mM PBS, pH 7.4, at a scan rate of 100 mV/s.

The NaHTe precursor was further investigated at a conventional glassy carbon electrode. From Figure 4.15 (A), a very prominent peak at around $E_{p,a}$ = 250 mV was observed. This peak may be attributed to the oxidation of tellurium from Te^{4+} to Te^{6+}, however, a shift in the peak position is visible. This might be due to the fact that a different electrode substrate was employed. A study done by Mundinamani and co-workers[14] found that the type of electrode used, surface modification of an electrode as well as the electrolyte solution of an electrochemical cell can all affect the cyclic voltammograms produced. Chemical binding

processes on different electrodes also play a role in the displacement of reduction/oxidation peak positions, as experienced when studying NaHTe using two different working electrodes.[14]

Figure 4.14 (B) shows the CV response of the MSA-WCl_6 precursor in 10 mM PBS, pH 7.4. From Figure 4.14 (B), an anodic peak A_1 at $E_{p,a}$ = 554 mV can be observed, which can be due to the oxidation of tungsten from W^{5+} to W^{6+}.[15] In the work done by Maxime and co-workers[16], the electrochemical behaviour of a tungsten-gold nanocomposite material was investigated by CV; the resulting cyclic voltammogram appeared to be strikingly similar to the CV illustrated in Figure 4.14 (B). However, anodic and cathodic peaks are shifted this could be due to the electrolyte solution used, in their case, sulphuric acid.[16] Contrary to this, conventional AuE also have its own characteristic peaks which could overlap with the peaks of the MSA-WCl_6 precursor. Figure 4.15 (B) shows the cyclic voltammogram of MSA-WCl_6 studied at the conventional GCE. From Figure 4.15 (B) it becomes apparent that around $E_{p,a}$ = + 550mV a broad peak is observed, which could be related to the oxidation of tungsten. However, there are no reduction peaks observed, which could be subject to the type of electrode used or the electrolyte solution used, in this case, glassy carbon and phosphate buffer, respectively.

Hence, after investigating precursors in solution for both conventional Au and GC electrodes, it can be seen that the characteristic anodic peaks for tellurium overlap with that of tungsten, and as such, can be considered as the QDs peaks.

4.1.7.2) <u>Quantum dots characterization using different electrode platforms</u>

After investigating the electrochemical properties of NaHTe and MSA-WCl_6 precursors, the electrochemical properties of MSA-WTe_3 QDs were then analysed keeping in mind the characteristic peaks of each precursor as to assign electrochemical peaks relevant to that of the QDs. From Figure 4.16 (A) and (B) a peak denoted by **A_1** at approximately $E_{p,a}$ = + 375 mV can be observed. This is the peak characteristic of the QDs since it's a combination of the anodic potentials of both NaHTe and MSA-WCl_6. This peak appears to be stable and increase as the scan rate increases. In addition, it is evident that for both solution and surface bound QDs, the peak shifts to more positive potentials, this confirms that the reaction at the electrode surface are governed by slow electron processes.[1]

4.1.7.2.1) Conventional gold electrode (AuE)

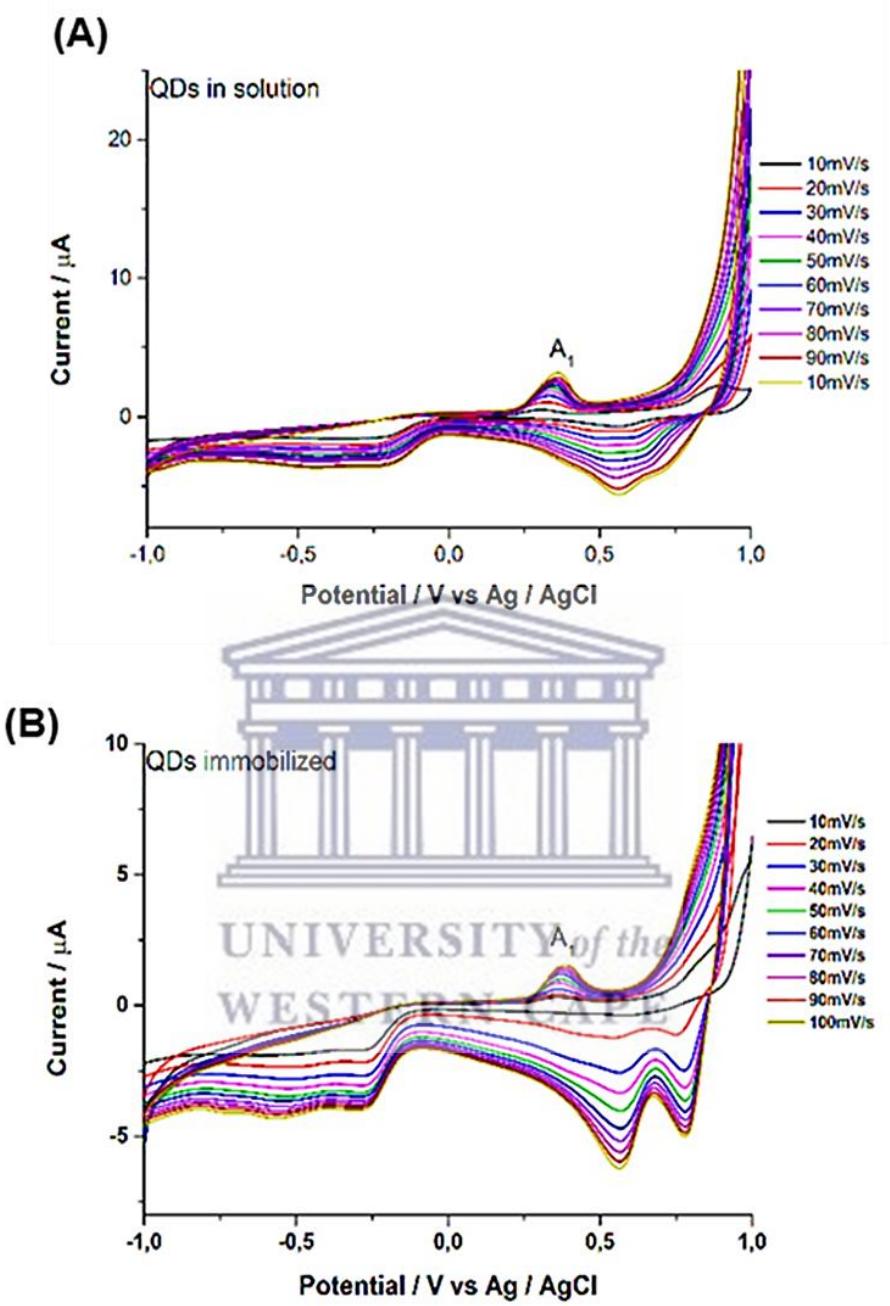

Figure 4. 16: CVs of MSA-WTe_3 QDs in solution at a conventional AuE (A) and immobilized on a conventional AuE (B) in 10 mM PBS, pH 7.4, at different scan rates in the range from 10 mV/s to 100 mV/s.

4.1.7.2.2) Conventional glassy carbon electrode (GCE)

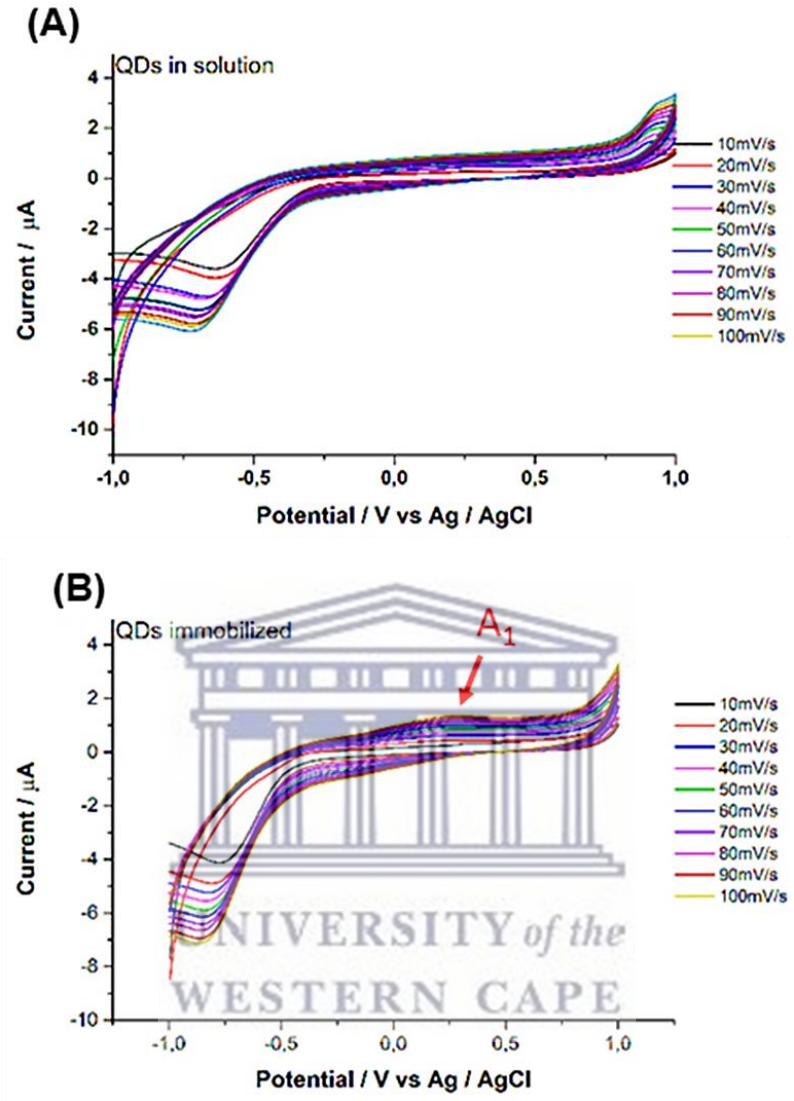

Figure 4. 17: CVs of MSA-WTe_3 QDs in solution at a conventional GCE (A) and immobilized on a conventional GCE (B) in 10 mM PBS, pH 7.4, at different scan rates in the range from 10 mV/s to 100 mV/s.

Conventional GCEs were also used to investigate the electrochemical properties of the MSA-WTe_3 QDs in solution and surface bound QDs, as shown in Figure 4.17 (A) and (B), respectively. By studying the CV curves it is evident that the CV for the surface bound QDs exhibited a peak at $E_{p,a} \approx +$ 300 mV, which is due to the oxidation of the MSA-WTe_3 QDs. However, in Figure 4.17 (A) no QDs peak can be observed. This may be attributed to the slow electron transfer processes between the solution species and the electrode surface.

4.1.7.2.3) Screen printed gold electrode (SPAuE)

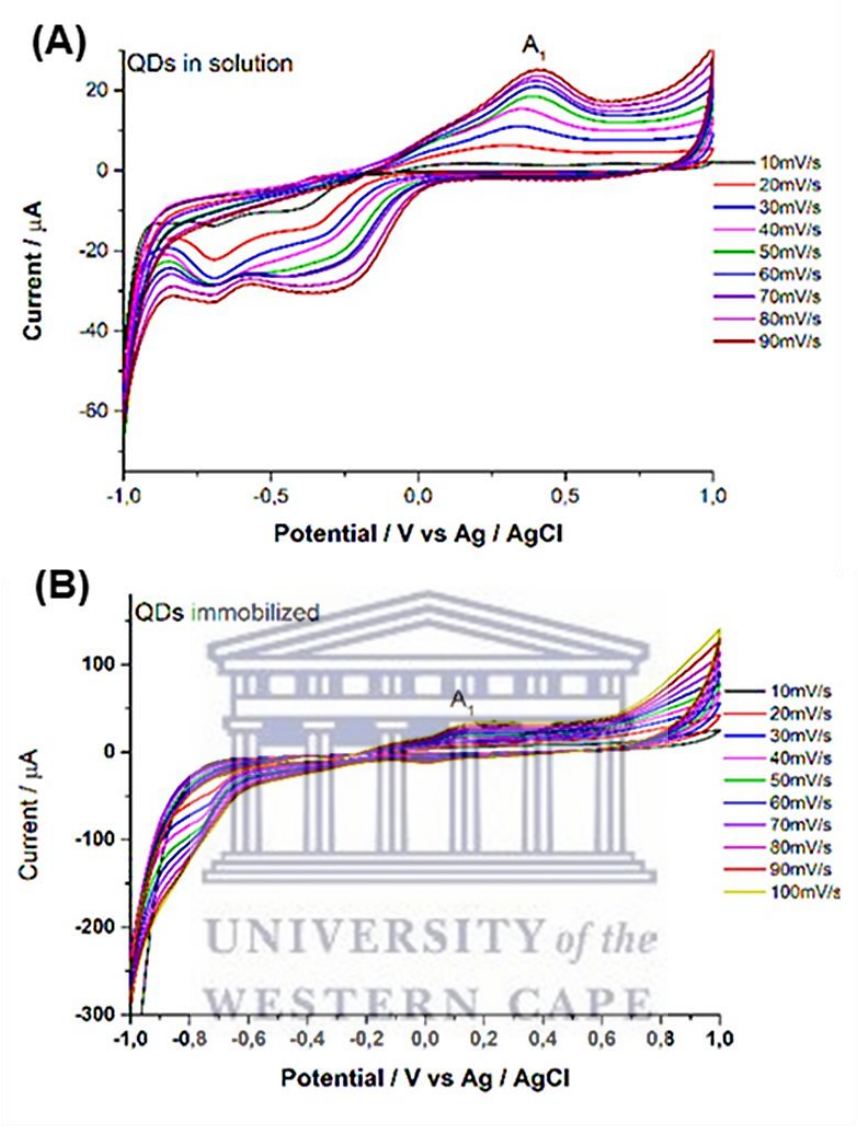

Figure 4. 18: CVs of MSA-WTe_3 QDs in solution at a SPAuE (A) and immobilized on a SPAuE (B) in 10 mM PBS, pH 7.4, at different scan rates in the range from 10 to 100 mV/s.

Screen printed gold electrodes (SPAuEs) were also used to characterize the MSA-WTe_3 QDs as shown in Figure 4.18. It can be seen that the CV response for both the surface bound QDs (Figure 4.18 (B)) and QDs in solution (Figure 4.18 (A)) are similar, however, the characteristic peaks of the QDs are more pronounced and prominent when QDs were studied in solution, as compared to QDs immobilized on the surface of the SPAuE. This could be due

to QDs having enough space to interact with its surrounding electrolyte and create a larger exchange of electrons in order to generate more pronounced peaks.

4.1.7.2.4) Screen printed carbon electrode (SPCE)

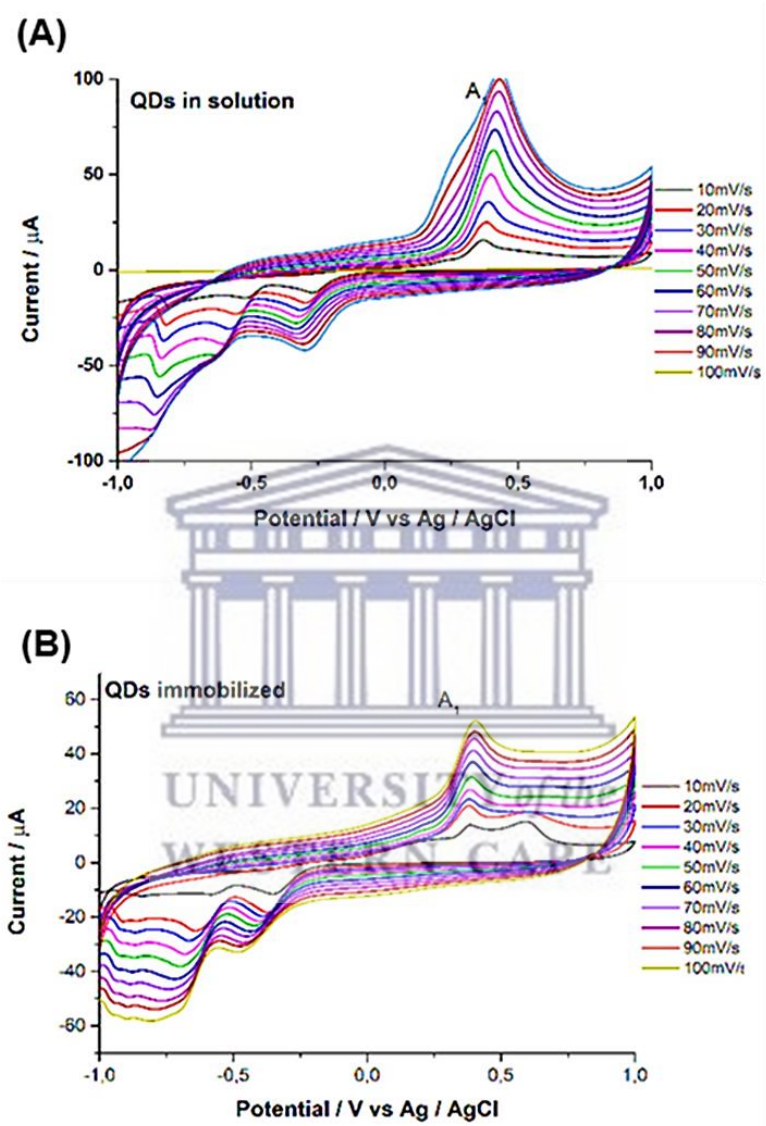

Figure 4. 19: CVs of MSA-WTe_3 QDs in solution at a SPCE (A) and immobilized on a SPCE (B) in 10 mM PBS, pH 7.4, at different scan rates in the range from 10 mV/s to 100 mV/s. It can be seen that in both CV's, a prominent peak A_1 is visible. This is attributed to the oxidation of the QDs.

Evaluating each set of cyclic voltammograms obtained for various electrode platforms, it was found that MSA-WTe_3 QDs studied at the SPCE appeared to show a more favourable electrochemical behaviour. For this reason, SPCEs will be the primary focus as working electrodes for biosensor/aptasensor fabrication and application.

The peak characteristics of QDs can be further analysed to obtain information regarding the surface concentration of the QDs on the SPCE surface. This was done by constructing a plot of ($I_{p,a}$) versus the scan rate (ν) in the range of 10 mV/s to 100 mV/s as shown in Figure 4.20 (A) below. A linear relationship between $I_{p,a}$ versus scan rate (ν) was observed since the linear correlation coefficient (R^2) was found to be 0.994.

Log $I_{p,a}$ versus Log scan rate (ν) is shown in Figure 4.20 (B), and a linear relationship (R^2 = 0.983) with a slope of 0.592 µA/mV.S^{-1} can be observed. These results indicate that the electron transfer reaction was controlled by the adsorption of the MSA-WTe_3 QDs immobilized on the surface of a SPCE in 10 mM PBS, pH 7.4.

Since the electrochemical reaction was found to be controlled by the adsorption of the surface concentration of the immobilized QDs on the surface of the SPCE, the surface concentration could be determined by the Brown Anson approximation given by Equation 4.2 below:

$$I_p = \frac{n^2F^2A\Gamma}{4RT}V \qquad [4.2]$$

Where $I_{p,c}$ = peak cathodic current, n = number of electrons (n = 1), F = 96485 c mol^{-1} (Faraday's constant), A = 0.0201 cm^2 surface area of electrode, R = 8.314 J $mol^{-1}K^{-1}$(Gas constant), T = absolute temperature (298K) of the system, and ν = scan rate in V s^{-1} and Γ is the (surface coverage). Therefore, the surface concentration of the surface adsorbed quantum dots was calculated to be

$$\Gamma = 2.250 \times 10^{-8}\, mol.cm^{-2}$$

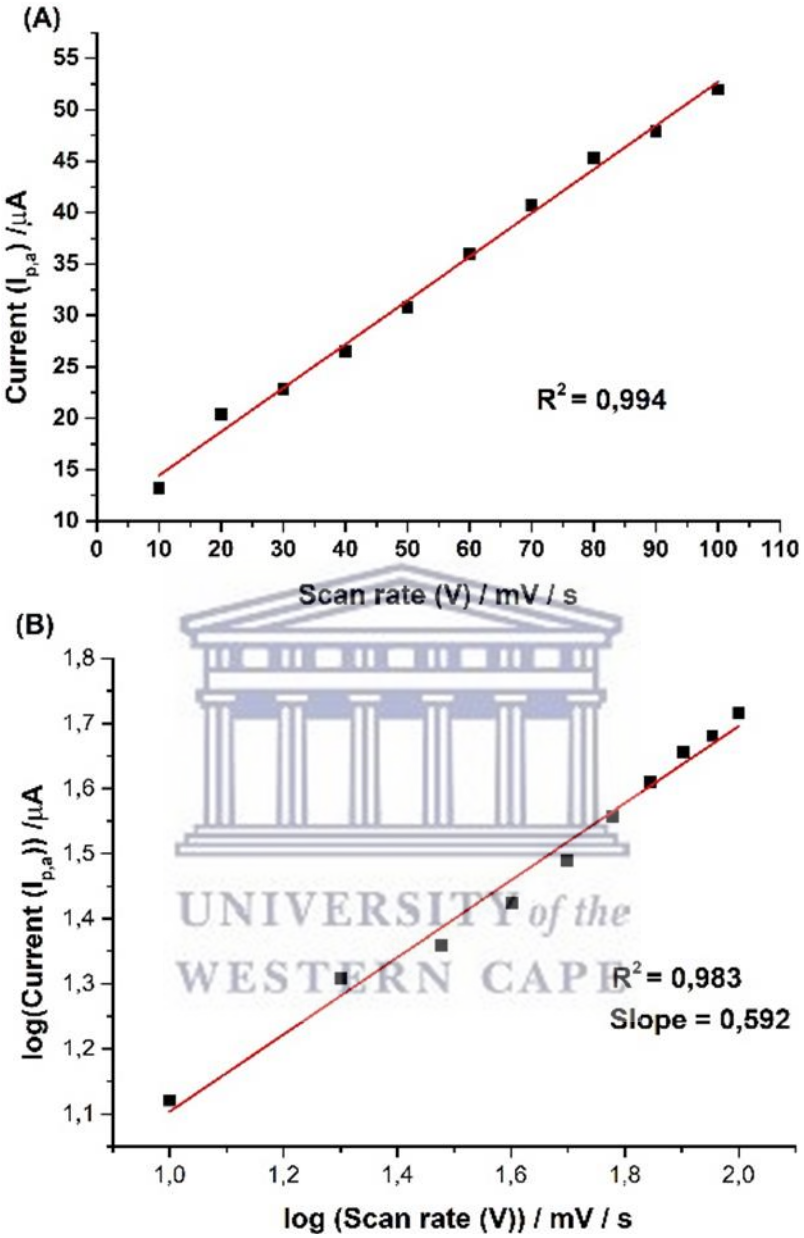

Figure 4. 20: Shows the (A) anodic plot (peak A_1) of peak current ($I_{p,a}$) versus scan rate (ν) and (B) plot of log peak current ($I_{p,a}$) versus log scan rate (ν).

4.1.8) Electrochemical Impendence Spectroscopy (EIS)

EIS was used to investigate the electrochemical properties of the MSA-WTe_3 QDs. Data obtained was then interpreted using both Nyquist and Bode plots. All parameters and conditions under which EIS experiments were performed are discussed in ***chapter three section 3.7***. Figure 4.21 shows Nyquist plots for a bare SPCE and a SPCE with MSA-WTe_3 QDs immobilized on it. The data obtained from the Nyquist plot was then interpreted using ZView® software, and its equivalent circuit obtained is shown.

The equivalent circuit was modelled to fit the QDs impedance data, shown as an inset in Figure 4.21. The equivalent circuit consists of elements such as R_S which denotes the solution resistance of the electrolyte solution, CPE which describes double layer capacitance and R_{ct} which describes charge transfer resistance properties.[1] Using this equivalent circuit it was evident that the R_{ct} value for the bare SPCE ($R_{CT} = 5.1759 \times 10^5 \Omega$ Bare SCE_GCE) was higher than the R_{ct} obtained for the MSA-WTe_3 QDs ($R_{CT} = 6.3001 \times 10^3 \Omega$ SCE_GCE/QDs).

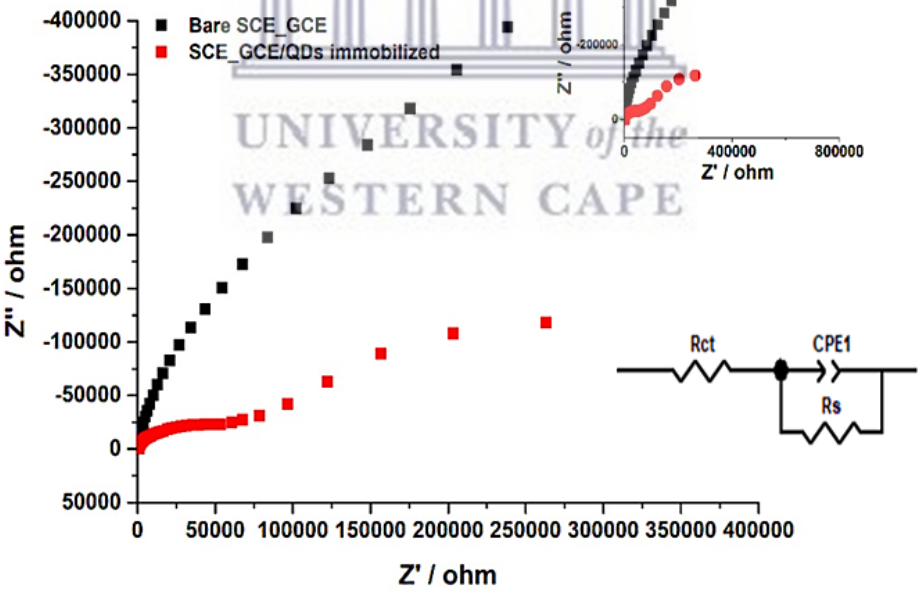

Figure 4. 21: Nyquist plots of bare SPCE and MSA-WTe_3-QDs immobilized on SPCE, respectively, in 10 mM PBS, pH 7.4. The inset shows the Randles equivalent circuit which was used to model/interpret impedance data.

This indicates that through incorporation of MSA-WTe_3 QDs the electrical conductivity was increased, and thus improved the transfer of charge to the electrode surface, and hence acting as an electron mediating platform. Similar findings were reported in the work done by Sahoo and co-workers[17], where the use of carbon quantum dots helped improve supercapacitor performance, and this was confirmed by EIS analysis, where electrons were easily transported deeper into layers of the capacitor material and showed a significant decrease in R_{ct} of the carbon QDs modified state in comparison to the unmodified material.[17] Furthermore, making reference to the Nyquist plot in Figure 4.21, it can be seen that during magnification of the impedance plot, close to the origin at very low frequencies, a small semi-circle can be observed (right inset on graph), indicating the low charge transfer resistance of the QDs material.[18] Figure 4.22 shows the Bode plots of bare SPCE and SPCE with MSA-WTe_3 QDs immobilized on it, respectively. It can be observed that the phase angle is higher for the bare SPCE (85º) than that of the SPCE/MSA-WTe_3 QDs (73º) at lower frequencies, which indicates an increase in the conductivity associated with the MSA-WTe_3-QDs/SPCE system. This increase in conductivity makes the MSA-WTe_3 QDs an ideal electron mediating platform in constructing a QD based aptasensor. It can also be stated that the Nyquist and Bode plots are in accordance with each other.

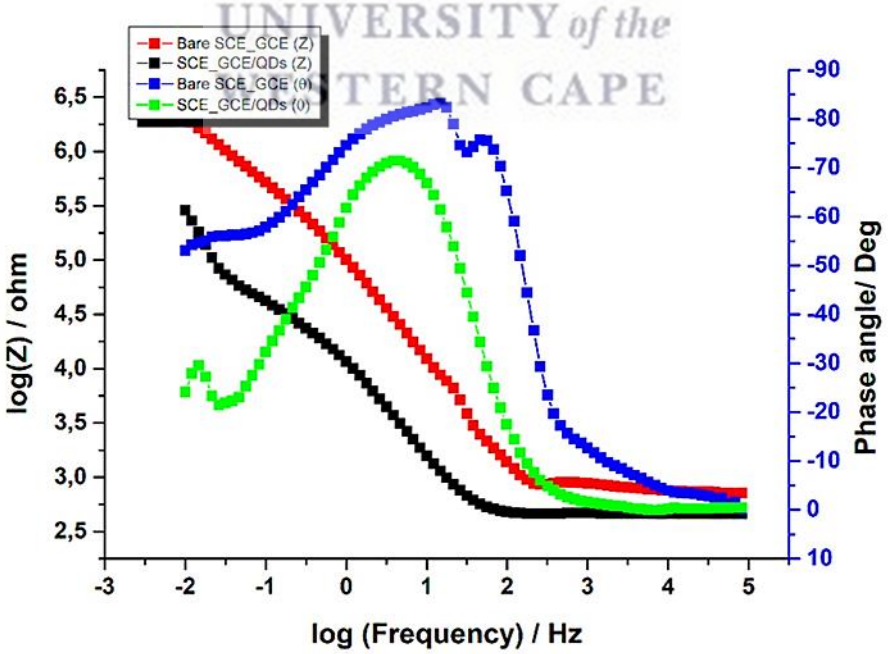

Figure 4. 22: Bode plots of bare SPCE and MSA-WTe3-QDs/SPCE in 10 mM PBS, pH 7.4.

4.2) Characterization of MSA-WTe_3 QDs based Aptasensor for AMACR detection

Characterization of MSA-WTe_3 QD aptasensor was done using techniques such as CV, EIS and DPV all experimental conditions and parameters can be found in ***chapter 3 section 3.7***.

4.2.1) Fabrication of the sensor

Cyclic voltammetry as well as electrochemical impedance was used to study the different modification steps in the aptasensor fabrication process.

4.2.1.1) Fabrication of the sensor characterized using CV

The electrochemical performance of the Aptasensor during its different modification steps was studied by CV to evaluate the electron transfer efficiency of each electrode modification. In addition, the peak characteristic of the ferricyanide $[Fe(CN)_6]^{3-}$ electrochemical probe were monitored to check the change in the electrochemical response for each modification step. The cyclic voltammogram illustrated in Figure 4.23 show the fabrication of the sensor by comparing the bare SPCE to both the SPCE/MSA-WTe_3 QDs and SPCE/MSA-WTe_3 QDs/APT, respectively. It can be seen that the ferricyanide probe shows two redox peaks at the bare SPCE. As soon as the QDs are attached to the SPCE surface, a drastic increase in the peak currents can be observed, which can be due to the synergistic effect from the electroactive MSA-WTe_3 QDs.[18] This confirms the good electronic properties of the MSA-WTe_3 QDs. Upon further investigation of the CV curves, shown in Figure 4.23, it can be seen that the presence of the aptamer causes a decrease in peak currents. This might be assigned to the steric hindrance effect between the modified aptamer and the electrolyte solution.[18] These results showed a similar response in comparison to the work done by Wang and co-workers.[18]

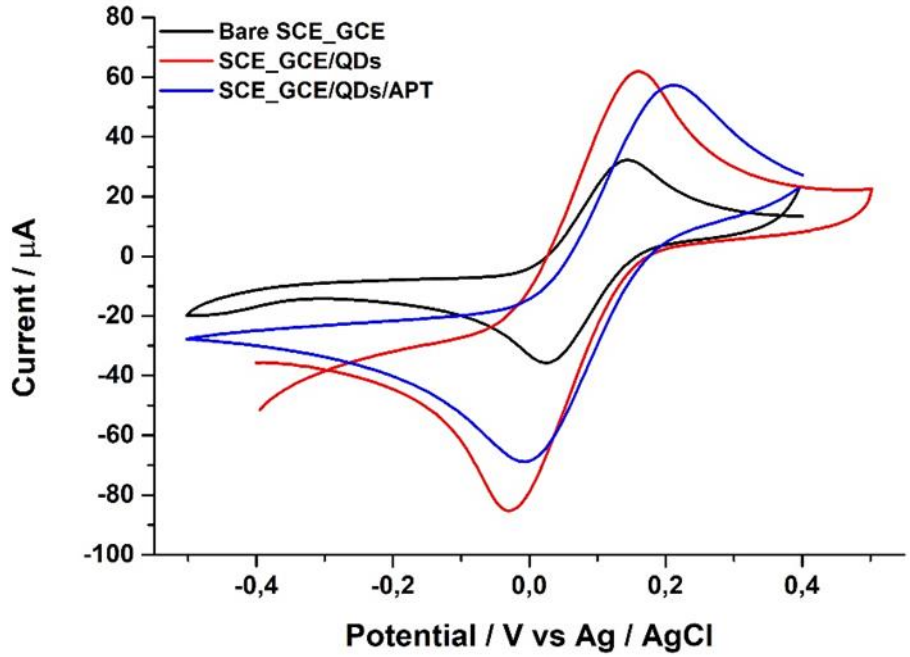

Figure 4. 23: CV curves of the different modification steps in aptasensor fabrication. Bare SPCE, SPCE/MSA-WTe_3 QDs and SPCE/MSA-WTe_3 QDs/APT are studied in 5 mM ferricyanide (prepared using 10 mM PBS, pH 7.4) at a scan rate of 50 mV/s.

4.2.1.2) Fabrication of the sensor characterized using EIS

By studying the Nyquist plots which were modelled using the equivalent circuit model (Figure 4.21), the R_{ct} values for each modification step were obtained and are tabulated in Table 4.1. It can be seen that the highest R_{ct} was that of the bare electrode, and the lowest being that of the QDs immobilized onto the surface, resulting in the conclusion that the QDs made the surface more conductive. However, upon addition of the Aptamer (synthetic single stranded DNA with amine ends for attachment) onto the SPCE/MSA-WTe_3 QD modified electrode now denoted as SPCE/MSA-WTe_3 QDs/APT, the R_{ct} resulted in a massive increase. The high R_{ct} value obtained when analysing the SPCE/MSA-WTe_3 QDs/APT implies successful assembly of the aptamer. The increase in resistance when the aptamer is added, is due to electrostatic repulsion between the negatively charged amine group on the aptamer and the PBS solution.[18] Another reason for the increase in R_{ct} when the aptamer is introduced, is due to the conformational changes the aptamer undergo, thus hindering the flow of electrons from the electrolyte to the SPCE surface (these changes can be seen in Figure 4.13–SEM data). An increase in the R_{ct} value for immobilization step of the blocking

agent is generally expected, as its role is to limit or hinder interfacial electron transfer to the electrode as explained in the work done by Wang and co-workers,[18] However, in this system this was not the case. This could possibly be due to the insufficient concentration of the MCH blocking buffer used.

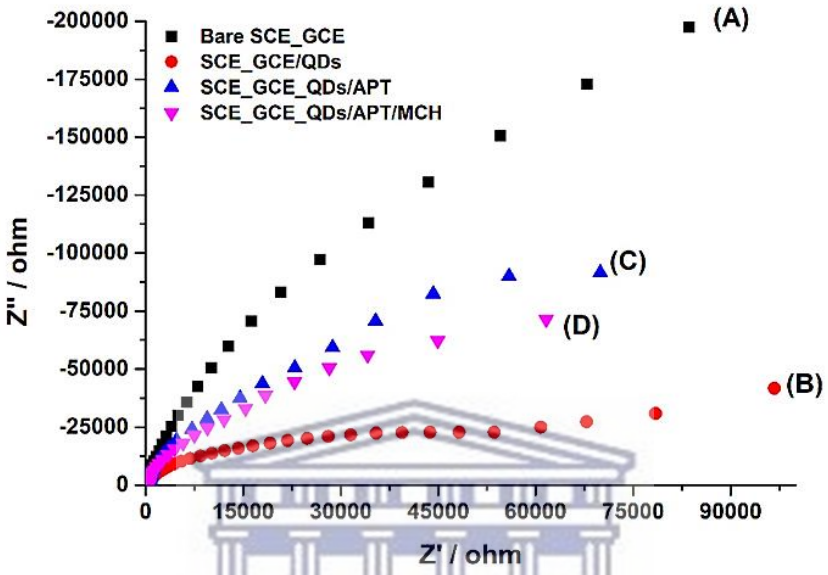

Figure 4. 24: Nyquist plot showing the different modification steps of the MSA-WTe_3 QDs based aptasensor in 10 mM PBS, pH 7.4. Where, (A) represents the Bare SPCE, (B) represents the SPCE/MSA-WTe_3 QDs, (C) represents the SPCE/MSA-WTe_3 QDs/APT, and (D) represents the SPCE/MSA-WTe_3 QDs/APT/MCH,

Table 4. 1: Charge transfer resistance (Rct) values of different medication steps obtained from fitting the EIS Nyquist plot in Figure 4.24.

Fabrication step of electrode	R_{ct}	% Error
Bare SCE_GCE	5.1759 X 10^5	10,156
SCE_GCE/QDs	6.3001 X 10^3	4.2644
SCE_GCE/QDs/APT	3.1665 X 10^4	1.5541
SCE_GCE/QDs/APT/MCH	1.9985 X10^4	4.4466

Phase angle (A) and total impedance (B) plots complementary to the Nyquist plot (Figure 4.24) are shown in Figure 4.25: It can be seen that the phase angle at low frequencies changes with each fabrication step.

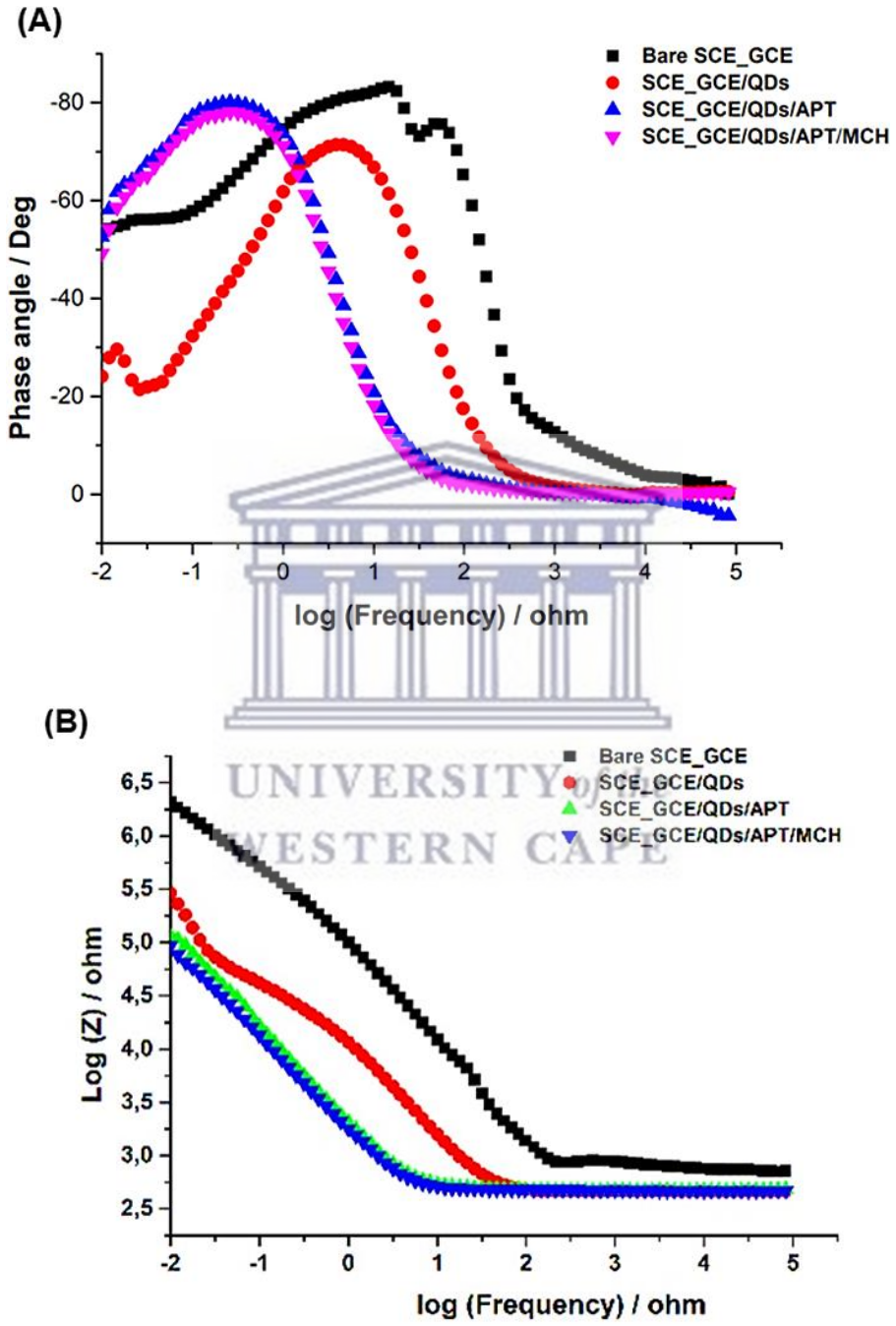

Figure 4. 25: Bode plots represented by the phase angle (A) and total impedance (B) plots for the different modification steps in the aptasensor fabrication process.

Interpreting Figure 4.25, it can be seen that the phase angle for the bare SPCE, SPCE/MSA-WTe_3 QDs/APT and SPCE/MSA-WTe_3 QDs/APT/MCH is high compared to the SPCE/MSA-WTe_3 QDs. This indicates a greater electrical conductivity associated with quantum dots. Thus, the Bode plots are in good accordance with the Nyquist plots for the sensor fabrication steps.

4.2.2) Aptasensor response to AMACR biomarker

In this study screen printed carbon electrodes (SPCEs) were modified with MSA-WTe_3 QDs synthesized using an aqueous route in order to allow it to be biocompatible for the detection of biological components such as AMACR. Using an amine modified aptamer specific to the AMACR biomarker, QDs on the surface of the SPCE were then modified. This was done in order to allow fast transfer of electrons to the electrode surface for quantification. In order to achieve the greatest selectivity towards the analyte each modification step during sensor fabrication was optimized before final fabrication of the aptasensor.

4.2.2.1) Response of MSA-WTE_3 QDs Aptasensor to AMACR biomarker (Target) using Differential Pulse Voltammetry (DPV)

In this study AMACR an emerging biomarker for prostate cancer was detected directly via MSA-WTe_3 QDs based aptasensor. QDs were used as an electron mediator in order to exploit its electronic properties. QDs were not only advantages to this study because of its excellent electron transfer properties, but also due to their small surface area which allowed for greater aptamer attachment onto the sensor platform, thereby increasing the overall sensitivity and selectivity of the aptasensor. QDs allowed aptamers specific to AMACR to bind to the surface of the SPCE via an amine carboxylic interaction which was mediated through the use of EDC/NHS interaction. The response of the MSA-WTe_3 aptasensor was investigated using DPV and the results are shown in Figure 4.26 and Figure 4.27 below.

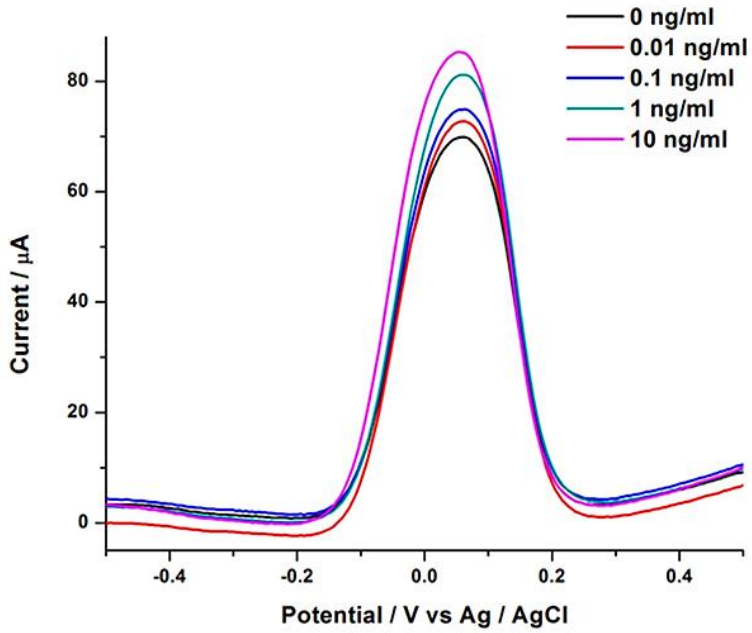

Figure 4. 26: DPV response of SPCE/MSA-WTe_3 QDs/APT/MCH sensor towards varying concentrations of AMACR, in the range 0 ng/mL – 10 ng/mL, in 5 mM ferricyanide, in 10 mM PBS, pH 7.4.

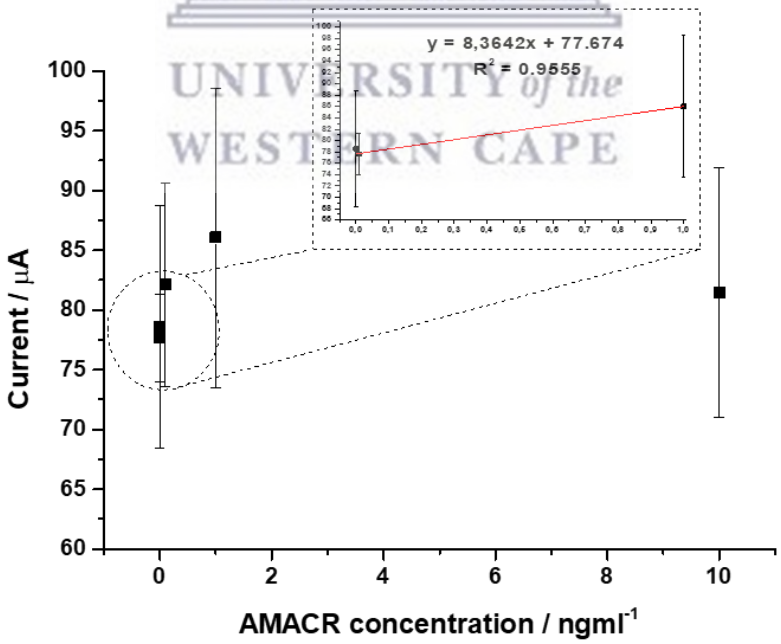

Figure 4. 27: Corresponding DPV calibrations curve responses of MSA-WTe_3 QDs based aptasensor towards different concentrations of the AMACR biomarker. Each error bar corresponds to the average of no less than three independent replicates.

DPV was used as a method of detection since it has a high sensitivity and low resolution in comparison to other electrochemical techniques such as CV. From Figure 4.26, it can be seen that the oxidation peak current increased with an increase in AMACR concentration, thus resulting in a linear relationship between the oxidation peak current and the concentration of AMACR. In order to fully understand the data obtained by DPV studies, a calibration curve was constructed and is shown in Figure 4.27. The inset on this graph just gives insight on the linear part of the calibration curve, however, more data points are required in order to move to higher and lower detection values and thus allow for a wider dynamic range. But based on the present data the calibration curve shows a good linear response with a correlation coefficient of R^2= 0.96. Three replicas (n = 3) of each DPV detection was done in order to determine the detection limit.

$$LOD = 3 \times \frac{standard\ deviation\ of\ blank}{sensitivity} \qquad [4.3]$$

Equation 4.3: Formula for calculating the limit of detection (LOD)

The detection limit (S/N = 3) was calculated to be 0.35651 ng/mL and the limit of quantification was 1.08033 ng/mL.

Table 4. 2: Recent AMACR detection methods reported in literature

Method of detection	Limit of detection	Dynamic linear range	References
Immunosensor	0.05µg/ml	0.900µg/ml	(Yao et al)[19]
Fluorescent enzyme linked aptamer immunosensor	19.5ng/ml	(10^{-1} to 10^{3}nM)	(kai et al)[20]
Colorimetric assay	1.4nmol/min/mg	(1.4-255 nmol/min/mg)	(Yevglevskis et al)[21]

Table 4.2 above shows the recent detection methods reported in literature for the detection of emerging prostate cancer biomarker AMACR. AMACR has been detected in lower detection limits than shown in the table above and this could be due to the incorporation of the novel MSA-WTe_3 QDs. Future work has to be done in order to increase the sensitivity of the sensor and optimize its performance in real samples.

References

1 S. F. Douman, The Response Dynamics of Indium Telluride Quantum Dots Impedimetric Genosensor for Telomerase Cancer Biomarker,University of the Western Cape, Thesis,2013.

2 T. M. Samir, M. M. H. Mansour, S. C. Kazmierczak and H. M. E. Azzazy, Quantum dots: Heralding a brighter future for clinical diagnostics, *Nanomedicine*, 2012, **7**, 1755–1769.

3 O. Arellano-Tánori, M. C. Acosta-Enríquez, R. Ochoa-Landín, R. Iñiguez-Palomares, T. Mendívil-Reynoso, M. Flores-Acosta and S. J. Castillo, Copper-selenide and copper-telluride composites powders sintetized by ionic exchange, *Chalcogenide Lett.*, 2014, **11**, 13–19.

4 U. Feleni, Palladium Telluride Quantum Dots Biosensor for the Determination of Indinavir Drug, University of the Western Cape, Thesis, 2013.

5 L.G. Pacoste, Development of Copper Selenide Quantum Dots-Based Therapeutic Drug Monitoring Biosensors for Toremifene , Univeristy of the Western Cape, Thesis,2017.

6 A. R. Jose, A. E. Vikraman and K. Girish Kumar, Photoinduced electron transfer between quantum dots and pralidoxime: An efficient sensing strategy, *New J. Chem.*, 2017, **41**, 10828–10834.

7 N. Allec, M. Choi, N. Yesupriya, B. Szychowski, M. R. White, M. G. Kann, E. D. Garcin, M. C. Daniel and A. Badano, Small-angle X-ray scattering method to characterize molecular interactions: Proof of concept, *Sci. Rep.*, 2015, **5**, 1–12.

8 P. Sobrova, M. Ryvolova, J. Hubalek, V. Adam and R. Kizek, Voltammetry as a tool for characterization of CdTe quantum dots, *Int. J. Mol. Sci.*, 2013, **14**, 13497–13510.

9 F. Mezrag, N. Bouarissa and M. Boucenna, Optik The size-dependent electronic and optical properties of InAs quantum dots, *Opt. - Int. J. Light Electron Opt.*, 2016, **127**, 1167–1170.

10 W. C. Law, K. T. Yong, I. Roy, H. Ding, R. Hu, W. Zhao and P. N. Prasad, Aqueous-phase synthesis of highly luminescent CdTe/ZnTe core/shell quantum dots optimized for targeted bioimaging, *Small*, 2009, **5**, 1302–1310.

11 H. Li, W. Y. Shih and W. H. Shih, Synthesis and characterization of aqueous carboxyl-capped CdS quantum dots for bioapplications, *Ind. Eng. Chem. Res.*, 2007, **46**, 2013–2019.

12 M. S. Martín-González, A. L. Prieto, R. Gronsky, T. Sands and A. M. Stacy, Insights into the electrodeposition of Bi2Te3, *J. Electrochem. Soc.*, 2002, **149**, 546–554.

13 Y. Wang, Y. Sun, H. Liao, S. Sun, S. Li, J. W. Ager and Z. J. Xu, Activation Effect of Electrochemical Cycling on Gold Nanoparticles towards the Hydrogen Evolution

Reaction in Sulfuric Acid, *Electrochim. Acta*, 2016, **209**, 440–447.

14 S. . Mundinamani and M. . Rabinal, Cyclic Voltammetric Studies on the Role of Electrode, Electrode Surface Modification and Electrolyte Solution of an Electrochemical Cell, *IOSR J. Appl. Chem.*, 2014, **7**, 45–52.

15 S. Cong, Y. Tian, Q. Li, Z. Zhao and F. Geng, Single-crystalline tungsten oxide quantum dots for fast pseudocapacitor and electrochromic applications, *Adv. Mater.*, 2014, **26**, 4260–4267.

16 M. Gougis, D. Ma and M. Mohamedi, Tungsten oxide-Au nanosized film composites for glucose oxidation and sensing in neutral medium, *Int. J. Nanomedicine*, 2015, **10**, 2939–2950.

17 S. Sahoo, A. K. Satpati, P. K. Sahoo and P. D. Naik, Incorporation of Carbon Quantum Dots for Improvement of Supercapacitor Performance of Nickel Sulfide, *ACS Omega*, 2018, **3**, 17936–17946.

18 Q. Wang, X. Qin, L. Geng and Y. Wang, Label-free electrochemical aptasensor for sensitive detection of malachite green based on au nanoparticle/graphene quantum dots/tungsten disulfide nanocomposites, *Nanomaterials*, , DOI:10.3390/nano9020229.

19 J. Yao, Y. Wang, Y. Dai and C. C. Liu, Bioconjugated, Single-Use Biosensor for the Detection of Biomarkers of Prostate Cancer, *ACS Omega*, 2018, **3**, 6411–6418.

20 D. K. Yang, L. C. Chen, M. Y. Lee, C. H. Hsu and C. S. Chen, Selection of aptamers for fluorescent detection of alpha-methylacyl-CoA racemase by single-bead SELEX, *Biosens. Bioelectron.*, 2014, **62**, 106–112.

21 M. Yevglevskis, G. L. Lee, A. Nathubhai, Y. D. Petrova, T. D. James, M. D. Threadgill, T. J. Woodman and M. D. Lloyd, A novel colorimetric assay for α-methylacyl-CoA racemase 1A (AMACR; P504S) utilizing the elimination of 2,4-dinitrophenolate, *Chem. Commun.*, 2017, **53**, 5087–5090.

CHAPTER FIVE

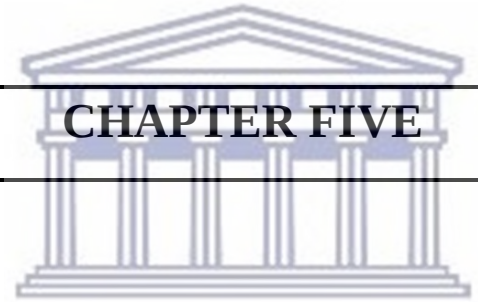

CHAPTER 5

CONCLUSION AND FURTURE WORKS

5.0) Overview

This chapter gives an overview of the study in terms of outlining the main objectives that were achieved and discusses the advantages of MSA-WTe_3 QDs as platforms in the aptasensor development for the sensitive detection of AMACR. This chapter also expresses future recommendations in order to optimize the sensor and eventually improve its design for application in the real world.

5.1 Conclusion

Prostate cancer is the leading cause of death in men in over 46 countries, currently the testing for prostate cancer results in long waiting periods and methods which are invasive and not specific to the disease itself. The main objectives of this study was to establish an ultra-sensitive aptasensor for an emerging prostate cancer biomarker known as AMACR through the implementation of novel MSA-WTe_3 QDs. This objective was achieved first via the aqueous synthesis of the MSA-WTe_3 QDs by microwave irradiation and then implementation of these QDs as an electron mediating platform for aptasensor development, in order to increase levels of sensitivity and specificity of the sensor. The MSA-WTe_3 QDs size was confirmed by HR-TEM to be 4 nm in diameter. The crystallinity of the QDs was hexagonal and this was confirmed by XRD. Elemental analysis corresponding to HR-SEM confirmed that the MSA-WTe_3 QDs are rich in both tungsten and tellurium. MSA-WTe_3 QDs showed excellent electro-catalytic properties using different sensor platforms. Impedance showed that the electrical conductivity increased in the presence of the QDs on the surface of the sensor platform, that is, screen printed carbon electrodes. The successful detection of AMACR was achieved by incubating the said biomarker onto the SPCE surface modified with QDs as an electron mediator and an amine-modified aptamer specific to the analyte (AMACR) under study. An electroanalytical technique, namely differential pulse voltammetry (DPV) was used to study the aptasensor performance towards different concentrations of AMACR. It was

observed that DPV exhibited a good linearity since its R^2 value corresponded to 0.96, and had a limit of detection as low as 0.35651 ng/mL as well as limit of quantification reported to be 1.08033 ng/mL for the detection of AMACR. Thus, the objectives of this study was achieved via the development of novel MSA-WTe_3 QDs whose properties were studied and confirmed via various characterization methods for the fabrication of a aptasensor specific to AMACR. The ultimate goal of this study is to apply this type of electrochemical biosensor to real life clinical samples, in order to implement a more improved method of prostate cancer diagnosis, which is inexpensive, simple, portable as well as non-invasive.

5.2) Recommendations for future study

Biosensors have great potential in medical diagnostics as well as disease monitoring, in terms of reducing mortality rates related to disease and allowing people to live longer more fulfilling lives. This can only be done by constantly improving and evolving on the current methods that exist for disease detection and monitoring through the implementation of new technologies and new sciences. Before the era of biosensors, methods such as High performance liquid chromatography (HPLC), Gas chromatography-Mass spectroscopy (GC-MS) as well as other long complicated laboratory procedures were primarily used for disease diagnostics.[1] However, some drawbacks associated with these conventional methods caused them to become unpopular and secondary detection systems. Some examples of these drawbacks are listed below:[1]

- Long waiting periods associated with these methods often stress patients before results are even ready.
- Large amount of sample is often needed.
- Most times samples are taken invasively from patients (often blood samples).
- Requires trained individuals to operate these systems, as it is often complicated and laborious.
- Easily allows for sample cross contamination and mix-up (increased human error).
- Requires a lot of power (electricity) to operate which increases running cost.
- Often produces a lot of waste products, and thus provision has to be made in order to dispose of the waste correctly. Costs associated with these procedures also increases.

Machinery used are often large and are termed either as ‘stand-alone’ or as ‘bench top’ machinery, thus developing countries where hospital infrastructure are lacking are hit hardest when it comes to diagnosis and treating of diseases. All of these factors have led to the ‘need’ for better methods of disease diagnosis and prognosis, and have led to the conclusion that an ideal biosensor should be fast, cost-effective, detect non-invasively, use small amount of sample and be able to detect target molecules with utmost precision and accuracy. Thus, more research has to be done in terms of improving the performance and operational principles of biosensors. Future prospects include exploring avenues such as micro/nano fluidic devices as well as wearable biosensors. These interesting and exciting approaches are further discussed in detail below.

5.2.1) Biosensors integrated with microfluidic systems

Microfluidics is considered to be a multidisciplinary technology in which fluids are controlled and manipulated usually on a scale of micro-pico litres through the use of channels and valves, which require very little sample for analysis.[2] Three main types of microfluidic devices exist, continuous flow, droplet based as well as digital microfluidics. Figure 5.1 below shows an image of each microfluidic type:

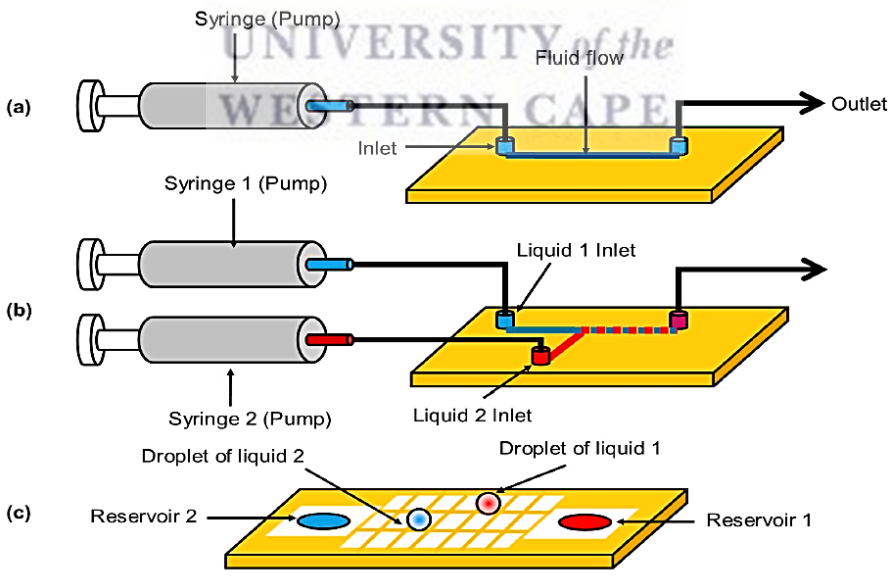

Figure 5. 1: Different types of microfluidic systems continuous (a), drop based (b) and digital image (c). Reprinted from G. Luka and co-workers, Microfluidics Intergrated Biosensors: A

Leading Technology towards Lab-on-a-Chip and sensors, *Sensors (Switzerland)* 2015, 30011 – 30031.

Continuous flow microfluidics is based on the continuous motion of fluid in a microchannel, droplet-based microfluidics are operated via the motion of droplets in a steam of immiscible fluids, and finally, digital microfluidics are based on the motion of discrete droplets on an array of electrodes.[3] Traditional biosensors can be miniaturized to perform as LOC (lab on a chip) devices, and thus, can be termed microfluidic integrated biosensors. LOC is a device a few millimetres in size which integrates many laboratory functions onto a single platform,[4] using less sample and eliminating cost associated with larger desktop machinery and different sample pre-treatment steps prior to analysis. By incorporating nanomaterials into these types of devices such as quantum dots, sensitivity and specificity can be increased, leading to better methods of disease diagnostics.

5.2.2) Wearable biosensors

Wearable biosensors refers to a class of biosensors which can be comfortably worn on the body, and provide continuous real time information via a non-invasive method of measuring biomarkers in bio-fluid such as sweat, tears and saliva.[5] This method of detection pose very little risks in terms of infection and is easy to operate. Wearable platforms can incorporate nanomaterials such as quantum dots, nanofibers, nanorods to allow a wearable sensor that gives accurate results about a certain biological process. An example of wearable sensors is the epidermal wearable biosensors, also known as, skin-worn sensors that are flexible and detects biological changes, which occur in our sweat.[6] Ocular wearable biosensors refer to biosensors that can be integrated into contact lenses, here the contact lenses come into contact with tears which could also contain biomarkers which can be quantified and detected.[5] Oral-cavity wearable biosensors detect biosensors that exist in the saliva, as many biomarkers in the saliva are passed from the blood stream via transcellular paths.[5] Figure 5.2 below shows images of different types of wearable glucose biosensors.

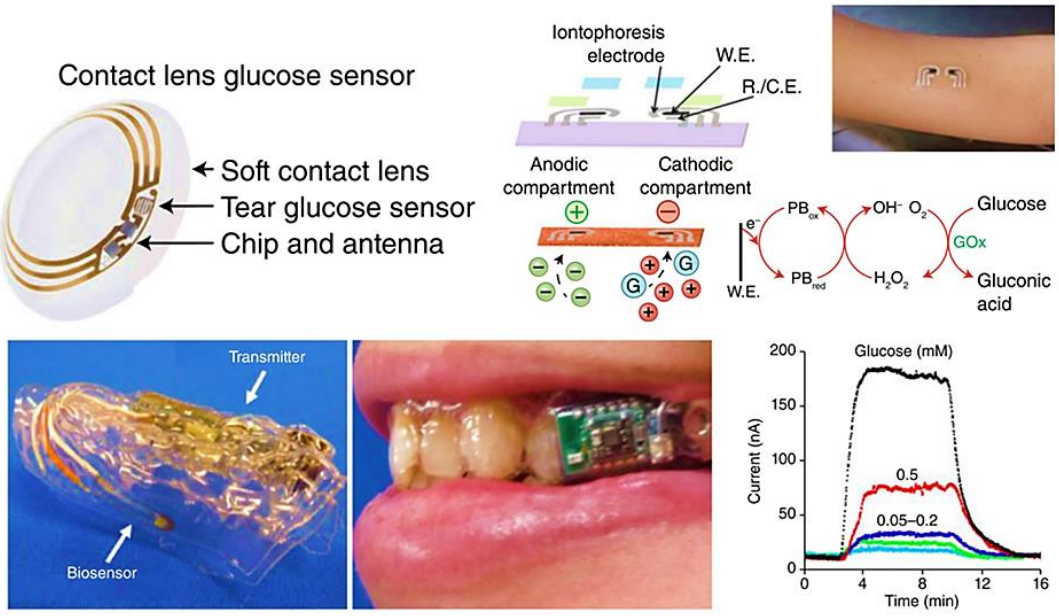

Figure 5. 2: Different types of wearable biosensors top left: ocular glucose sensor; top right: epidermal wearable biosensor, bottom: oral-cavity wearable biosensor. Image reprinted from J. kim and co-workers, Wearable biosensors for healthcare, *Nature Biotechnology*, 2019, 37, 389 – 406.

The ultimate goal for the future is to develop such devices as outlined above for early prostate cancer detection. By modifying the existing aptasensor into miniaturized devices and incorporation of nanomaterials for optimal sensor performance. These proposed methods of detection can possibly be commercialized, since it offers great advantages to the medical industry as point-of-care devices. The development and implementation of these detection methods in recent years can now easily allow medical practitioners to bridge the gap between the laboratory and the patient by bringing the laboratory to the patient (LOC/ microfluidic biosensors), thus allowing real time analysis and early detection of diseases which can then be treated adequately.

Main points to further optimize the fabricated QDs based aptasensor are highlighted below:

- QDs immobilization platform (this includes the sensor substrate) should be optimized in order to allow the most sensitive levels of AMACR detection.
- The fabricated aptasensor should not be limited to one type of cancer disease, but in future, be applicable to other types of cancer diseases such as, lung, stomach and oral cancer.

- The fabricated aptasensor should be applied to real clinical samples and compared to conventional desktop heavy machinery, which are currently used for disease diagnosis.
- Novel synthesis methods should be discovered and studied in order to produce nanomaterials of highest performance, meaning properties of these materials can be modified for different uses whether it is in medical, environmental or food.
- Different forms of detection strategies should be designed and investigated like microfluidic systems.

References

1 S. M.L., M. K.E., W. P.K. and L. J.C., Advances and challenges in biosensor-based diagnosis of infectious diseases, *Expert Rev. Mol. Diagn.*, 2014, **14**, 225–244.

2 E. J. Fong, C. Huang, J. Hamilton, W. J. Benett, M. Bora, A. Burklund, T. R. Metz and M. Shusteff, A microfluidic platform for precision small-volume sample processing and its use to size separate biological particles with an acoustic microdevice, *J. Vis. Exp.*, 2015, **2015**, 1–11.

3 G. Luka, A. Ahmadi, H. Najjaran, E. Alocilja, M. Derosa, K. Wolthers, A. Malki, H. Aziz, A. Althani and M. Hoorfar, Microfluidics integrated biosensors: A leading technology towards lab-on-A-chip and sensing applications, *Sensors (Switzerland)*, 2015, **15**, 30011–30031.

4 F. Gorjikhah, S. Davaran, R. Salehi, M. Bakhtiari, A. Hasanzadeh, Y. Panahi, M. Emamverdy and A. Akbarzadeh, Improving "lab-on-a-chip" techniques using biomedical nanotechnology: a review, *Artif. Cells, Nanomedicine Biotechnol.*, 2016, **44**, 1609–1614.

5 J. Kim, A. S. Campbell, B. E. F. de Ávila and J. Wang, Wearable biosensors for healthcare monitoring, *Nat. Biotechnol.*, 2019, **37**, 389–406.

6 J. R. Windmiller and J. Wang, Wearable Electrochemical Sensors and Biosensors: A Review, *Electroanalysis*, 2013, **25**, 29–46.